


12-1-2012

Development of Nano-ZrO₂ Reinforced Self-Flowing Low and Ultra Low Cement Refractory Castables

Cem Gogtas

University of Wisconsin-Milwaukee

Follow this and additional works at: <https://dc.uwm.edu/etd>

 Part of the [Materials Science and Engineering Commons](#), and the [Nanoscience and Nanotechnology Commons](#)

Recommended Citation

Gogtas, Cem, "Development of Nano-ZrO₂ Reinforced Self-Flowing Low and Ultra Low Cement Refractory Castables" (2012).
Theses and Dissertations. 51.
<https://dc.uwm.edu/etd/51>

This Dissertation is brought to you for free and open access by UWM Digital Commons. It has been accepted for inclusion in Theses and Dissertations by an authorized administrator of UWM Digital Commons. For more information, please contact open-access@uwm.edu.

DEVELOPMENT OF NANO-ZrO₂ REINFORCED SELF-FLOWING LOW AND
ULTRA LOW CEMENT REFRACTORY CASTABLES

by

Cem Gogtas

A Dissertation Submitted in
Partial Fulfillment of the
Requirements for the Degree of

Doctor of Philosophy
in Engineering

at

The University of Wisconsin-Milwaukee

December 2012

ABSTRACT
DEVELOPMENT OF NANO-ZrO₂ REINFORCED SELF-FLOWING LOW AND
ULTRA LOW CEMENT REFRACTORY CASTABLES

by

Cem Gogtas

The University of Wisconsin-Milwaukee, 2012
Under the Supervision of Professor Hugo Lopez

The main goal of this research is to develop high strength high toughness nano-ZrO₂ reinforced self flow low cement (5%) and ultra low cement (3 and 1%) castables based on tabular alumina. In processing these castables, the Andreassen model was used to obtain optimum self flow properties in both, low and ultra low castables. The castables thus produced were fired at 110 and 1000, 1300 and 1500°C and the phases obtained were investigated by X-ray diffraction (XRD) including energy dispersive X-ray (EDX), scanning electron microscopy (SEM), thermogravimetric analysis (TGA) and differential thermal analysis (DTA). In addition, the other castable properties were measured such as cold crushing strength (CCS), apparent porosity (AP), bulk density (BD), water absorption (WA), weight loss (WL), zeta potential (ZP), flexural strength (MOR), fracture toughness (K_{IC}), indentation toughness and self-leveling flowability. It was found that 5% cement castables exhibit the highest densification and strength after firing at 1500°C for 3 hours. In addition, castables with various amounts of nano-ZrO₂ and YSZ (yttria stabilized zirconia) (5%, 3%, 1%, 0.1% and 0.01%) were fired at 1300°C in order to improve the flexural strength and fracture toughness. The results indicate that the addition of nano-ZrO₂ improves the flexural strength by 20% but it does not have an

important effect on the K_{IC} . Apparently, the presence of a relatively high density of pores and cracks overrides the potential benefits associated with the nano-ZrO₂ and YSZ reinforcement additions.

©Copyright by Cem Gogtas, 2012
All Rights Reserved

TABLE OF CONTENTS

ABSTRACT

TABLE OF CONTENTS

LIST OF FIGURES

LIST OF TABLES

LIST OF SYMBOLS and ABBREVIATIONS

ACKNOWLEDGEMENTS

CHAPTER 1. INTRODUCTION	1
CHAPTER 2. LITERATURE REVIEW	4
2.1 Refractory Castable Compositions	4
2.2 Phase Composition	9
2.2.1 Bonding Mechanism	13
2.2.2 Dehydration and Firing	16
2.3 Surface Chemistry	17
2.3.1 Dispersion Mechanism	18
2.3.2 Electric Double Layer	20
2.3.3 Zeta Potential	21
2.3.4 Dispersants	27
2.4 Types of Refractory Castables	29
2.4.1 Conventional Castables	30
2.4.1.1 Disadvantages	30
2.4.2 Low and Ultra Low Cement Castables	33
2.4.2.1 Particle Packing, Dispersion and Rheology	35

2.4.2.2 Properties	41
2.4.3 Zero Cement or Cement Free Castables	45
2.4.4 Free or Self Flowable Castables	48
2.5 Fracture of Refractories	53
2.5.1 Strength of Refractories	57
2.5.1.1 Indentation Fracture Toughness	64
2.5.2 Crack Process Zone for Refractories	70
2.5.3. Toughening Mechanism	73
2.5.3.1 Transformation Toughening	74
2.5.3.1.1 Thermodynamics of Transformation	77
2.5.3.1.2 Stabilization of Tetragonal Zirconia	79
2.5.3.1.3 Ytria Content and Distribution	80
2.5.4 Fractography	84
Chapter 3. SCOPE and OBJECTIVES	89
3.1 Experimental Research	89
3.2 Experimental Refractory Compositions	89
3.2.1 Refractory Aggregate	90
3.2.2 Refractory Fillers and Modifiers	90
3.2.3 Bonding Agents	90
3.2.4 Additives	90
3.3 Preparation of Nanoparticles	91
3.4 Self-Flowing Test	92
3.5 Determination of Particle Size Distribution, Zeta Potential and pH of Nanoparticles	93

3.6 Bulk Density, Apparent Porosity, Water Absorption and Density	94
3.7 Microstructural Analysis	95
3.8 Cold Crushing Strength (CCS), Modulus of Rupture (MOR), Fracture Toughness (K_{IC}) and Indentation Toughness of Castables	96
3.9 Rheology and Flow Measurements of Castable Refractories	100
Chapter 4. EXPERIMENTAL RESULTS and DISCUSSION	101
4.1 Determination of Andreassen Distribution Coefficient of SFCs	101
4.2 X-Ray Diffraction (XRD) Analysis of SFCs	102
4.3 Self-Flow Measurement of Castables	106
4.4 Correlation of Zeta Potential, pH and Particle Size Distribution of Nano-ZrO ₂ Powder	108
4.5 Bulk Density, Apparent Porosity and Water Absorption of SFCs	110
4.6 Thermogravimetric Analysis (TGA) and Differential Thermal Analysis (DTA) of Castables	114
4.7 Cold Crushing Strength (CCS) of Castables	116
4.8 Modulus of Rupture (MOR) of Castables	118
4.9 Fracture Toughness (K_{IC}) of Castables	120
4.10 Indentation Toughness of Castables	122
4.11 Effect of nano-ZrO ₂ and YSZ Addition on the Modulus of Rupture (MOR) of SFCs	125
4.12 Modulus of Rupture of Binding System	136
4.13 Fracture Toughness of Binding Systems of Castables	137
4.14 Effect of Nano-ZrO ₂ addition on the MOR of Binding System of Castables	139
4. 15 Effect of Yttria Distribution of Nano-ZrO ₂ Reinforced Refractory Castables	141

4.16 Effect of Drying on Modulus of Rupture of Binding System	143
4.17 Microstructural Investigation of Fracture Surfaces	145
Chapter 5 CONCLUSION	155
Chapter 6. FUTURE WORK	160
REFERENCES	161
CURRICULUM VITAE	171

LIST OF FIGURES

Figure 2.1 Typical powder processed refractory microstructure.	4
Figure 2.2 Wet-gunning of the ultra low cement bauxite based castable.	9
Figure 2.3 SEM micrographs of fracture surfaces of samples prepared using $\text{CaO-Al}_2\text{O}_3$: (a) sintered at 1300°C and (b) sintered at 1550°C for 2 h, showing the evolution and morphology of CA_2 and CA_6 , respectively.	12
Figure 2.4 (a) Uncharged Particles are free to collide and aggregate (b) charged particles repel each other.	19
Figure 2.5 Schematic representation of the Double Layer	20
Figure 2.6 Schematic representation of zeta potential.	22
Figure 2.7 Zeta potential as a function of pH.	22
Figure 2.8 Zeta potential as a function of pH for some of the raw material commonly used in refractory castables.	24
Figure 2.9 pH is as a function of the deflocculants content for the different types of deflocculants.	24
Figure 2.10. Zeta potential of aqueous 3Y-TZP suspensions at different pH values	25
Figure 2.11 SEM micrographs of green compacts dried from the slurries with 47–50 wt.% solid content and pH values at (a) pH 3; (b) pH 4.5; (c) pH 5.5; (d) pH 7.5.	26
Figure 2.12 Effect of time on the zeta potential of a suspension prepared from the Tosoh zirconia powder.	27
Figure 2.13. Examples of the effect of (a) anionic (0.06 wt% citric acid) and (b) cationic (0.33wt% polyethyleneimine, PEI) dispersants on the zeta potential curve of alumina and silica particles, respectively	28
Figure 2.14 Relations between particle packing, dispersion and rheology	34
Figure 2.15. Free flow as a function of time and particle size distribution at 20°C	38
Figure 2.16. Comparison of self-flowability of castables	40
Figure 2.17. Free-flow value of castables as a function of the dispersant content for compositions dispersed with citric acid, gallic acid and PBTCA (14 vol.% water)	41
Figure 2.18 Compressive strength in castables heat-treated at different temperature	42

Figure 2.19 CCS of different castable samples fired at different firing temperatures	43
Figure 2.20 Cold crushing strength of alumina castables	44
Figure 2.21 Cold crushing strength of ultra low cement castables vs. heating temperature.	44
Figure 2.22. Free flow and increase in water content vs. % dosage of Alphabond.	46
Figure 2.23 Drying behavior of green castables bonded with CAC and HAB subjected to continuous heating: (a) Rate of 10°C/min from room temperature up to 800°C. Curves (iii) and (iv) refer to moisture free (MF) samples. (b) A more aggressive heating rate (20°C/min) was applied to evaluate the explosive spalling occurrence.	47
Figure 2.24 The effect of various deflocculants on the self flow of castables.	49
Figure 2.25 Flow value and water addition for a 1.5 % cement, tabular alumina based refractory castable as a function of microsilica content.	50
Figure 2.26 Impact of warehouse aging on flow at 30 minutes	51
Figure 2.27 Free flow at 35°C as a function of time and citric acid addition. Ultra low cement castable composition with 13 vol% water (4.10 wt%).	52
Figure 2.28 Apparent viscosity as a function of time of matrix representative suspensions containing 5wt.% of sodium citrate or sodium polymethacrylate	53
Figure 2.29 Fracture toughness as a function of spinel content before and after thermal shock.	54
Figure 2.30 Fracture energy results for the samples of refractory castables heat treated at the temperatures.	56
Figure 2.31. Photograph of the fractured sample showing: matrix (fine fraction), fractured and debonded aggregates (coarse fraction), and hole produced by pull out of the aggregate.	56
Figure 2.32 Flexural strength values of 8D, 8DM and PKDOL refractory castables.	58
Figure 2.33 Plot of flexural strength (at 25°C) of fired (1500°C) in situ spinel bonded castable (G) with increasing concentration of spinel additive.	60
Figure 2.34. MOR– <i>T</i> curves for specimens A8 and S8	61
Figure 2.35 Schematic illustration of indenters tips.	65
Figure 2.36. Schematic illustration of radial cracking at a Vickers indentation.	65

Figure 2.37 Typical load-displacement data.	66
Figure 2.38 Typical cracks produced using a cube-corner indenter under a load of 2.6 N. A radial crack is highlighted. Crack tips are labelled c.	68
Figure 2.39 A small indentation in glass made with the cube-corner indenter showing well defined radial cracks.	69
Figure 2.40 (a–d) Representative SEM micrographs of nanoindentations made with various loading forces. Cracks at the corners of the indented impression can be observed.	69
Figure 2.41 Schematic of the crack process zone for refractory materials.	70
Figure 2.42 Toughening by crack deflection is estimated to increase as the obstacle shapes change from spheres, discs and rods (G_C is crack resistance force of composite, G_M is crack resistance force of matrix)	72
Figure 2.43 Crystal structures of most important zirconia polymorphs: cubic, tetragonal and monoclinic	74
Figure 2.44 The transformation ZrO_2 from tetragonal to monoclinic.	76
Figure 2.45 Stress induced phase transformation	76
Figure 2.46 Critical particle size for the retention of tetragonal zirconia	78
Figure 2.47 ZrO_2 rich portion of ZrO_2 - Y_2O_3 phase diagram in the system	81
Figure 2.48 Influence of test temperature of fracture toughness. The transformation zone size increases with decreasing temperature, as the tetragonal particles become less stable. At some critical temperature, however, the transformation can become spontaneous.	81
Figure 2.49 Crack initially propagates on a plane but, if failure is unstable, the crack will start branching	85
Figure 2.50 Fracture surfaces in brittle materials generally show a smooth region that surrounds the failure origin (mirror region) but the surface increases in roughness as the crack accelerates (mist region) until crack branching occurs. The branched region contain ‘ridges’ known as a hackle Fracture surfaces are often described as to whether a crack passes through grains (transgranular) or between grains (intergranular).	86
Figure 2.51 a) Lenticular void that acted as a fracture origin in an alumina-zirconia composite b) Spherical void that acted as a fracture origin in a an open-cell vitreous carbon; scanning electron micrograph	86

Figure 2.52 Scanning electron microscopes showing processing defects that act as fracture origins in alumina-zirconia composites: a) porous alumina agglomerate; b) large alumina grain	87
Figure 2.53 Failure origin in a zirconia-toughened alumina, caused by the presence of a zirconia aggregate in starting powder.	87
Figure 2.54 Scanning electron micrographs showing failure origins in single crystal alumina (sapphire) fibers : a) internal pore: b) surface flaw	88
Figure 2.55 Silicon carbide inclusions that acted as fracture origin in silicon nitride scanning electron micrograph.	88
Figure 3.56 The truncated flow cone described by ASTM C230	92
Figure 3.57 The measurement of self flow value of castable after pouring from truncated cone	93
Figure 3.58 Three point bending test.	97
Figure 3.59 Schematic illustration of fracture toughness test.	98
Figure 3.60 (a-b) Cracks created by Berkovich indenter in nanoindentation test	99
Figure 4.61 Andreassen distribution coefficient (q value) of castables	101
Figure 4.62 XRD patterns for (a) SFC-5, (b) SFC-3 and (c) SFC-1 dried at 110°C for 24h.	103
Figure 4.63 XRD pattern for (a) SFC-5, (b) SFC-3, (c) SFC-1 fired at 1000°C for 3h	104
Figure 4.64 XRD pattern for (a) SFC-5, (b) SFC-3, (c) SFC-1 fired at 1300°C for 3h.	105
Figure 4.65 XRD pattern for (a) SFC-5, (b) SFC-3, (c) SFC-1 fired at 1500°C for 3h.	106
Figure 4.66 Self flow values of SFCs as a function of cement content	107
Figure 4.67 Self flow values of castables as a function of nano ZrO ₂ /YSZ addition.	107
Figure 4.68 (a) PSD of nano-ZrO ₂ particles in the water solution. (b) PSD of ultrasonicated nano-ZrO ₂ particles in the water solution. (c) PSD of nano-ZrO ₂ particles dispersed with additive (D-811D) in water. (d) The effect of ultrasonication on the PSD of nano-ZrO ₂ particles with D-811D in water. (e) PSD of nano-ZrO ₂ particles dispersed with additive (M-ADS) in water. (f) The effect of ultrasonication on the PSD of nano-ZrO ₂ particles with M-ADS in water.	109

Figure 4.69 AP and BD of SFCs at different firing temperatures.	111
Figure 4.70 Water absorption of SFCs as a function of firing temperature.	113
Figure 4.71 Weight losses of SFCs as a function of firing temperatures.	114
Figure 4.72 TGA and DTA of SFCs at elevated temperatures	115
Figure 4.73 The CCS values of SFCs as a function of temperature.	117
Figure 4.74 The MOR of SFCs as a function of temperature.	119
Figure 4.75 Fracture toughness values of SFCs as a function of temperature.	121
Figure 4.76 Indentation toughness of SFCs as a function of firing temperatures	122
Figure 4.77 Optical microscope picture of SFC after nanoindentation test at 400X	123
Figure 4.78 (a) Linear crack (b) Non-linear crack created by Berkovich indenter at 400X	124
Figure 4.79 XRD patterns of (a) nano-ZrO ₂ and (b) 8% mol YSZ powders	125
Figure 4.80 XRD data of (a) 5%, (b) 3%, (c) 1%, (d) 0.1%, (e) 0.01% - 8 mol % YSZ reinforced SFC-5 at 1300°C	126
Figure 4.81 XRD data of (a) 5%, (b) 3%, (c) 1%, (d) 0.1%, (e) 0.01% - nano ZrO ₂ reinforced SFC-5 at 1300°C.	127
Figure 4.82 MOR of nano-ZrO ₂ and YSZ reinforced SFC-5 at 1300°C.	128
Figure 4.83 K _{IC} of nano-ZrO ₂ and YSZ reinforced SFC-5 at 1300°C.	128
Figure 4.84 XRD data of (a) 5%, (b) 3%, (c) 1%, (d) 0.1%, (e) 0.01% nano-ZrO ₂ - reinforced SFC-3 fired at 1300°C	129
Figure 4.85 XRD data of (a) 5%, (b) 3%, (c) 1%, (d) 0.1%, (e) 0.01% - 8 % mol YSZ reinforced SFC-3 fired at 1300°C.	130
Figure 4.86 MOR of 8 mol%-YSZ and ZrO ₂ reinforced SFC-3 at 1300°C for 3h.	131
Figure 4.87 K _{IC} of nano-ZrO ₂ and 8 mol % YSZ reinforced SFC-3 at 1300°	132
Figure 4.88 XRD data of (a) 5%, (b) 3%, (c) 1%, (d) 0.1%, (e) 0.01% nano-ZrO ₂ - reinforced SFC-1 fired at 1300°C for 3h.	132

Figure 4.89 XRD data of (a) 5%, (b) 3%, (c) 1%, (d) 0.1%, (e) 0.01% - 8 % mol YSZ reinforced SFC-1 fired at 1300°C	133
Figure 4.90 The MOR of 8 mol % YSZ and ZrO ₂ reinforced SFC-1 at 1300°C.	134
Figure 4.91 K _{IC} of nano- ZrO ₂ and 8 mol % YSZ reinforced SFC-1 at 1300°C.	135
Figure 4.92 The MOR of binding systems of SFCs as a function of temperature	136
Figure 4.93 K _{IC} of binding systems of SFCs as a function of firing temperature	138
Figure 4.94 MOR of binding system of SFC-5 as a function of firing temperatures	139
Figure 4.95 MOR of binding system of SFC-3 as a function of firing temperatures.	140
Figure 4.96 MOR of binding system of SFC-1 as a function of elevated temperature.	141
Figure 4.97 MOR of binding system of SFC-3 at elevated temperatures as a function of yttria distribution	142
Figure 4.98 Fracture toughness of binding systems of SFC-3 as a function of firing temperature.	143
Figure 4.99 Drying effect of the MOR of binding system of (a) SFC-5, (b) SFC-3 and (c) SFC-1 as a function of time	144
Figure 4.100 (a) and (b) Fracture surface of SFC-5 and SFC-3 at 110°C for 24 hours respectively and (c) EDS pattern of fracture surface of SFC-5 sample at 100X.	146
Figure 4.101 (a) Fracture surface of SFC-5 dried at 110°C for 24h (b) and (c) SEM pictures of SFC-5 at 100X	147
Figure 4.102 Fracture surfaces of (a) SFC-5 and (b) SFC-3 after drying at 110°C for 24 h at 100X	148
Figure 4.103 Fracture surface of SFC-5 (a) at 100X and (b) at 500X after firing at 1000°C for 3h.	148
Figure 4.104 (a) and (b) EDS patterns of SFC-5 sample after firing at 1000°C for 3h.	149
Figure 4.105 Fracture surfaces of (a) SFC-3 and (b) SFC-1 after firing at 1000°C for 3h at 100X	150

Figure 4.106 Fracture surfaces of (a) SFC-5 and (b) SFC-1 after firing at 1300°C for 3h at 150 500X.

Figure 4.107 (a) Fracture surface of SFC-5 and (b) SEM picture of SFC-5 at 50X 151 (c) fracture surface and (d) SEM picture of SFC-1 at 50X after firing at 1500°C for 3h

Figure 4.108 Fracture surfaces of (a) SFC-1 and (b) SFC-5 after firing at 1300°C for 3h at 152 1000X.

Figure 4.109 Fracture surfaces of (a) SFC-1 and (b) SFC-3 after firing at 1500°C for 3h at 152 1000X

Figure 4.110 Fracture surfaces of (a) SFC-5 and (b) SFC-3 after firing at 1300°C for 3h at 153 1000X

Figure 4.111 Fracture surface of SFC-3 (a) at 2000X and (b) at 5000X after firing at 153 1300°C for 3h.

.

LIST OF TABLES

Table 2.1 Refractory Castable Composition.	5
Table 2.2 Primary Alumina and Alumina-Silicate Aggregates.	5
Table 2.3 Common Refractory Fillers and Modifiers.	6
Table 2.4 Calcium Aluminate Cement Types.	7
Table 2.5 General types of additives and their functions in the castable system.	8
Table 2.6 Typical mineral constituents of calcium aluminate cements.	10
Table 2.7 Properties of CAC mineral constituents.	11
Table 2.8 Properties of CA cement hydrates.	15
Table 2.9. Dehydration temperature of CA cement hydrates.	16
Table 2.10 Mineralogical changes of dehydrated high alumina cement on heating	17
Table 2.11. Details of Castable mixes.	39
Table 2.12 Some typical fracture toughness values for brittle materials.	73
Table 2.13 Measured properties of $\text{MgCr}_2\text{O}_4\text{-ZrO}_2$ composite specimens with different volume fractions of ZrO_2 inclusions.	84
Table 3.14 Experimental castable compositions.	91

LIST OF SYMBOLS AND ABBREVIATIONS

LCC	Low Cement Castable
ULCC	Ultra Low Cement Castable
CAC	Calcium Aluminate Cement
HAC	High Alumina Cement
SFCs	Self Flow Castables
PSD	Particle Size Distribution
ASTM	American Society for Testing and Materials
XRD	X Ray Diffraction
EDX	Energy Dispersive X-Ray
SEM	Scanning Electron Microscope
TGA	Thermo Gravimetric Analyzer
DTA	Differential Thermal Analysis
CCS	Cold Crushing Strength
AP	Apparent Porosity
BD	Bulk Density
WA	Water Absorption
WL	Weight Losses
ZP	Zeta Potential
MOR	Modulus of Rupture
K_{IC}	Fracture Toughness
HAB	Hydratable Alumina Bonded
A-1000SG	Calcined Alumina
ZPC	The Zero Point of Charge

IEP Isoelectric Point

ZCC Zero Cement Castable

CPFT Cumulative Percent Finer Than

PEI Polyethyleneimine

CA Citric Acid

Na-PAA Sodium Polyacrylate Acid

TPP Sodium Tripolyphosphate

HMP Sodium Hexametaphosphate

PBTCA Phosphonobutane Tricarboxylic

MCC Medium Cement Castable

CS Conventional Castable

m-ZrO₂ Monoclinic Zirconia

t-ZrO₂ Tetragonal Zirconia

c-ZrO₂ Cubic Zirconia

YSZ Ytria Stabilized Zirconia

PSZ Partially Stabilized Zirconia

Y-TZP Ytria-Stabilised Polycrystalline Tetragonal Zirconia

M_S Start Temperature for Martensitic Transformation

X_{cr} Critical Ytria Content

EPMA Electron Probe Micro Analyzer

EF Edge Fracture

COD The Crack Opening Displacement

CMOD The Crack Mouth Opening Displacement

CTE Coefficient of Thermal Expansion

ACKNOWLEDGEMENTS

I would first like to thank to my advisors, Professor Hugo Lopez and Associate Professor Konstantin Sobolev for their guidance and support during this work. I would also like to thank to Dr. Steve Hardcastle for his assistance in the characterization of samples and Assistant Professor Ben Church for his support. In addition, I would like to thank to Dale P. Zacherl and Steve Kowalski from Alcoa to supply the raw materials for the experiments. Lastly, I would especially thank to my family members for their caring support throughout my years of education.

CHAPTER 1 – INTRODUCTION

Refractory materials, by definition are supposed to be resistant to heat and are exposed to different degrees of mechanical stress and strain, thermal stress and strain corrosion/erosion from solids liquids and gases, gas diffusion, and mechanical abrasion at various temperatures [1]. Development of the major consumer of the steel industry and also other industries such as aluminum, copper, glass and cement force the refractory industries to improve the quality of the refractories. The driving force for change is either improved process technology or longer campaign lives. As a consequence, it creates the most significant development in the refractory world that is the evolution of monolithic refractories in the last 50 years. Since 1960s to the present time there has been a steady increase in the use of monolithic refractories by refractory consuming industries. More than 50% of the production is monolithic refractories in many countries due to ease of installation and fixing and better corrosion resistivity of castables[1,2].

Use of submicron additions in refractory matrix is another development. It leads to decrease cement content in refractory matrix. Low cement castables (LCCs), ultra-low cement castables (ULLCs) have replaced a variety of other castables such as the conventional ones. In addition to decreasing water, less water is used to achieve the casting consistency in LCCs and ULCCs. That makes castables performance superior such as: improved cold and hot strength, reduced porosity, higher density and better corrosion resistance. Later on, a reduction in cement content was achieved with the

development of zero cement castables. Calcium aluminate cement (CAC) is replaced by a hydraulic binder such as hydraulic alumina [1,2].

Due to decreasing water content with decreasing cement there is poor flow in castables which makes it necessary the use of vibration for placing. This poses limitations in the filling of spaces without the presence of defects of complex shapes. In the mid 1980s, self-flowing castables (SFCs), which are LCCs or ULLCs with a consistency after mixing that allows them to flow and degas without application of vibration, joined the family of refractory concretes [3]. Particle size distribution (PSD) is one of the important factors controlling the flowability and porosity. Since the last century, several packing models have been presented. Furnas - Anderegg and Andreassen and Dinger - Funk (modified Andreassen) are the best known models in the refractory world. The model of modified Andreassen is the most commonly used among them. In this model, q is the distribution coefficient. Basically the lower q values indicate the finer the particles in the refractory. Results from Andreassen show that the q value should be lower than 0.25 for self flow property and around 0.30 for vibrationable castables[4-7].

Alumina based castables widely investigated according to the published literature [7-22] because alumina has high strength, hardness, thermal shock and good corrosion resistance. On the other hand, alumina has low toughness so fracture has always been a critical problem for refractories during their use. They can be strengthened by the addition of secondary phase ceramic particles. Y_2O_3 (yttria), CeO_2 (ceria), TiC , SiC , Al_2O_3 and ZrO_2 (zirconia) are successfully used as a secondary phase in the alumina matrix [23]. Among them ZrO_2 is getting more attention due to its high strength and good

toughness, even though it possesses relatively poor hardness. The strength and toughness of alumina may be enhanced by a dispersion of ZrO_2 solid solutions. Tetragonal- ZrO_2 grains undergo a monolithic transformation (stress induced phase transformation) and microcracks form around existing m- ZrO_2 grains. Consequently, toughness of Al_2O_3 - ZrO_2 is improved by both stress induced phase transformation and microcrack toughening of dispersed alumina[24-26].

The goal of this research is to develop nano- ZrO_2 reinforced self flow low cement (5%) and ultra low cement (3 and 1%) castables based on tabular alumina. The Andreassen model was used to obtain self flow property of both low and ultra low castables. After samples were fired at 110 and 1000, 1300 and 1500°C, the corresponding phases obtained were investigated in the castables by X-ray diffraction (XRD) with energy dispersive X-ray (EDX), scanning electron microscopy (SEM), thermogravimetric analysis (TGA) and differential thermal analysis (DTA). In addition, the cold crushing strength (CCS), apparent porosity (AP), bulk density (BD), water absorption (WA), weight loss (WL), zeta potential (ZP), flexural strength (MOR), fracture toughness (K_{IC}), indentation toughness and self-leveling flowability were all used in determining the various castable properties, as well as the exhibited microstructures. Then, castables with different amounts of (5%, 3%, 1%, 0.1% and 0.01%) of nano- ZrO_2 and YSZ (yttria stabilized zirconia) were fired at 1300°C in order to improve the flexural strength (MOR) and fracture toughness (K_{IC}) of castable samples. The results indicate that the addition of nano- ZrO_2 improves the performance of castables.

CHAPTER 2 - LITERATURE REVIEW

2.1 Refractory Castable Compositions

Refractories are a group of ceramic materials used in massive quantities to line vessels in which other materials (such as metals, glass and cements) are produced at elevated temperatures. They consist of large sized (up to centimeters) aggregates (filler) phases held together with finer (sometimes submicrometers), often porous, binder phases resulting in the microstructure shown schematically in figure 2.1.[2]

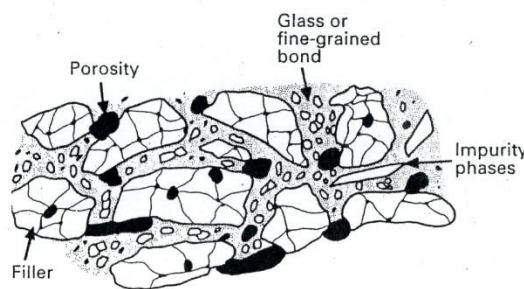


Figure 2.1 Typical powder processed refractory microstructure. [2]

The most significant trend in refractory technology since 1980 has been the ever increasing use of monolithics, or unshaped refractories. The reasons for the rapid growth of monolithic are their ready availability, faster, easier, and cheaper installation and fewer corrosion-susceptible lining joints. A significant advance in monolithic technology was the development of refractory concretes or castables based on calcium aluminate cements (CACs)[1,2].

Refractory castables may be characterized as structures of premixed combinations of refractory grain, matrix components, bonding agents, and admixtures. Table 2.1 lists the

general range of component quantities in a refractory castable. Refractory aggregate is the main component or the basic skeleton of the castable. The sizing of the aggregates can range between 20 mm to 300 μ m[1].

Table 2.1 Refractory Castable Composition[1]

<i>Aggregate</i>	<i>40-80%</i>
<i>Modifiers</i>	<i>5-30%</i>
<i>Bond agents</i>	<i>2-50%</i>
<i>Admixtures</i>	<i><1%</i>

The wide variety of refractory aggregates is available. Table 2.2 gives list the principal aggregates used in refractory castables[1].

Table 2.2 Primary Alumina and Alumina-Silicate Aggregates[1]

Aggregate	Al₂O₃ / SiO₂	Max. service limit (°C)
Alumina-tabular or white fused	99+ % / 0%	1870
Alumina-brown fused	94-98% / 1-2%	1760
Bauxite-S.A. and Chinese	84-90% / 5-7%	1760
Mullite-sintered and fused	74-76% / 19-24%	1760
Bauxitic kaolin-calcined	58-70% / 26-37%	1760
Andalusite	57-61% / 38-40%	1760
Calcined kaolin and flint clay	40-47% / 49-55%	1650
Pyrophyllite	13-30% / 65-80%	1425
Fused silica	0% / 99.7+%	1370

In addition to aggregates and binders, refractory fillers and/or modifiers are added in order to fill out the particle sizing and to impart other desired attributes such as expansion control, chemistry/mineralogy modification, bond enhancement. Table 2.3 lists the most common fillers and modifiers used in refractory castable compositions and their primary function[1].

Table 2.3 Common Refractory Fillers and Modifiers [1]

Filler/Modifier	Chemical formula	Function
Fine milled aggregates	Various	Chemistry, mineralogy and adjustment, bond modification and development
Alumina calcined	$\alpha\text{-Al}_2\text{O}_3$	Chemistry adjustment, bond modification and development
Alumina reactive	$\alpha\text{-Al}_2\text{O}_3$	Flow/rheology control, bond modification and development
Silica quartz	SiO_2	Shrinkage control (800°C)
Silica fume	SiO_2	Flow/rheology characteristics, bond modification and development
Kyanite	$3\text{Al}_2\text{O}_3 \cdot 3\text{SiO}_2$	Shrinkage control (1325°-1410°C), chemistry and mineralogy adjustment
Clay (fire, ball, bentonite)	Hydrated alumino-silicate	Filler, flow/rheology control
Zircon	ZrSiO_4	Reduce metal, slag, alkali attack
Graphite/Carbon	C	Reduce metal, slag attack
Fly ash	Varies	Low-temperature filler

The types of bonding agents used in refractory castables have increased in the past 20 years. Non-cement bonds such as: hydratable alumina, clay, silica and alumina gels and chemical bonds such as: momoaluminum phosphate, phosphoric acid, and alkali silicates are getting increasing attention over the years but still calcium aluminate cements (CACs) are used as the bonding agent in most refractory castables[1,2]. Table 2.4 lists the available types of CACs. In order to complete the refractory castable formulation, various types of additives or admixtures can be used. Table 2.5 lists the general types of additives and their functions in castable system[1].

Table 2.4 Calcium Aluminate Cement Types (CAC) [1]

	Chemistry (%)				Max. use tempt. (°C)
	Al ₂ O ₃	SiO ₂	CaO	Fe ₂ O ₃	
Low purity	36-48	3-9	35-40	7-16	1370
Medium purity- 50	51-53	4-5	37-39	1-2	1540
Medium purity- 60	57-59	4-5	33-35	1-2	1540
High purity-70	69-72	<0.5	27-29	<0.5	1870
High purity-80	79-82	<0.5	17-20	<0.5	1870

Usually, multiple additives are used in a single formulation. Additives are used in very small amounts typically >0.2% and may possibly change in function by varying the quantity used.

Table 2.5 General types of additives and their functions in the castable system.[1]

<i>Additive</i>	<i>Function</i>				
	<i>Accelerat or</i>	<i>Retarder</i>	<i>pH control</i>	<i>Water Reducer</i>	<i>Rheology Modifier</i>
<i>Lithium carbonate</i>	<i>x</i>				
<i>Calcium hydroxide</i>	<i>x</i>		<i>x</i>		
<i>Sodium carbonate</i>	<i>x</i>		<i>x</i>		
<i>Sodium bicarbonate</i>			<i>x</i>		
<i>Sodium citrate</i>		<i>x</i>		<i>x</i>	<i>x</i>
<i>Sodium Phosphate</i>		<i>x</i>		<i>x</i>	<i>x</i>
<i>Sodium polyacrylate</i>				<i>x</i>	<i>x</i>
<i>Polycarboxylate</i>				<i>x</i>	<i>x</i>
<i>Citric acid</i>		<i>x</i>			
<i>Boric acid</i>		<i>x</i>			

While conventional castables containing the largest amount of cement are the greatest percentage of those produced but use of reduced cement varieties like low cement castables (LCCs) and ultra low cement castables (ULCCs) have grown significantly over the past 30 years. This is because the CaO (calcia) present in the cement leads to deterioration in the high temperature properties of the castables. Refractory castables are dry granular materials which require water addition. Installation is by casting or pouring into place, vibration placement, trowelling or projection (spraying or shotcreting). Mechanical vibration may be used to assist the flow of the concrete or to enable mold filling with a low liquid content in the slurry. Some products can fill in molds without vibration and such concretes are called as a free or self-flowing. The process like wet

gunning or shotcreting, refractory compositions are premixed with water and then pumped under pressure to the site of placement where they are projected or sprayed on the surface[2]. In this process, the concrete is termed a shotcreting or sprayable castable (figure 2.2).



Figure 2.2 Wet-gunning of the ultra low cement bauxite based castable [27].

Modern castables are used increasingly in almost every refractory application, such as blast furnaces, steel ladles, rotary cement kilns, direct reduction kilns, coke oven door plugs, cyclones and transfer lines of fluidized catalytic cracking unit vessels of the petrochemical industry, foundry ladles and heat treating furnaces, aluminum reverberatory furnaces and ladles, boilers and waste incinerators seating (well) blocks and powder injection lances, desulphurizing and argon stirring lances, refractory lining of snorkels in RH degassing vessels and, more recently, fabrication of shrouds and submerged entry nozzles used for the continuous casting of steel[1,2].

2.2. Phase Composition

Refractory castables must “set” or harden at room temperature. Either water or another catalyzing agent must activate the bonds used in castables. After setting, a controlled

heat-up procedure is generally required to dewater or dehydrate the bond as the refractory castable lined vessel or furnace is put into service. The majority of alumina and alumina-silicate castables produced have historically been bonded with calcium aluminate cement (CACs). Where C:CaO, A:Al₂O₃, F:Fe₂O₃, S:SiO₂ and T:TiO₂.

Table 2.6 Typical mineral constituents of calcium aluminate cements [2]

Relative hydration rate	Cement purity		
	Low	Intermediate	High
Fast	C ₁₂ A ₇	C ₁₂ A ₇	C ₁₂ A ₇
Moderate	CA	CA	CA
Slow	CA ₂	CA ₂	CA ₂
	C ₂ S	C ₂ S
	C ₄ AF	C ₄ AF
Non-hydrating	C ₂ AS	C ₂ AS	CA ₆
	CT	CT	A
	A	A

Typical phases present in commercial CACs, based on their relative reaction rates with H₂O are listed in table 2.6. They form the hydrated cement phases responsible for developing strength after curing the concrete in a humid environment. Useful properties of these minerals are listed in table 2.7. Monocalcium aluminate (CaO.Al₂O₃ or CA) is the most important component of CACs since it generally happens in large amounts (40-70%), has a relatively high melting point (1600°C) and develops the highest strength among the phases listed during the relatively short time available for hydrating refractory concretes. It takes some time to start setting, but hardens rapidly after the initial set.

Table 2.7 Properties of CAC mineral constituents [2]

	Chemical composition, wt-%				T_m °C	Density g.cm ⁻³	Cold crushing MPa	Crystal System
Mineral	C	A	F	S				
C	99.8				2570	3.32		Cubic
C₁₂A₇	48.6	51.4			1415- 1495	2.69	15	Cubic
CA	35.7	64.6			1600	2.98	60	Monoclinic
CA₂	21.7	78.3			1750- 1765	2.91	25	Monoclinic
C₂S	65.1			34.9	2066	3.27		Monoclinic
C₄AF	46.2	20.9	32.9		1415	3.77		Orthorhombic
C₂AS	40.9	37.2		21.9	1590	3.04		Tetragonal
CA₆	8.4	91.6			1830	3.38		Hexagonal
α-A		99.8			2051	3.98		Rhombohedral

Calcium dialuminate (CA₂) is the secondary phase in CACs (<25%) and is more refractory than CA but takes an excessively long time to set though accelerated at high temperature. While hydration of CA is known to be accelerated by the presence of CA₂, the opposite does not hold true, and the hydration of CA₂ may actually be hindered by the presence of CA. The strength of CA₂ after three days hydration is comparable to that of the pure CA and, unlike in CA, it always increases with time[2].

CA₆ is the only non-hydrating phase in the pure calcium aluminate system and is often a reaction product in alumina castables bonded with high purity aluminate cement. It is

believed that CA_6 is mostly readily formed in alumina castables when using CA_2 as a precursor. More recently, studies on the properties and microstructure of the CA_6 phase have revealed its great potential as a strong thermal shock resistant, refractory material and its important role in the bonding of corundum and spinel aggregates. Figure 2.3 shows the morphology of CA_2 and CA_6 [2].

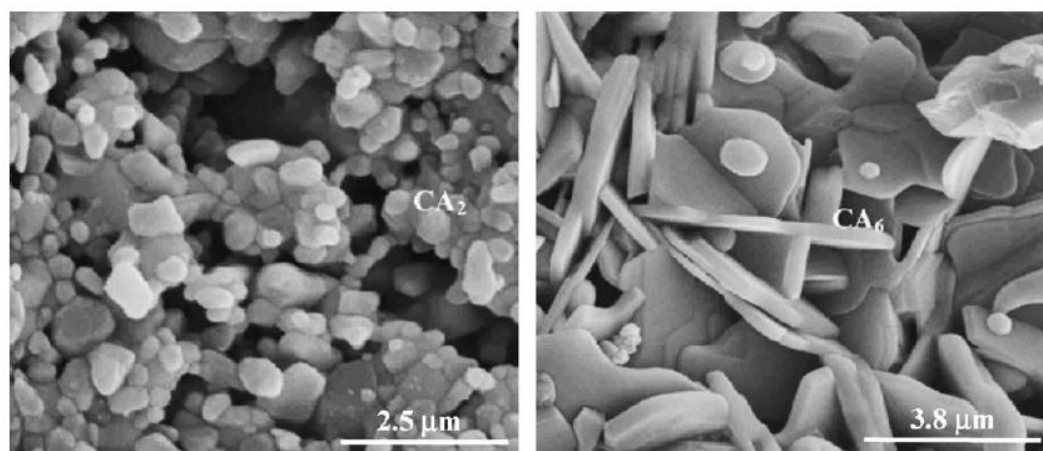


Figure 2.3 SEM micrographs of fracture surfaces of samples prepared using $CaO-Al_2O_3$: (a) sintered at $1300^{\circ}C$ and (b) sintered at $1550^{\circ}C$ for 2 hours, showing the evolution and morphology of CA_2 and CA_6 , respectively[2].

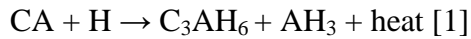
$C_{12}A_7$ hydrates rapidly and can be used to control the setting rate of CACs when used in small quantities: it has a relatively low melting point. C_2S and C_4AF are common in Portland cement, but can also occur in the high silica and iron rich low purity CACs respectively. C_4AF forms hydrates of calcium aluminate and calcium ferrite or solid solutions of the two hydrates and in its setting rate resembles $C_{12}A_7$. C_2AS (gehlenite) shows little tendency to hydrate and is an undesirable component of alumina cement which limits refractoriness and hot strength properties[2].

Generally, the characteristics of CACs are associated with the amount of alumina, lime and impurities present in the products. Increased alumina content will give higher

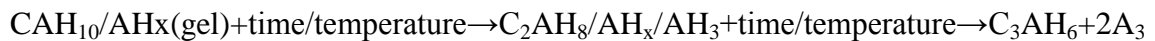
refractoriness, while high lime content in the cement increases cured strength. Iron impurities lower the carbon monoxide resistance at high temperatures, and siliceous compounds reduce resistance to hydrogen atmospheres under similar conditions[2].

2.2.1. Bonding Mechanism

Hydration begins when cement contacts water. As mentioned before, CA (calcium monoaluminate) is the principal and most important hydrating phase [1,2,28,29] CA hydrates according to the following reaction:



Where C=CaO, A=Al₂O₃, and H=H₂O. C₃AH₆ is the normal, stable hydrate phase when cement curing temperatures of >35°C occur in the castable mass. While this curing temperature may seem high, it is generally reachable because cement hydration is an exothermic reaction. Rather often internal castable temperatures can reach temperatures of up to 75°C or greater especially in high cement (20+%) formulations. If a curing temperature of 35°C is attainable, the metastable hexagonal hydrates of CAH₁₀ + AH_x (gel) (<21°C) and C₂AH₈ + AH_x + AH₃(21°-35°C) will form. CAH₁₀ can be detected after 6-24 hours. The presence of C₂AH₈ can be detected after 24 hours[1,2,28]. These hydrates will convert to C₃AH₆ per the following:



As the temperature increases above 21°C, the metastable hydrates CAH₁₀ and C₂AH₈ transform into the more stable compounds, C₃AH₆ and AH₃. The transitional crystalline

change from one calcium aluminate hydrate to another is commonly referred to as 'conversion'. However, with this conversion to the stable hydrate there is phase volume shrinkage that can disrupt the bond structure and lead to weakening of the bond[1,2].

The morphologies of the main CAC hydrates (listed in table 2.8) change extensively though, in general C_3AH_6 forms as cuboids, C_2AH_8 as platelets, CAH_{10} as needles or hexagonal prisms, and gibbsite as tablets or needles. When the castable is heated for the first time, the hydrated cement phase will undergo a dehydration process over a temperature range. Dehydration of the hydrated cement occurs over a temperature range from $210^{\circ}C$ to $370^{\circ}C$, with the peak dehydration temperature for AH_3 at $230^{\circ}C$ and for C_3AH_6 at $315^{\circ}C$ [1,2].

Direct formation of denser stable hydrates (AH_3 and C_3AH_6) at higher curing temperatures produces greater porosity and larger pore sizes than when the metastable and less dense hydrates (CAH_{10} and C_2AH_8) are formed at lower temperatures. While this gives rise to lower green strengths it also gives coarse, permeable hydrate phases so that the vapor species can escape on drying.

Table 2.8 Properties of CA cement hydrates[2]

Hydrate	Chemical composition, wt-%			Crystal System	Density g.cm ⁻³
	CAO	Al ₂ O ₃	H ₂ O		
CAH ₁₀	16.6	30.1	53.5	Hexagonal	1.72
C ₂ AH ₈	31.3	28.4	40.3	Hexagonal	1.95
C ₃ AH ₆	44.4	27.0	28.6	Cubic	2.52
AH ₃	--	65.4	34.6	Hexagonal	2.42

If the castable is heated too quickly and if released steam from the dehydrating cement cannot vent from the castable structure fast enough, internal pressure develops in the castable and steam spalls or explosions can happen. Many advanced castables also include fine powder additions and are packed to gain maximum density. That reduces the castable permeability and further complicates heat-up procedures. It is quite common to use organic, synthetic fiber additions in order to help reduce the possibilities of bake-out spall. Those additions melt or burn out at low temperatures (typically <200°C) to assist open the castable structure and ease the release of moisture. Polypropylene, acrylic, or polyester are the most common fibers used in lengths ranging from 3 mm to 10 mm and diameters of 15-40µm. The other method is to reduce the danger of explosive spalling. For this purpose, refractory CAC castables are generally cured above 27°C. Best practice for safe heating and maximum strength development is to cure for at least 24 h. at 30-38°C covered in an impermeable membrane to maintain a humid environment for hydration, followed by a 24 h. air cure with the surface exposed to 30-38°C. The increase in porosity and its effect on strength are also heavily influenced by original total water/cement ratio[2].

2.2.2. Dehydration and Firing

Strength loss is known to happen in hardened calcium aluminate pastes while the metastable hexagonal CAH_{10} phase dehydrates through the hexagonal C_2AH_8 transition phase into the stable cubic C_3AH_6 . This loss of strength can best be understood by considering the morphological and volume changes accompanying this conversion. When CAH_{10} is allowed to form during low temperature curing, the metastable hexagonal prisms (density 1.72gcm^{-3}) and gel (2.42gcm^{-3}) solidify. That eventually will convert to the stable cubic (2.52gcm^{-3}) type with time and/or temperature. The gross restructuring from H_2O loss leading to pore formation and nominal 50% volume shrinkage on conversion of CAH_{10} to denser C_3AH_6 and α - AH_3 (table 2.9) are disruptive to a rigid structure and account for the observed loss in mechanical strength[2].

Table 2.9 Dehydration temperature of CA cement hydrates[2]

Hydrate	CAH_{10}	C_2AH_8	C_3AH_6	AH_3
Dehydrating temperature, °C	100-130	170-195	300-360	210-300

As the temperature is increased, the dehydration process continues, until all phases lose their water of crystallization[1,2,28]. The compounds formed during hydration of CACs dehydrate up to around 550°C . The process of hydration followed by dehydration creates the anhydrous material which is extremely fine and active. Lime and alumina reappear and recombine in a way similar to that of the original raw materials in the kiln. Table 2.10 depicts the mineralogical changes in HACs as the temperature increases up to 1500°C [2].

Table 2.10 Mineralogical changes of dehydrated high alumina cement on heating[2]

Temperature(°C)	70% Al ₂ O ₃ CAC					80% Al ₂ O ₃ CAC				
	C ₁₂ A ₇	CA	CA ₂	CA ₆	A	C ₁₂ A ₇	CA	CA ₂	CA ₆	A
500	X	X	X
600	X	X	X
700	X	X	X	X
800	X	X	X	X	X
900	X	X	X	...	X	X	X	X	...	X
1000	X	X	X	...	X	...	X	X	...	X
1100	...	X	X	...	X	...	X	X	...	X
1200	...	X	X	X	X	...	X
1300	...	X	X	X	X	...	X
1400	...	X	X	X	X	X
1500	...	X	X	X	X	X

2.3. Surface Chemistry

Surface chemistry principles are rather important since they all involve the handling of suspensions (solid–liquid mixtures) containing colloidal particles (<1 µm) of relatively high specific surface area (>1 m²/g), which are more susceptible to the surface forces that take place at the solid–liquid interface. The magnitude of these surface forces controls the dispersion state of particles and the rheological behavior of colloidal suspensions. Advanced refractory castables usually have a broad particle size distribution so they contain a large fraction of micron- and submicron-sized particles (0.1–100 µm) in combination with coarse aggregates (>100 µm). Thus, aspects of the surface chemistry

and the dispersion state of the smaller particles (matrix) in water also play a major role in the processing and final properties of these refractory materials[1].

The term “agglomerate” is used to mean the relatively weak clusters of particles formed in the absence of efficient dispersing mechanisms. From this standpoint, agglomerates differ from the hard clusters of particles linked to each other by strong covalent bonds which are normally referred to as aggregates. Particle agglomeration must result from a strong driving force, which justifies the need for efficient dispersing mechanisms. This driving force derives from the Van der Waals attractive forces originated by the interactions between the permanent and/or induced inner electric dipoles of neighboring particles. Especially, alumina particles show a strong driving force for agglomeration in comparison to other materials. This is probably one of the reasons for the major role of alumina particles in the dispersion of multicomponent castable systems[1].

2.3.1 Dispersion Mechanism

The agglomerates formed through the action of the Van Der Waals attractive forces influence the rheological behavior and final properties of refractory castables (figure 2.4a). In terms of rheological properties, the agglomerates lead to an increase in the apparent viscosity and yield stress of the matrix suspension and a reduction in the castable’s flowability. Thus, higher water is needed to improve the fluidity of castables and that causes a reduction in the matrix suspension density and favors the segregation of dense and coarse aggregates. Increase in water amount leads to a more porous final

microstructure, reducing the mechanical, wear, and corrosion strengths of the refractory castables[1].

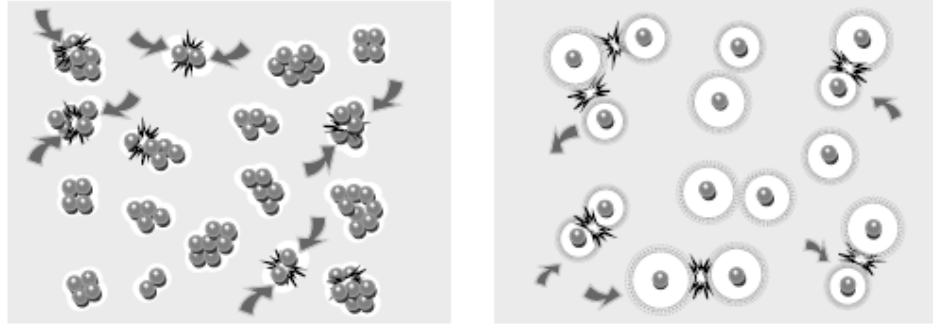


Figure 2.4 (a) Uncharged Particles are free to collide and aggregate **(b)** charged particles repel each other[30]

In order to prevent particle agglomeration (figure 2.4b), dispersing mechanisms are activated. The main methods used for this purpose are (1) electrostatic, (2) steric, and (3) electrosteric dispersing mechanisms. The electrostatic mechanism involves the development of electric charges on the surface of particles, inhibiting agglomeration through the formation of an electric double layer around the particles. In the purely steric mechanism, long-chain nonionic molecules are adsorbed at the particles surface to prevent their close approach by a physical hindrance effect. The electrosteric mechanism simultaneously combines the electrostatic and steric features of the previous mechanisms by the adsorption of relatively long-chain charged molecules on the surface of particles. All these mechanisms are expected to provide a repulsive force that counter balances the attractive effect of the van der Waals forces[1].

2.3.2 Electric Double Layer

In the electrostatic and electrosteric mechanisms, the repulsive force required to overcome the attractive van der Waals forces is developed through the formation of the so-called electric double layer around particles. Figure 2.5 shows a schematic diagram of the double layer. Initially, attraction from the negative colloid causes some of the positive ions to form a firmly attached layer around the surface of the colloid; this layer of counter-ions is known as the *Stern layer*. Additional positive ions are still attracted by the negative colloid, but now they are repelled by the Stern layer as well as by other positive ions that are also trying to approach the colloid. This dynamic equilibrium results in the formation of a *diffuse layer* of counterions. They possess a high concentration near the surface which gradually decreases with distance until it reaches equilibrium with the counter-ion concentration in the solution[1].

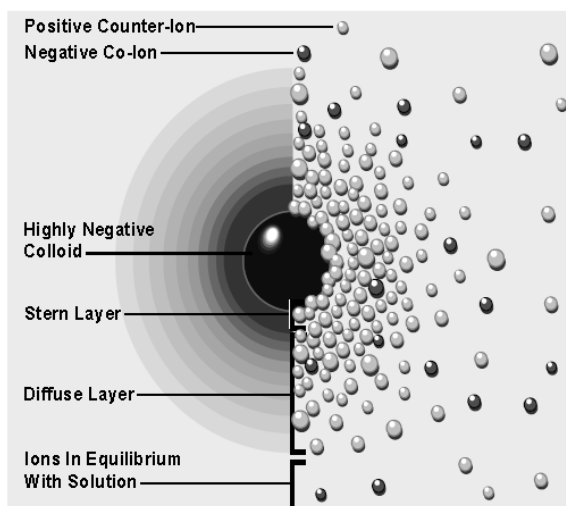


Figure 2.5 Schematic representation of the Double Layer[1]

In a similar, but opposite, fashion there is a lack of negative ions in the neighborhood of the surface, because they are repelled by the negative colloid. Negative ions are called *co-*

ions because they have the same charge as the colloid. Their concentration will gradually increase with distance, as the repulsive forces of the colloid are screened out by the positive ions, until equilibrium is again reached. The diffuse layer can be visualized as a charged atmosphere surrounding the colloid. The charge density at any distance from the surface is equal to the difference in concentration of positive and negative ions at that point. Charge density is greatest near the colloid and gradually diminishes toward zero as the concentration of positive and negative ions merge together. The attached counter-ions in the Stern layer and the charged atmosphere in the diffuse layer are what it is referred to as the *double layer*. The thickness of this layer depends upon the type and concentration of ions in solution[1].

2.3.3 Zeta Potential

The double layer is formed in order to neutralize the charged colloid that causes an electrokinetic potential between the surface of the colloid and any point in the mass of the suspending liquid. This voltage difference is of the order of millivolts and is referred to as the surface potential. The magnitude of the surface potential is related to the surface charge and the thickness of the double layer. Away from the surface, the potential drops off roughly linearly in the Stern layer and then exponentially through the diffuse layer, approaching zero at the imaginary boundary of the double layer. The potential curve is a useful one because it indicates the strength of the electrical force between particles and the distance at which this force comes into play[1].

A charged particle will move with a fixed velocity in a voltage field. This phenomenon is called electrophoresis. The particle mobility is related to the dielectric constant and viscosity of the suspending liquid and to the electrical potential at the boundary between the moving particle and the liquid. This boundary is called the slip plane and is usually defined as the point where the Stern layer and the diffuse layer meet. The Stern layer is considered to be rigidly attached to the colloid, while the diffuse layer is not. As a result, the electrical potential at this junction is related to the mobility of the particle and is called the zeta potential (see figure 2.6)[1].

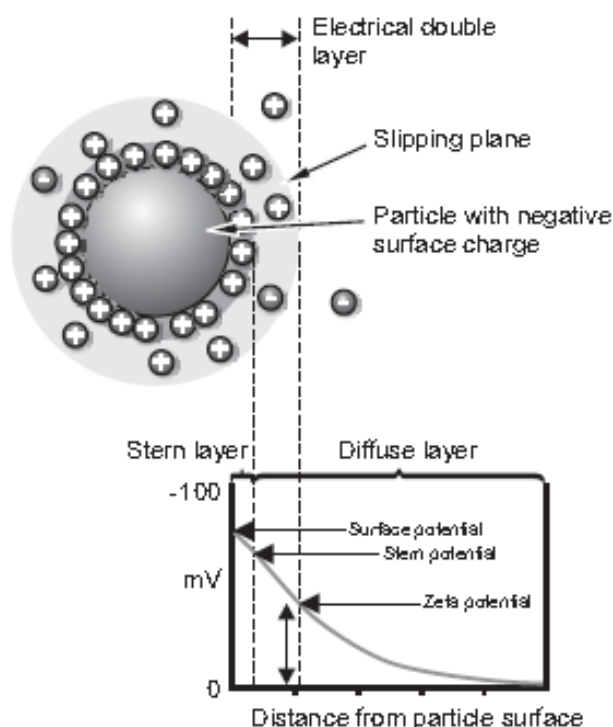


Figure 2.6 Schematic representation of zeta potential[1].

The magnitude of the zeta potential gives an indication of the potential stability of the colloidal system. If all the particles in suspension have a large negative or positive zeta potential then they will tend to repel each other and there will be no tendency for the

particles to come together. However, if the particles have low zeta potential values then there will be no force to prevent the particles coming together and flocculating. The most important factor that affects zeta potential is the pH. A zeta potential value on its own without a quoted pH is a virtually meaningless number. Figure 2.7 shows zeta potential as a function of pH. The point where the plot passes through zero zeta potential is called the Isoelectric point and is very important from a practical consideration. It is normally the point where the colloidal system is least stable. Zeta potential is the minimum at the isoelectric point so particles have a tendency to come together. A typical plot of zeta potential versus pH is shown below in figure 2.7[1].

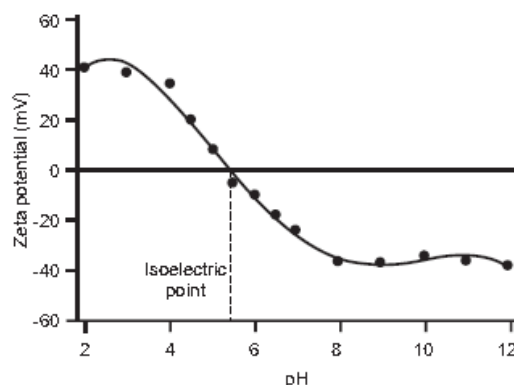


Figure 2.7 Zeta potential as a function of pH[1].

Figure 2.8 presents the variation of zeta potential as a function of pH for some finely grinded raw materials used in refractory applications. It is worth noting the markedly different zeta potential profiles of these raw materials.

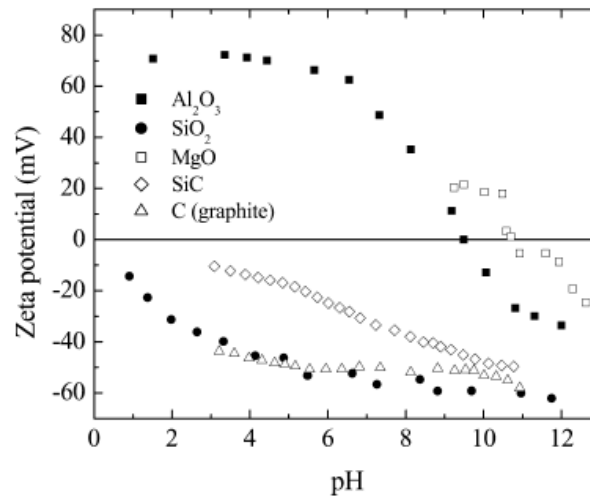


Figure 2.8 Zeta potential as a function of pH for some of the raw materials commonly used in refractory castables[1].

Otroj and colloquies investigated the effect of deflocculants on the self flow characteristics of ultra-low cement castables. Figure 2.9 shows the variation of pH as a function of deflocculant content for different types of deflocculants used[31].

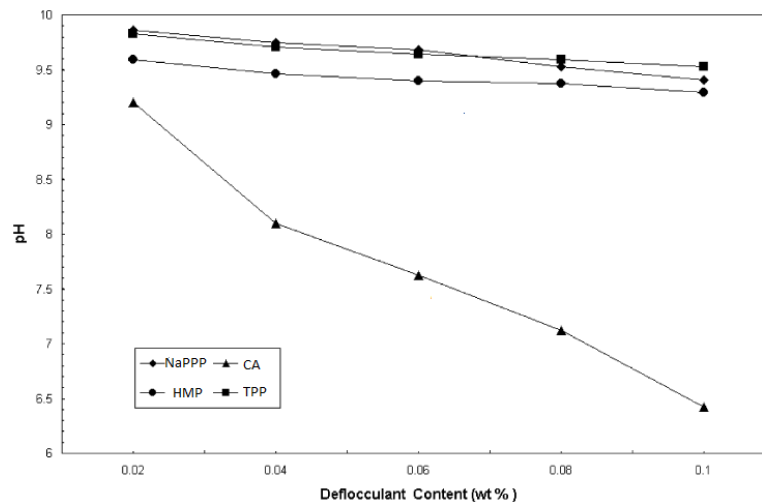


Figure 2.9 pH is as a function of the deflocculants content for the different types of deflocculants[31].

Their results showed that the addition of citric acid (CA) reduces the pH of the suspension to values as low as 6.5 due to its acidic nature. On the other hand, other

deflocculants (sodium polyacrylate acid (Na-PAA), sodium tripolyphosphate (TPP) and sodium hexametaphosphate (HMP)) have not produced such a dramatic change in pH values which remain relatively stable. Hence, it is important to add anionic molecules such as; citric acid to properly disperse high-alumina castables since alumina particles have a ZPC (The zero point of charge) corresponding to the usual pH range (8–10) of the castable.

Sun studied the influence of initial pH on nano zirconia powder. Figure 2.10 shows the effect of pH on the zeta potential of 3Y-TZP powder in a variety of NaCl solutions. He concluded that the isoelectric point of 3Y-TZP is near 6.8. The absolute value of zeta potential measured in 100M NaCl solution is lower than those measured in 1 and 10mM NaCl solution due to compression of the double layer in higher ionic strength[32].

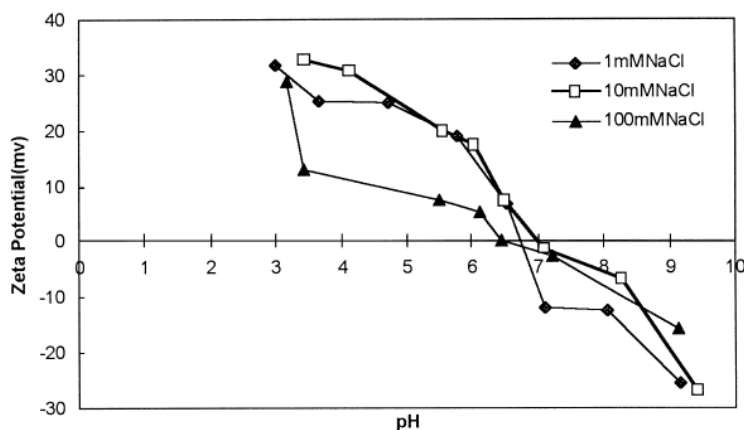


Figure 2.10 Zeta potential of aqueous 3Y-TZP suspensions at different pH values[27].

Lan and colleagues investigated the agglomeration on drying of 8wt.% yttria stabilized zirconia slurry. Figure 2.11 shows the SEM micrographs of green compacts dried from the slurries with different pH values[33].

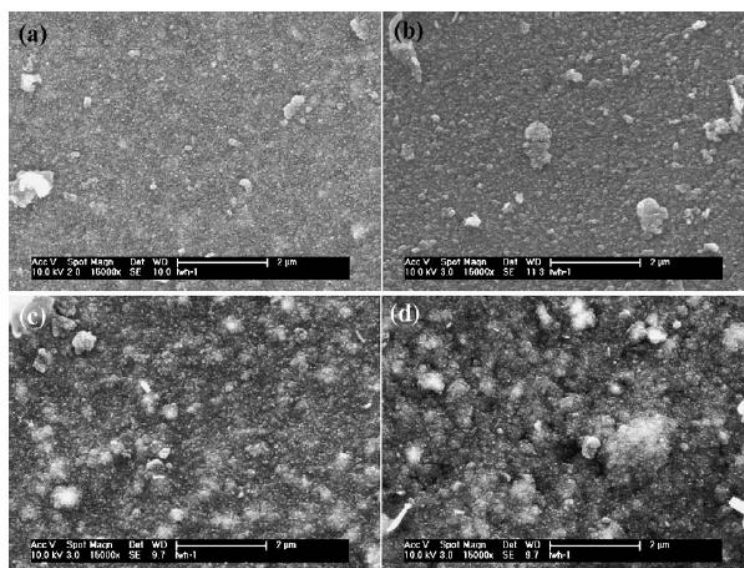


Figure 2.11 SEM micrographs of green compacts dried from the slurries with 47–50 wt.% solid content and pH values at (a) pH 3; (b) pH 4.5; (c) pH 5.5; (d) pH 7.5[33].

His results showed that green compacts dried from a dispersed slurry with pH 3 possess a dense microstructure, whereas green compacts dried from a strongly agglomerated slurry with pH 7.5 displays the least dense microstructure, in which large pores are present. Green compacts dried from weakly agglomerated slurries with pH 4.5, 5.5 show medium-dense microstructures. He concluded that the isoelectric point (IEP) was determined as 8 for Y_2O_3 stabilized ZrO_2 . The zeta-potential decreases with increase of the pH value from 3 to 7.5. The slurry with pH 7.5 displays strong shear thinning behavior and high viscosity, indicating a high agglomeration degree. This is attributed to the comparatively lower zeta potential at a pH value close to the IEP.

Greenwood and Kendall studied the effect of time after mixing on the zeta potential of a 3 mol% Y_2O_3 stabilized ZrO_2 (see Figure 2.12). Notice that the Zeta potential increases by 5mV over a period of 6h so particle size distribution decreases with time[34].

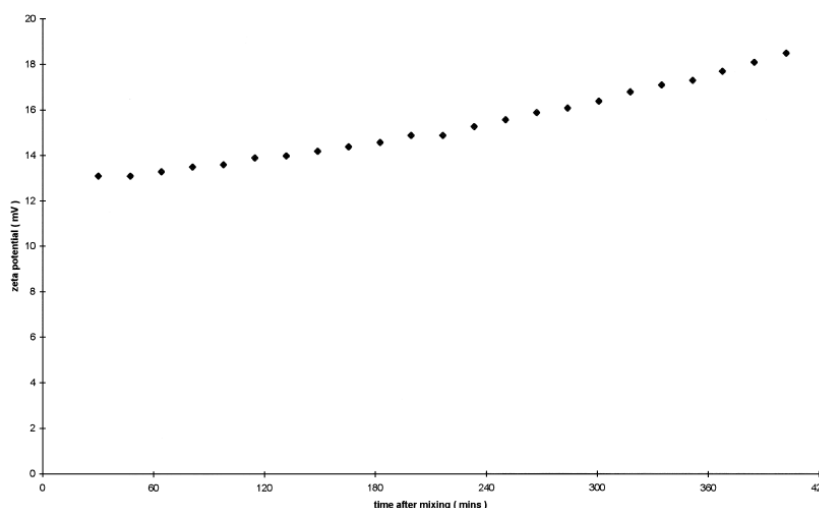


Figure 2.12 Effect of time on the zeta potential of a suspension prepared from the Tosoh zirconia powder[34].

They concluded that the yttrium ions could precipitate on the powder surface so a positive charge builds up with time. This increase in the zeta potential with time corresponds to an increase in stability; as a result the particle size decreases as the aggregates break down into smaller units.

2.3.4 Dispersants

The dispersion of refractory castables is usually accomplished by developing electric charges with the same signal on the particle surfaces. However, a brief glance at the zeta potential curves of powders indicates that it is impossible to promote particle dispersion simply by controlling the suspension pH. This is due to the fact that the raw materials display dissimilar surface charges over a very broad pH range. Even in the case of simple refractory compositions, substantial pH shifts are not expected to favor particle dispersion. This is due to the large contents of acid/alkaline compounds usually required to change the pH of castables, which would substantially increase the ionic strength of

the liquid medium. Considering these factors, the most common method to disperse refractory castables is the addition of specific charged molecules (dispersants), which can absorb and provide charges with the same signal on particle surfaces[1].

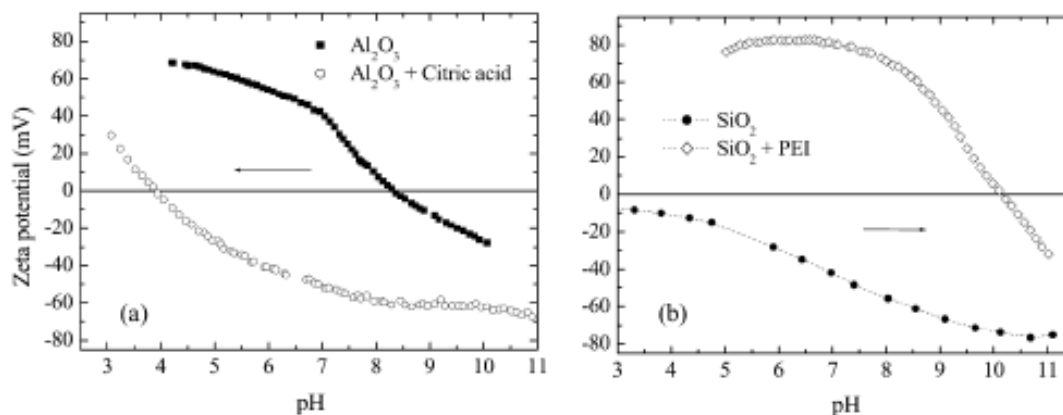


Figure 2.13 Examples of the effect of (a) anionic (0.06 wt% citric acid) and (b) cationic (0.33 wt% polyethyleneimine, PEI) dispersants on the zeta potential curve of alumina and silica particles, respectively[1].

Figure 2.13 shows the ability of anionic and cationic dispersants to modify the surface characteristics of ceramic powders in water. As it is seen from figure 2.13, the anionic species causes a shift of the zeta potential curve towards acidic values, leading to negatively charged particles over a broad pH range. The opposite behavior occurs in the case of the cationic dispersants, whose adsorption produces a positive net charge on the surface of silica particles within a wide pH interval[1].

It should be mentioned that the charged sites of such molecules should be able to establish relatively strong interactions with the surface groups so as to actually modify the surface chemistry of the particles. This can occur through the formation of either primary bonds or coordinated interactions among the dispersant molecules and the surface groups. This characteristic distinguishes the action of dispersants from that of the

counterions of the Stern and diffuse layers, which, rather than reacting with the particle surface, simply exert a screening effect on the electric potential surface[1].

2.4. Types of Refractory Castables

Refractory castables are classified by The American Society for Testing and Materials (ASTM) according to their lime content[1,2,10,13,35,36]:

- Conventional Castables ($\text{CaO} > 2.5\%$)
- Low Cement Castables ($2.5\% > \text{CaO} > 1.0\%$)
- Ultra Low Cement Castables ($1\% > \text{CaO} > 0.2\%$)
- Cement free Castables ($\text{CaO} < 0.2\%$)

Castables can be also classified in various ways since they are a diverse group of materials. The primary division of castables is based on chemistry. The division separates the refractory castables based on alumina and alumina-silicate aggregates from the castables based on basic refractory oxides such as magnesite and dolomite. A more detailed classification[1]:

1. Chemistry and/or mineralogy
 - a. Alumina content/refractoriness (i.e., superduty, 60% alumina etc.)
 - b. Mineral base (i.e., mullite, fused silica, etc.)
2. Density/thermal insulating value
 - a. Dense ($> 1920 \text{ kg/m}^3$)
 - b. Medium weight ($1600\text{-}1920 \text{ kg/m}^3$)
3. Cement Content (by CaO from cement)
 - a. Conventional Castables ($\text{CaO} > 2.5\%$)
 - b. Low Cement Castables ($2.5\% > \text{CaO} > 1.0\%$)
 - c. Ultra Low Cement Castables ($1\% > \text{CaO} > 0.2\%$)
 - d. Cement free Castables ($\text{CaO} < 0.2\%$)

4. Flow/placement characteristics

- a. Vibrating
- b. Casting
- c. Free-flow
- d. Shotcrete

2.4.1. Conventional Castables

Conventional refractory castables contain 15-30% calcium aluminate cement (CAC) acts as a lubricant in water suspension and as a binder after hardening to give mechanical strength at room temperature. The properties of these concretes depend largely on the choice of refractory aggregate and hydraulic cement. The cured strength of conventional castables is due to the formation of various cement based hydrated phases. Because of the high cement content in conventional castables, they have relatively high in water content (8-15%)[2].

The functions of water in refractory castables are:

- 6 – 10 % water reacts with cement to form hydrated phases and to make the concrete flow. The reminder of 2-6% water is for proper installation.
- 0-5 % water is often taken up by the porosity of the aggregates and does not contribute to the hydraulic bond.

2.4.1.1. Disadvantages

These high cement castables have three major disadvantages. First, they are usually porous and open textured because they need large water contents, which greatly reduces their strength. The low porosity and permeability of castables at temperatures below 21°C

is caused by the alumina gel formed upon curing. The open porosity of conventional castables dried at 110°C is usually about 9-17%, but can be as low as 8%. Although some of this porosity is because of entrapped air bubbles, the most porosity is caused by the excess water added on mixing. On heating, the hydraulic bond is first modified, as conversion occurs and then destroyed by the dehydration process. During this textural modification, the pore size distribution changes and porosity grows significantly. The new porosity depends on the amount of chemically bonded water and is therefore dependent on cement type and content. The final open porosity of conventional refractory concretes fired at 1000°C generally varies from 22 to 26%, depending on the type of aggregate used[1,2].

Second, conventional castables show a characteristic drop in strength at intermediate temperatures (often quoted to be between 538 and 982°C), when the hydraulic bond has already broken down, due to the dehydration process, but the still sluggish sintering has not yet allowed the development of a ceramic bond. The exact temperature range when strength deteriorates is not absolute, but may depend on various factors, such as the type and proportion of hydrates, the curing temperature, and heating schedule. Early attempts to accelerate the formation of a ceramic bond generally consisted in making additions of various fluxes, most of which did little good and usually reduced the maximum temperature of use. Values for the cold crushing strength of conventional refractory castables fired at 1000°C usually vary from 10 to 30 MPa, averaging around 60% of the strength after drying[2].

Finally, the high lime content of these castables favors the formation of a fluid vitreous phase at high temperatures via the eutectic liquid in $\text{CaO-Al}_2\text{O}_3\text{-SiO}_2$ (CAS) ternary system which may encourage crystal formation but often remains as a glass or low melting anorthite and gehlenite on cooling which degrades refractoriness and corrosion resistance. The volume of viscous phase in refractory castable for a given temperature and refractory aggregate is mainly determined by the impurity content of the binding phase, i.e. by the composition and amount of cement used. Even with a high purity CAC containing 70-80 % Al_2O_3 , it is impossible to reduce the CaO content of conventional castables to less than 3%, which is still a large amount, particularly if silica containing aggregates are used. Further reduction is only possible by reducing the cement content[1,2].

Unlike fired refractory bricks, whose final properties are largely fixed before reaching the user, a refractory concrete has properties which evolve and alter for a considerable time after it has been put into use. In the case of refractory concrete it is the behavior at the service temperature which is more important than the unfired strength. By the end of the 1960s, there was little doubt about what should be done to improve the performance of refractory castables. Reducing the amount of cement without impairing other properties of the material proved difficult and challenging. However after several attempts it finally led to the development of a new range of products: the low and ultra low cement castables[1,2].

2.4.2. Low and Ultra Low Cement Castables

The first attempts to improve LCCs having excellent cold and hot strengths were unsuccessful since mechanical resistance was insufficient with less than 10% cement. In 1969, Prost and Pauillac improved LCCs (5-8% cement) without any reduction in strength. However they were very sensitive to rapid heating, mainly because the chemically bonded water released in a much narrower temperature range. This led to explosive spalling since the outer layers closed off and internal water pressure built up. Further improvements led to the development of concretes characterized by a pseudozeolithic bond, which releases the chemically bonded water slowly between 150 and 450⁰C, rather than within a narrow temperature range. This minimized the problems associated with explosions during heating but, because LCCs and ULCC s are dense materials with low permeability, baking out is always difficult, especially in thick installations[1,2].

The idea was to reduce the water requirements by eliminating the intergranular voids, which are often filled with excess water during the castable placement. This was achieved by carefully grading the particle size distribution so that interstices were progressively filled by smaller particles to gain the maximum packing density. Water requirements were further reduced by proper selection of defloculants and water reducing agents, which prevented coagulation of the fine powders and improved dispersion. The reduction in the water content required for vibration casting and maximizing of the packing density means these have higher density, low porosity and good mechanical and abrasion

resistance. Low and ultra-low cement castables usually require 3-7% water for placement, depending on the grade[1,2].

To appreciate fully modern refractory castables the interrelation between particle packing, dispersion technology, and rheology is critical (Figure 2.14). Understanding the relation between the first two of these gave rise to the new range of LCCs and ULCCs, while incorporating the third further improved the overall understanding of the technology and allowed the development of SFCs[2].

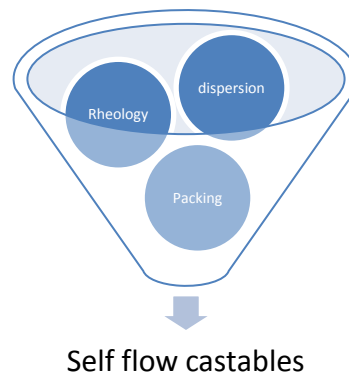


Figure 2.14 Relations between particle packing, dispersion and rheology[2]

Evangelista studied how to control the formulation and optimization of self-flow castables based on pure calcium aluminates. His results show that free flow behavior is obtained through the correct selection of the components of the refractory matrix and of the volume ratio between matrix aggregates. In addition it is necessary to optimize multiple additives for each specific system[3].

2.4.2.1 Particle Packing, Dispersion and Rheology

The main goal behind LCCs and ULCCs is to reduce the water requirement for placement while maintaining strength. Minimizing the water addition has been one of the major tasks in the development of castable technology[1,2]. Practical means of the reducing the cement and the water level consist of:

- Proprietary mixtures of chemicals, which improve the rheological behavior of the system and the setting process
- Ultrafine reactive powders which replace part of the cement of conventional castables and when used appropriate dispersant, fill the voids between larger which would otherwise filled with water.

Basically, the aim of the refractory industry is to get as dense refractory structures as possible. A major breakthrough in the development of this technology was the realization that this could be accomplished by improving the packing density of the material. The use of particle size distribution (PSD) in the construction of refractory castables has the recent few years become more common to achieve high dense castables. Although 100% packing density is not achievable, control of the particle size distribution of a castable is of vital importance[5,9,37]. Mainly for two reasons:

- Whether the castable is of a vibratable or a self may be decided flowing type by the particle size distribution. It is possible to design a castable to be either by using PSD analyses.

- Although 100% packing density is contradictory to flow, a solid structure with optimum packing theoretically requires less water for placement than castables with imperfect packing.

The particle size distribution (PSD) of the castables is a key factor to improve the flowability and density of the mix. The fine and ultra fine particles can increase the separation distance between aggregates and improve flowability. There are number of models have been presented over the years. The most commonly known models are Furnas - Anderegg and Andreassen and Dinger - Funk (modified Andreassen) [5,9,37].

The model of Furnas and Anderegg is however difficult and complicated to use. The model of Andreassen is much simpler but it has been criticized because of its semi-empirical nature. One interesting aspect of the Andreassen model is that it does not require any shape factor. It only requires the different particles to be of similar shape. The main objection that has been raised against the Andreassen equation has been that the model supposes infinitely small particles since real systems are finite. To overcome this problem, Dinger and Funk, by combining the Andreassen and the Furnas distribution, made a modified Andreassen distribution in which a minimum particle size was incorporated. The resultant model is much easier to use than the one given by Furnas, and is frequently called the "modified Andreassen" or the "Dinger and Funk" equation. Below is given the models as proposed by Furnas, Andreassen and Dinger and Funk (modified Andreassen)[5,9,37]:

- **Furnas :**

$$\frac{CPFT}{100} = \frac{r^{\log d} r^{\log D_s}}{r^{\log D_L} r^{\log D_s}} \quad [2.1]$$

- **Andreassen :**

$$CPFT = \left(\frac{d}{D_L} \right)^q \times 100 \quad [2.2]$$

- **Modified Andreassen (Dinger-Funk):**

$$CPFT = \left(\frac{d^q - D_s^q}{D_L^q - D_s^q} \right) \times 100 \quad [2.3]$$

CPFT: Cumulative percent finer than

r: Average particle size ratio

d: Particle size

D_s: Minimum particle size of the distribution

D_L: Largest particle size

q: Distribution coefficient (q-value)

One important aspect when dealing with particle size distributions is that they are always based on volumes. So for mixtures of powders with different densities, the amounts always have to be transformed to volumes in order to give volume percents. The parameters of the Andreassen and the modified Andreassen equation are the same i.e. the q-value is identical for both. One important result presented by Dinger and Funk was the influence of the q-value on packing. Using density values made it possible for infinite distributions. There is always porosity q-values above 0.37 so the q-value should not exceed 0.37 to get dense packing[5-9,37].

The Furnas distribution has been widely used in refractories. A common experience when using this distribution on castables has been that flow is improved by adding more of the finest fraction by adding more of the superfines change the distribution from a Furnas type towards an Andreassen type. Thus, despite the imperfections of the Andreassen distribution, it has been found that it works better for refractory castables than those of the Furnas type on systems with microsilica. Results from systems based on the Andreassen equation have indicated that in order to get good flow for castables, the q -value should not exceed approximately 0.3. Model systems based on fused alumina have shown that for 0.2 to 0.3, the flow pattern of the castables may be influenced by manipulating the q -value in the range. If relatively high q -values are used (i.e. close to 0.3), the castables are vibratables. On the other hand, self flow is dominant for lower q -values (<0.25)[5-9,37]. Myrhe used different q values in Andreassan model to determine self flow values based on ultra low cement castables[9]. Figure 2.15 shows free flow of ultralow-cement castables (ULCCs) with different particle size distributions as a function of time. His results show that the free flow is significantly influenced by the q -value, lower q value gives higher free flow.[9]

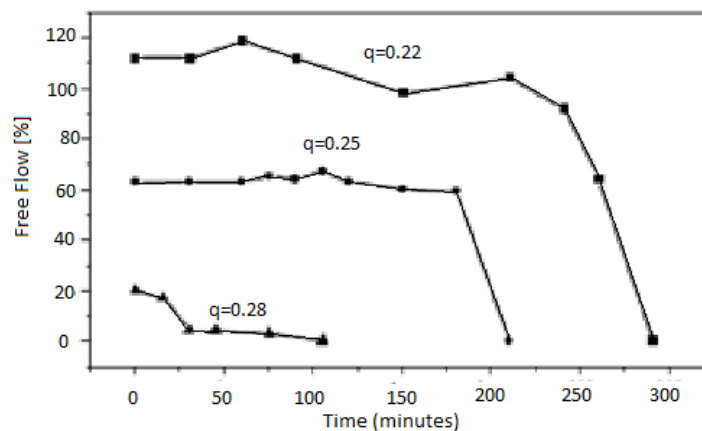


Figure 2.15 Free flow as a function of time and particle size distribution at 20°C[9]

Thus, it is possible to design either type of castable by manipulating the PSD. The effect of reducing the q -value is an increase in fines content. Particle interactions are essential for flow of castables, that is especially between coarser particles, so that an increase in the content of fines effects a separation of the coarser particles. A separation of the particles by viscous liquid containing water together with fines and superfines seems to be essential for creating flow in such systems[5-9,37]. Zhou used different q values in Andreasan's model to determine self-flow property of castable mixes[14]. Table 2.11 shows these compositions based on different q values[14].

Table 2.11 Details of Castable mixes[14]

Composition	CM-1	CM-2	CM-3	CM-4
Andreasen modulus, q	0.23	0.26	0.29	0.26
D_{max}, mm	5	5	5	8

Then, he measured self-flow properties of castables after mix for 30 minutes in Figure 2.16. His results show that self-flowability of all compositions looks similar at 0 min. After 30 min, CM-1 has shown considerable increase in self-flowability while observing little increase for composition CM-2. In the case of composition CM-3 and CM-4, there is a decrease in self-flowability due to segregation. Also, he indicated that it would be better to limit the maximum particle size since CM-2 and CM-4 have same q value but CM-2 shows better self-flowability after 30 minutes[14].

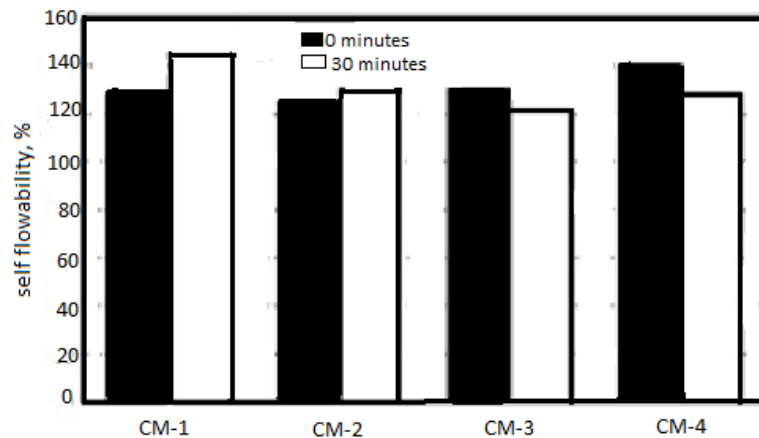


Figure 2.16 Comparison of self-flowability of castables[14]

However, the idea of reducing the water requirement for placement by simply improving the packing density of the castables would not have been successful without the proper use of superplasticizing additives to allow adequate dispersion of the submicrometer powders. Different types of additives or admixtures may be used to modify the flow/rheology characteristics of the castables, control setting behavior (retarding or accelerating), reduce casting water, stabilize/control the cement paste's pH, or stabilize storage behavior. In many cases, multiple additives are used in a single formulation. Additives and admixtures are used in very small amounts, usually between 0.05 and 0.5% [1,2].

A.R. Studart researched at selection of dispersants for high alumina zero cement refractory castables [15]. Gallic acid and 2-phosphonobutane-1,2,4-tricarboxylic (PBTCA) were used to investigate the dispersing efficiency. The free flow value of zero-cement high-alumina castables containing 14 vol.% water (4.12 wt.% based on dry solids) is presented in Figure 2.17 as a function of the dispersant content. His results indicate that such compounds are able to efficiently disperse zero-cement high-alumina

castables, enabling a reduction of their water consumption for a given fluidity level in comparison to those dispersed with citric acid[15].

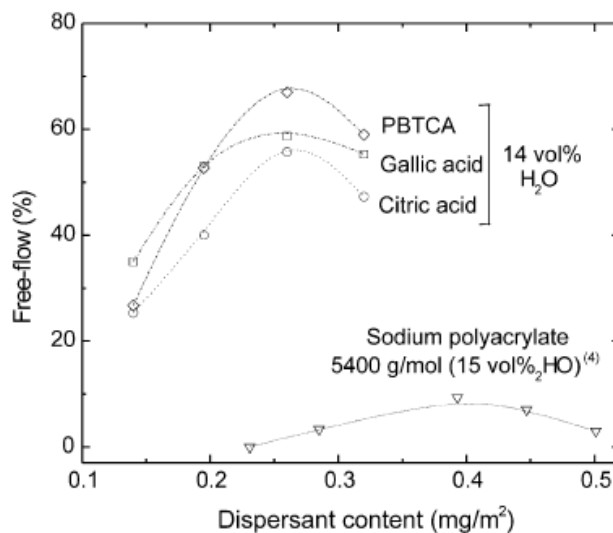


Figure 2.17 Free-flow value of castables as a function of the dispersant content for compositions dispersed with citric acid, gallic acid and PBTCA (14 vol.% water)[15]

Refractory castables consist mainly of fine powders, aggregate, and water and it is generally agreed that the workability of the material is governed by the flow properties of the fine powders. Therefore, the study of abnormal flow properties in a fine powder-water system, such as slurries and pastes, is important[1].

2.4.2.2 Properties

The main technical advantages of LCCs and ULCCs are their excellent physical properties, such as high density, low porosity, high temperature and “cold” room temperature strength, and high abrasion and corrosion resistance. The porosity and mechanical strength of refractory castables vary with temperature. A conventional castable has an open porosity of about 9-17% after drying and around 20-30% after heat

treatment at 1000°C. Most LCCs have an open porosity not higher than 10% and 16% after drying and firing, respectively[2].

M.A. Serry, studied at bauxite based low and ultra low cement castables. His results show that after firing at 1400°C, apparent porosity values between 10-15% and cold crushing strength values between 40-65 MPa[16]. Low cement castables usually possess a much finer pore size distribution than conventional high cement castables. In turn, this further contributes to increase the corrosion resistance, by hindering the penetration of metals and slags. The cold strength of LCCs rises steadily with temperature and is often higher than that of a conventional castable of similar composition at all temperatures after dehydration.

S. Goberis studied the properties of conventional castables (CS), medium cement castables (MCC) and low cement castables (LCC)[38]. In Figure 2.18, results show that at elevated temperatures, LCC samples have higher CCS values than both, CS and MCC specimens. The reasons are the recrystallization of minerals at 800°C and formation of bonding by the sintering process at 1100- 1300°C[38].

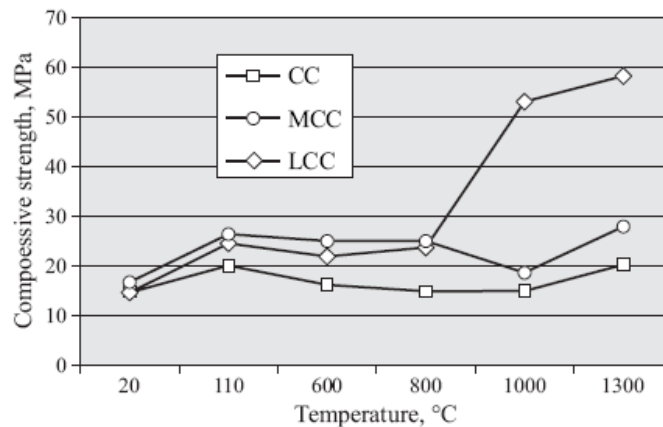


Figure 2.18 Compressive strength in castables heat-treated at different temperatures[38]

Zawrah investigated the effect of mullite formation on the properties of refractory castables[39]. He prepared four different refractory compositions based on different content of CAC's. In figure 2.19, castable 1, 2, 3 and 4 refer to 15, 10, 5 and 2 % CAC's respectively.

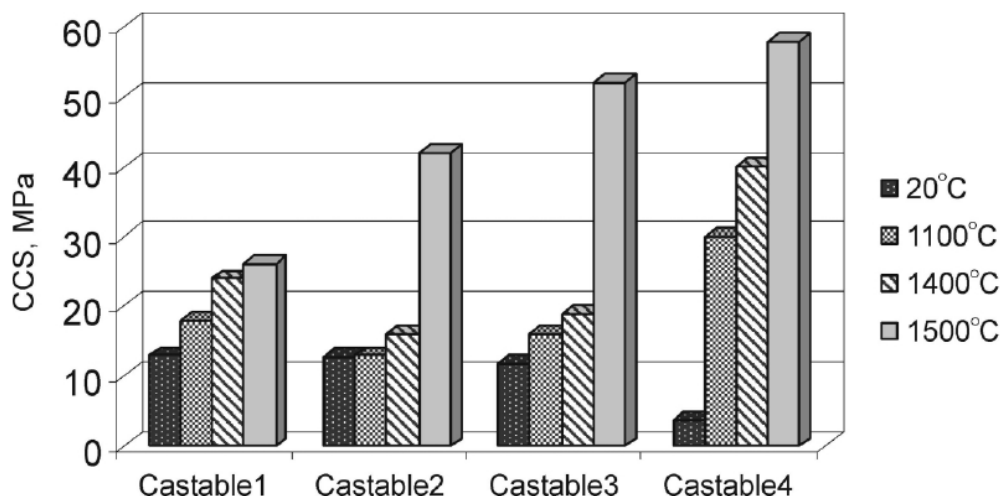


Figure 2.19 CCS of different castable samples fired at different firing temperatures[39]

Figure 2.19 shows that at lower temperatures high cement content castables show better strength values while low cement castables show lower Cold compressive strength (CCS) since the amount of cement is very little to promote bonding. On the other hand, Castables 3 and 4 containing the least amounts of cement (5 and 2wt.%, respectively) show the highest values of CCS at increased temperatures, this is attributed to the formation of mullite, a mineral that forms a network of mullite needles strengthening the structure and providing better performance at high temperatures[39].

There is increasing interest in the use of new bonding agents with superfine materials. Zawrah studied the effect of zircon additions on low and ultra low cement alumina castables[40]. Figure 2.20, ZOA, Z2A, Z4A, Z6A and Z8A show the effect of 2, 4, 6,

and 8 wt.% zircon additions (cement replaced by zircon) respectively. These results show that at elevated temperatures, castables with increased zircon dosage have improved cold crushing strength values. This is because of decreasing cement and increasing of m-ZrO₂ mullite-corundum or m-ZrO₂- corundum within the composite matrix[40].

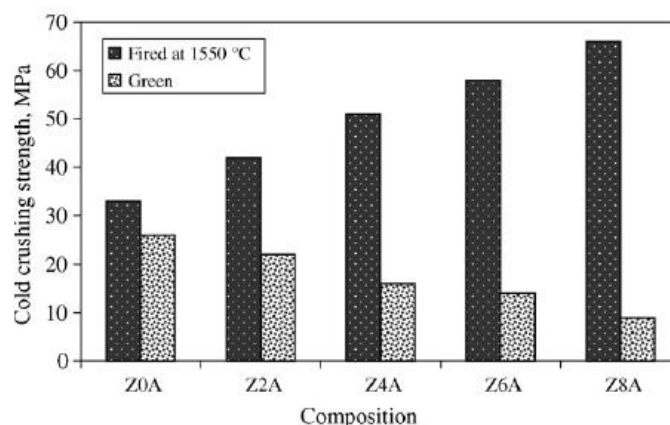


Figure 2.20. Cold crushing strength of alumina castables[40].

Mukhopadhyay used mullite and spinel sols as bonding agents in a high-alumina based ultra low cement castables[41]. Figure 2.21 shows the performance of castables with (M) and (S) mullite and spinel sols respectively. It was found that mullite is a promising material as an additive in ultra low cement castables demonstrating better CCS values than spinel sol containing castables[41].

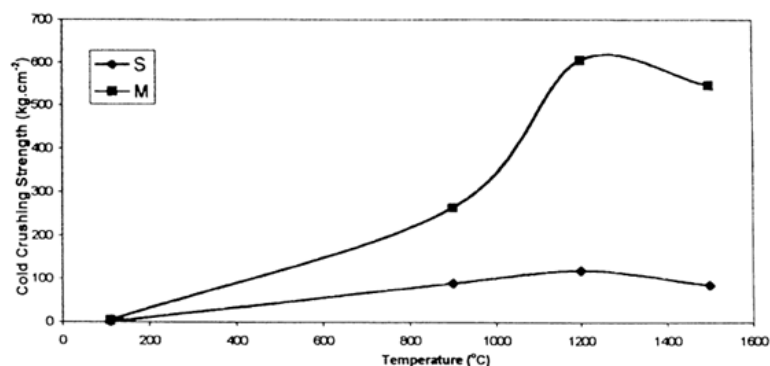


Figure 2.21 Cold crushing strength of ultra low cement castables vs. heating temperature[41].

Low cement castables (LCCs) usually have higher modulus of rupture and lower creep values than conventional high cement castables. All these characteristics provide superior performance over conventional (high cement) castables and other monolithic materials, such as ramming mixes, plastics, and gunning refractories. However, high cement castables are more robust with regards to installation and cast procedures, and ease of placement. In contrast, LCCs and ULCCs are more sensitive to installation parameters and possible variations in water content and casting conditions (such as the ambient temperature that may affect pot life, hardening time, and strength)[2].

2.4.3. Zero-Cement or Cement Free Castables

Zero-cement castables are used in numerous molten iron steel contact applications, where the elimination of lime in the refractory matrix increases the maximal use temperature. These usually do not show the superior performance and mechanical properties of LCCs and ULCCs, but they have a better corrosion resistance in respect to molten metals and slags. Zero cement castables (ZCCs) utilize the diversity of bonding systems like clay minerals, silica gels, hydratable aluminas, and phosphates[2].

Hydratable aluminas have attracted attention among the different binding systems for zero-cement castables (ZCCs). The first reported applications came from Japan in the early 1980s. Hydratable aluminas are amorphous mesophase transition aluminas which, similar to cement, harden hydraulically. These are produced by the rapid dehydration of gibbsite ($\text{Al}(\text{OH})_3$). In contact with water, γ -alumina rehydrates, forming pseudoboehmite ($\text{AH}_{1.2}$) and bayerite (AH_3). During heating, the hydrated phases lose their chemically

bound water, giving rise to the stable form of alumina ($\alpha\text{-Al}_2\text{O}_3$), which, at higher temperatures, will help to develop a strong ceramic bond[2].

The hardening reaction of transition alumina can be accelerated by the inclusion of alkali metal salts or delayed by the use of carboxylic acids. When used as a substitute for the cement, transition aluminas are usually combined with microsilica to promote the formation of mullite at high temperatures and to improve hot strength. In order to control the setting time of the castable, it has been found that some small additions, usually around 0.5% of CAC may be necessary. This is because a castable with a low hydraulic alumina content will not set. Higher additions of hydraulic alumina would require the increase of mixing water to maintain the flow however, this solution increases the porosity of castables[2].

Myhre investigated the effect of hydraulic alumina (Alphabond) on free flow value as demonstrated by Figure 2.22. It may be seen that with increased in the hydraulic alumina content, more water has to be added to obtain given flow[7].

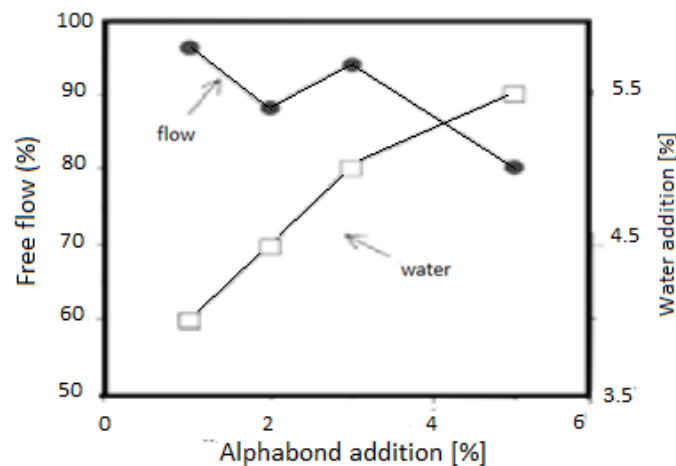


Figure 2.22 Free flow and increase in water content vs. % dosage of Alphabond[7].

Hydratable aluminas also have disadvantages. For examples, there is a high risk of explosive spalling at low temperatures, usually around 200-300°C due to the impervious structure[2]. Cardoso studied the drying behavior of hydratable alumina-bonded (HAB) refractory castables and compared them with the ultra low cement compositions[42].

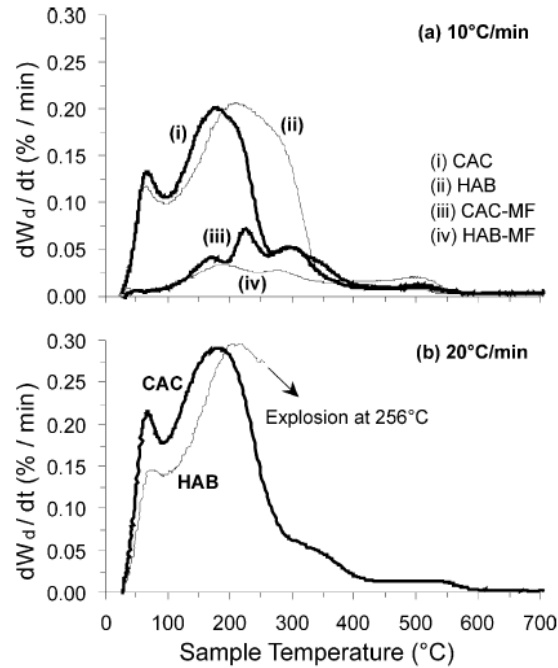


Figure 2.23 Drying behavior of CAC and HAB green castables subjected to continuous heating: (a) Rate of 10°C/min from room temperature up to 800°C. Curves (iii) and (iv) refer to moisture free (MF) samples. (b) A more aggressive heating rate (20°C/min) was applied to evaluate the explosive spalling occurrence[42].

Figure 2.23 shows that the intensity of the HAB evaporation peak is lower than that of the CAC drying profile indicating that a larger amount of free water remains available for vapor pressurization during the ebullition stage. The low permeability of the HAB samples is related to the formation of gel-like phases. These phases did not only restrict the evaporation process but also affected the second peak, causing it to shift to higher temperatures as the release of steam was adversely affected. Hence, greater pressure

gradients (i.e., higher temperatures) were required to expel the water vapor from the bulk of the solid at the same rate as from the CAC bodies[42].

In many cases, castables are selected as the preferred lining materials just because installation of bricks may be difficult or even impossible. Low and ultra-low cement castables are often the first technical choice, but whether these materials can be satisfactorily installed is not always immediately apparent. Among many factors that affect the quality of the installation, and of course the performance of the lining, are the following: inefficient mixing, excess water additions poorly placement, and inexperienced personnel. Flow of LCCs and ULCCs is usually promoted by internal or external vibration, since these materials are thixotropic in nature, but this solution alone is not always sufficient to assure the complete filling and good consolidation of all zones of the filling[1,2].

2.4.4. Self Flowable Castables

In order to overcome the installation problems associated with the vibration placement, a new class of high performance LCCs and ULCCs has been produced. These products were developed in the mid 1980s, characterized by excellent consistency and flow after mixing which allows the material to flow and degas without the application of external vibration[2,3,10-13]. These materials were named ‘self-flowing castables’ (SFCs), and were developed by modifying the rheology of the LCC and ULCC systems, by changing the shape and size distribution of the aggregates and by the use of deflocculants.

Otraj studied the effect of four different dispersing agents: sodium polyacrylate acid (Na-PAA), citric acid (CA), sodium tripolyphosphate (TPP) and sodium hexametaphosphate (HMP) on the flow behavior of ultra low-cement $\text{Al}_2\text{O}_3\text{-SiC-C}$ castables[31]. His results show that sodium polyacrylate has proved to be the most effective additive (Figure 2.24). The electrosteric mechanism of Na-PAA appears to promote the higher flowability in this system.

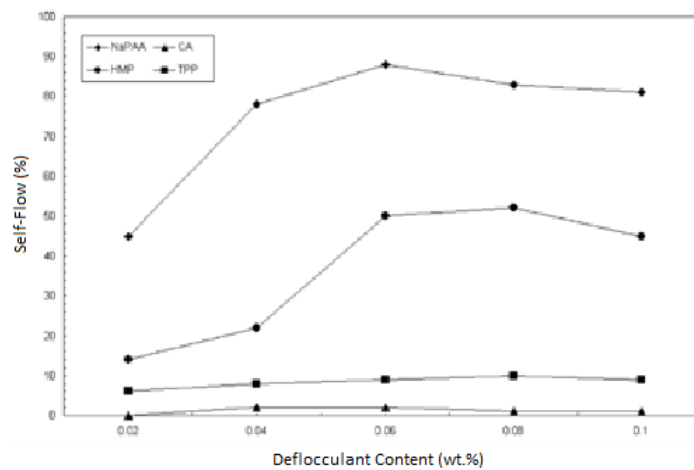


Figure 2.24 The effect of various deflocculants on the self flow of castables[31].

The basic idea was to reduce the points of contact between the aggregates, which affect the flow, by increasing the volume of the matrix, while keeping its density high. With water addition in the range 4.5-8%, depending on the product type, these castables self-flow under their own weight, easily filling intricate forms and shapes and, because of their cohesive consistency, those can be installed without segregation of the fine material or the fluid phase[2].

Early low cement, free flow castables had good flow characteristics but their strengths were significantly below those of vibrated LCCs. Other free flow castables with higher cement levels had an improved flow property. Modern self-levelling castables were

optimized to generate self-flow behavior at low water levels and utilize aggregates and cement levels similar to those of LCCs and ULCCs. The self-flow technology can be applied to a wide variety of compositions, ranging from fumed silica and bauxite based products to high alumina and silicon carbide based castables[1,2].

Myrhe studied the use of microsilica in refractory castables. Figure 2.25 shows an example of the effect of microsilica additions on flow of a tabular alumina based castable with 1.5% cement[9]

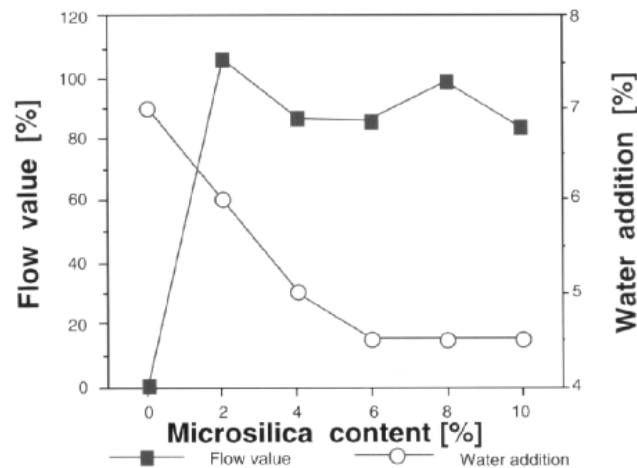


Figure 2.25 Flow value and water addition of tabular alumina based refractory castable as a function of microsilica content[9].

In this figure 2.25, when the microsilica content is increased from 2 to 4%, it allows to lower the water content by 1% while maintaining the flow. One percent water equals approximately the volume of 2% microsilica. However, at higher microsilica additions the water replacing effect is not pronounced. In turn, this demonstrates the microsilica effect as a microfiller[9].

However, despite of the significant improvements in the technology of castables, it should be noted that the physical properties of vibrated LCCs are generally superior to those of free flow castables. Self-flowing refractory castables also have their limitations such as: control of the setting time to allow the natural degas of the castable and yet prevent sedimentation or segregation[2]. Gierisch studied the aging behavior of alphasbond and calcium aluminate cement bonded castables[43]. For this purpose, he prepared 4 different refractory compositions: Two low cement castables (LCCs) based on different additives and ultra low cement castable (ULCC) and zero cement castable (ZCC). His results show that ULCC with dispersing aluminas M-ADS/W shows the higher aging resistance (Figure 2.26).

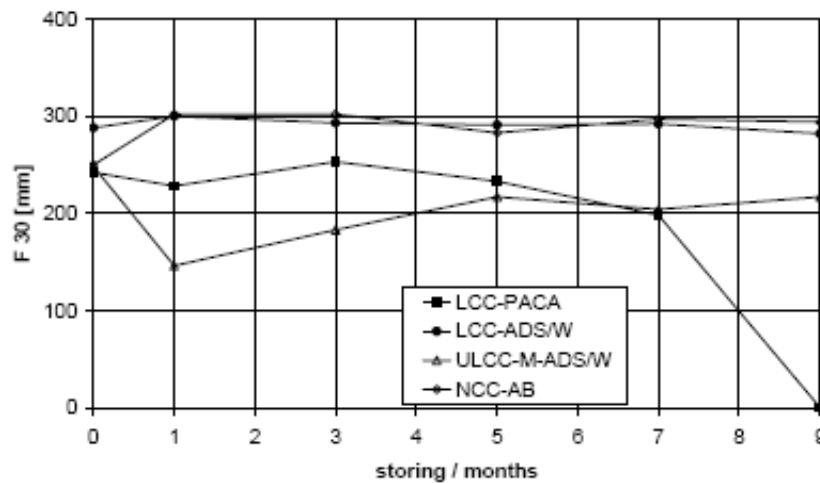


Figure 2.26. Impact of warehouse aging on flow at 30 minutes[43]

Other disadvantages are related to the strong influence of temperature on flow behavior and the setting time, with temperatures above 30°C being particularly harmful and detrimental to quality of installation differences in plant sites and applications. In turn, this requires different but controlled placement and demolding times and dilatant flow behavior, which complicates handling and dosing[2].

Myhre found that citric acid additions on free flow of the ultra low cement castables with 13 vol% water (4.10 wt%) at 35°C conventional castables had a very rapid flow decay at this temperature[6]. However, addition of 0.02 wt% citric acid helped in the free flow for a time sufficient for placement (see figure 2.27). Higher additive levels prolong the time until flow decay commences. These results show that flow is controlled by the particle size distribution, and the amount of retarder.

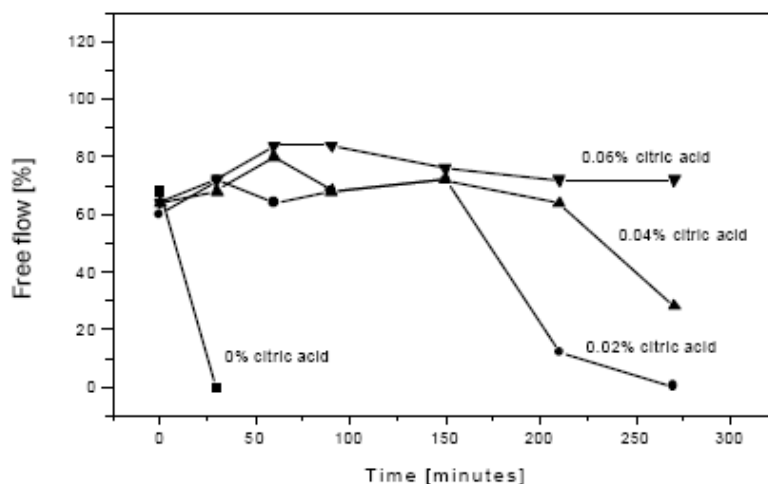


Figure 2.27 Free flow at 35°C as a function of time and citric acid addition. Ultra low cement castable composition with 13 vol% water (4.10 wt%)[6]

De Oliveira studied the setting behavior of ultra-low cement refractory castables in the presence of citrate and polymethacrylate salts[44]. Figure 2.28 shows the apparent viscosity values of castables with both additives as a function of time. These results indicate that there is a higher setting rate in the presence of sodium citrate when compared with that obtained in the case of the polymethacrylate salt. He concluded that a gel phase formed from compositions prepared with sodium citrate led to the reduction of the working time of refractories.

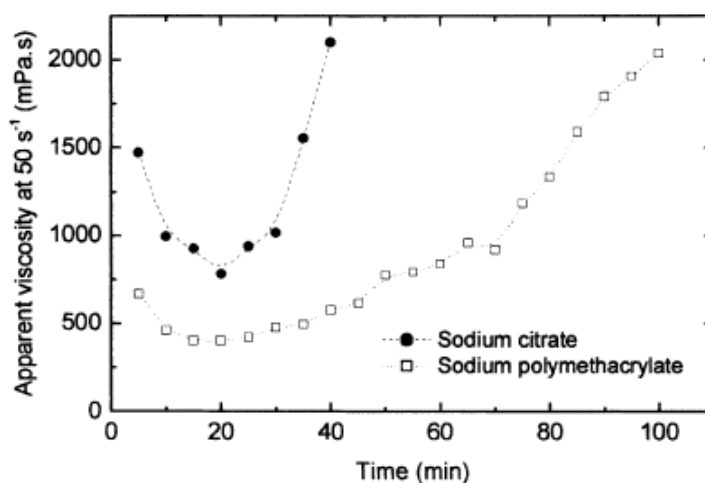


Figure 2.28 Apparent viscosity as a function of time of suspensions containing 5 wt% of sodium citrate or sodium polymethacrylate[44].

Finally, the water demand of self-leveling systems is considerably higher than that of vibration castables and similar to the thixotropic LCCs and ULCCs[2]. However, overwatering significantly affects the mechanical strength and corrosion resistance of these materials.

2.5 Fracture of Refractories

Fracture is always a critical problem for materials applications and one of the two most common modes of failure for the refractory linings of modern industrial processing vessels. The other is chemical attack, or corrosion by the material that the refractories are containing within the process vessel, often molten metals or glasses at very high temperatures[1].

Fracture failures are of several varieties, including simple mechanical overload that can arise from impact during the loading of the process vessel with scrap metal. Thermal stress fracture during cooling or heating, particularly the initial heat-up of a vessel or

during rapid thermal cycling between heats, is another type of failure. In the case of refractory concretes or castables, the situation of explosive fracture from moisture entrapment is also a major concern. These fractures may be catastrophic and result in the complete loss of the refractory lining. Sometimes thermal shock simply causes surface spalling and a significant reduction of the lifetime, or campaign, of the lining. However, fracture need not always be disastrous; it may just result in the development of a crack pattern in the process vessel lining. Those crack surfaces may be held together and closed by the vessel lining compressive stresses that develop from thermal expansion when the vessel is heated to operating temperatures[1].

Aksel studied the fracture behavior of magnesia and magnesia-spinel composites before and after thermal shock[45]. Figure 2.29 shows the fracture toughness values for MgO.

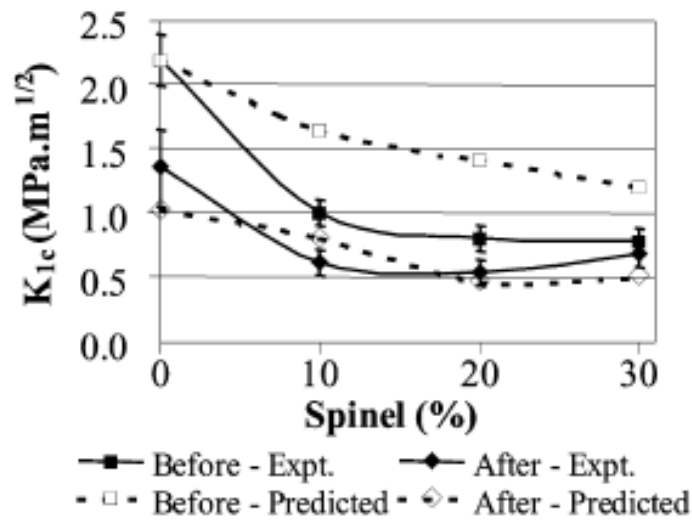


Figure 2.29 Fracture toughness as a function of spinel content before and after thermal shock[45]

The experimental composite toughness values are all below the one for pure MgO. The reason is that at room temperature, the fracture of MgO was mostly transgranular

(through the grains), and a large proportion of intergranular (along the grain boundaries) fracture was observed with increasing spinel content. The reason for the occurrence of intergranular fracture is linked to the presence of spinel particles at the grain boundaries. After thermal shock, fracture surfaces of MgO showed that the extension of a large amount of combined intergranular fracture appeared with some transgranular fracture above the critical quench temperature, $>600^{\circ}\text{C}$. Spinel composites had mostly intergranular fracture, after quenching from 800°C . Preexisting connected cracks appeared not to be able to propagate easily in the 20 and 30% spinel materials. For this reason, more energy was required to connect the cracks for propagation after thermal quenching. Therefore, the cracks propagate only a short distance and become arrested. The composite containing 30% spinel in general shows the greatest resistance to crack propagation, and to further thermal shock damage[45].

S. Ribeiro studied the influence of the microstructure on the maximum load and fracture energy of refractory castables[46]. Figure 2.30 shows results of the count of fractured aggregates at the surface. His results show that the number of fractured aggregates increases with the heat treatment temperature, indicating that the aggregates are strongly bonded in the structure of the matrix, and that the energy required to debond from the matrix would be higher than their resistance to fracture. This behavior is more pronounced for the higher test temperature at 1550°C , when sintering occurred[46].

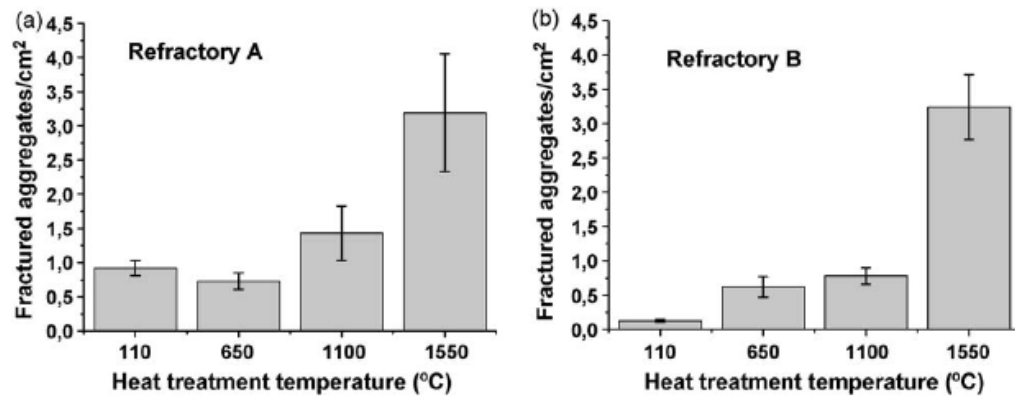


Figure 2.30 Fracture energy results for the samples of refractory castables heat treated at the temperatures[46]

In figure 2.31, there is a good indication of the fractured surface of the castables B, sintered at 1100°C for 12h, illustrating the fractured aggregates and debonded aggregates, and the place where the aggregates were debonded from the refractory castable matrix[46].

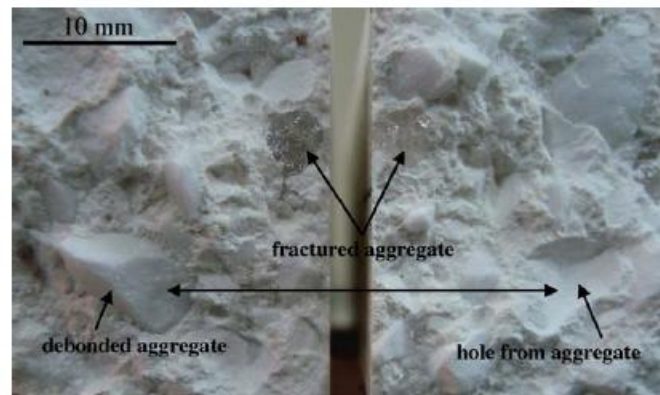


Figure 2.31 Photograph of the fractured sample showing: matrix (fine fraction), fractured and debonded aggregates (coarse fraction), and hole produced by pull out of the aggregate[46]

Basically, strength and fracture toughness are related through the aggregate sizing of refractories, which illustrates the importance of the microstructural aspects of the refractory aggregate to the strength. Their size and distribution in a refractory body of the

refractory aggregates play an important role in refractory fracture phenomena. This is due to the crucial role that aggregates assume in following the wake region of a crack. Thus, the aggregate distribution must be the focus of microstructural design for improved fracture characteristics when all other factors are equal in a refractory body[1].

2.5.1 Strengths of Refractories

Refractory strengths are generally reported in terms of the three-point bend strength or the flexural strength, frequently called the modulus of rupture (MOR)[47,48]. In the case of refractories, there exists a standard test for this simple strength measurement. It is based on the familiar formula[1]:

$$\sigma_f (MOR) = \frac{3PL}{2bd^2} \quad [2.4]$$

Where σ_f is the strength in three-point bending, L is the length of the test span, b is the specimen width, and d is the specimen height. The fracture load is P. It specifies the tensile stress at the bottom of the flexing bend test beam. In principle, equation 2.4 is strictly applicable only when the load-displacement curve is fully linear elastic to failure[1]. This equation can be converted to fracture mechanics terminology:

$$\sigma_f = K_{IC} Y C^{-1/2} \quad [2.5]$$

Where K_{IC} is the fracture toughness, Y is the geometric factor equal to $\pi^{-1/2}$ in the classical, and C is the critical flaw size. Flaw size are generally of the same size as the largest aggregates in the refractory since refractory mixes with larger top sizes aggregates have lower strengths than those containing just fine aggregates. It is an important point

for understanding the strength of refractories and the role of the aggregates in the refractory mix[1].

When refractories fail in a brittle elastic manner, where the load-displacement curve is clearly linear elastic to failure and both equations are satisfactory representations for the strength[1]. L.A. Diaz studied the room temperature mechanical properties of high alumina refractory castables with spinel, periclase and dolomite additions[49]. Figure 2.32 shows his bending strength results at room temperature with firing temperature. In this figure, refractory castables with spinel content 5, 10, 15 and 20 wt.% (8D type), and refractory castables with addition of magnesita (8DM type) and refractory castables with dolomite additions of 5, 10, 15 and 20 wt. % (PKDOL type).

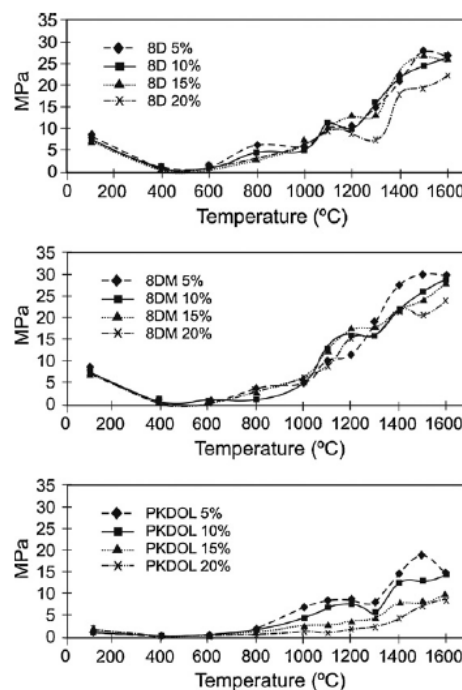


Figure 2.32 Flexural strength values of 8D, 8DM and PKDOL refractory castables[48].

Both the 8D and 8DM castables show similar flexural strength. Up to 400°C, the decrease in mechanical strength is due to the non-cohesive aggregate-matrix union. The increase in

flexural strength between 800 and 1000°C is related to crystallization of CA. The reaction of this phase with free alumina results in CA_2 which increases the flexural strength. At 1200°C a transitory liquid phase can be observed due to the dissolution of the CA phase after which another expansion occurs. Flexural strength is then observed to decrease. Above 1200°C, flexural strength of both 8D and 8DM compositions increase due to the sintering process. PKDOL compositions show lower values than both 8D-8DM sample because of the different composition location in the Al_2O_3 -MgO-CaO ternary diagram system[49].

G. Prokopski studied the fracture toughness of concretes at high temperature. He used three point bending tests to determine the fracture toughness[50]. His results show that fracture toughness values of samples increase with an increase in testing temperature. The reason is attributed to crack propagation along the contact surface between aggregate grains and the cement paste. Above 400°C, the cohesion of the grains with the cement paste caused grain cracks in numerous sites which resulted in the propagation of a fracture through the cement paste[50].

However, when refractories do not fail in a brittle linear elastic manner, such as when an extensive nonlinear region develops prior to fracture, then the use of these two equations is not the best practice for strength determinations[1]. Gogotsi investigated alternative methods of evaluating the fracture resistance of ceramics[51]. He indicated that the experimental results favor the view of the edge fracture (EF) method, which is not based on the linear elastic fracture mechanics principles. This method can be useful for checking the fracture resistance of ceramics and their resistance to crack propagation.

For the most part refractory linings, or systems, are not subject to severe load-bearing conditions: their function is primarily one of containment. Refractories do not have a major structural role in their applications. For these reasons, refractories do not need to be very strong or just strong enough to maintain their integrity. Typically, refractories have room temperature bend, or flexural strengths in the range of approximately 10-40 MPa (around 1500-6000 psi). It is important to realize that refractories are not very strong by any standards or comparisons[1].

S. Mukhopadhyaya investigated the effect of increasing the spinel content on the flexure strength of a low cement refractory castables[52]. Figure 2.33, shows the flexural strength of G in-situ spinel bonded castable as a function of the spinel content. Notice that spinel additions increases between 30-35 MPa the flexural strength which is better than for spinel free castables[52].

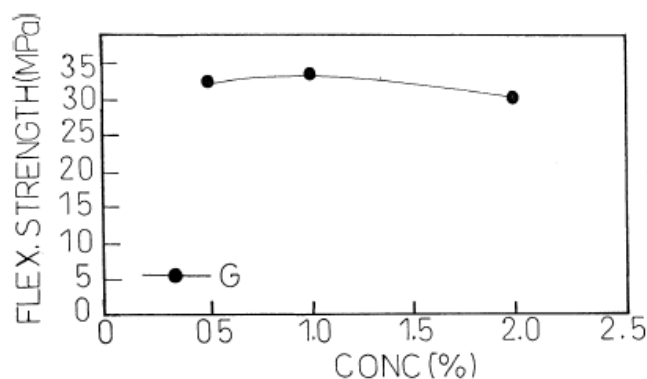


Figure 2.33 Plot of flexural strength (at 25°C) of fired (1500°C) in situ spinel bonded castable (G) with increasing concentration of spinel additive[52]

Fangboe Yea studied the high temperature mechanical properties of bauxite-based SiC-containing ultra low cement castables[53]. In figure 2.34, both samples have similar chemical composition except for the microsilica content (S8 and A8 samples contain 4.5

and 1.5% microsilica respectively). The results show that up to 600°C, there is only a slight increase in the MOR with increasing temperature. At temperatures between 800–1000°C, the MOR of specimens increases significantly, reaching a maximum at 800°C (sample A8) and 1000 °C (sample S8), then there is a decrease in strength at higher temperatures. It was concluded that both specimens contain more than two phases so the strength of these kinds of materials increases with temperature up to the inflexion point after which the strength decreases with temperature[53].

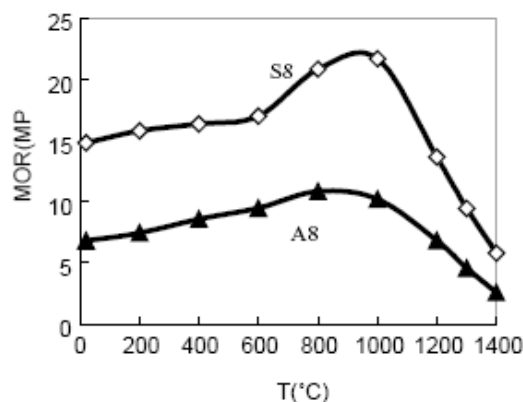


Figure 2.34 MOR– T curves for specimens A8 and S8[53]

Refractories are utilized at elevated temperatures, so there is an interest in improving their strength with increasing temperatures[1]. When the strength of refractories is measured by the three-point bend test and done so as a function of temperature, then the bend or flexural strength invariably exhibits a maximum that is associated with the softening of the silicate bonds. This strength maximum is usually not a very large one. It is usually observed between 600°C and 1400°C, depending on the particular refractory type, its silicate content, and the specific chemistry of that silicate. At elevated temperatures, above this strength maximum, the strength of the refractory rapidly decreases to only a few MPa and exhibits distinctly nonlinear load-displacement curves.

Although refractories are never very strong, they become even weaker at elevated temperatures, but they are noticeably less brittle as well. In addition, the loading rate dependence of strength at elevated temperatures becomes quite complicated. The coupling of the loading rate and temperature effects on strength have been previously addressed. It is not a simple interdependency, but one that varies considerably from one refractory system to another[1].

When attempting to understand the fundamentals that govern the strength of refractory systems, it is important to realize that although many refractories can be considered brittle materials at low temperatures ($<600^{\circ}\text{C}$), once the temperature of the strength maximum is exceeded, refractories no longer remain very brittle. The silicates soften and impart a significant degree of “plasticity.” Brittle fracture of refractories is not a major problem at elevated temperatures where a distinctly viscous, or plastic deformation, type of response occurs under most loading conditions. Furthermore, reported high temperature strength values of refractories should only be accepted with reservations and only applied to design situations with a considerable degree of caution. Most of those strengths are probably not properly measured[1].

In the 1970s and 1980s, researchers realized that the approach to understanding the fracture of refractories was to conduct measurements on individual or single cracks, instead of, or in addition to, the common bend strength measurements[1]. The K_{IC} -values were determined by the single-edge crack, or notched-beam bend specimen, where the normal three-point bend specimen was simply notched straight across at the half height

with a thin diamond blade. From this simple bend test of an artificially cracked (diamond saw notched) specimen, the fracture toughness is then calculated from the equation[54]

$$K_{IC} = \left[\frac{3P_{\max}L}{2bd^{3/2}} \right] \left[\frac{[a/d]^{3/2}}{[1-a/d]^{3/2}} \right] f \left\{ \frac{a}{d} \right\} \quad [2.6]$$

Basically, equation 2.6 is combination of eqs. (2.4) and (2.5) where the parameters have the same identities. The $f \{a/d\}$ polynomial is related to the ratio of the crack length to the specimen thickness and it is given by equation 2.7[53];

$$f \left(\frac{a}{d} \right) = \frac{1.99 - \left[\frac{a}{d} \right] \left[1 - \frac{a}{d} \right] \left[2.15 - 3.93 \left[\frac{a}{d} \right] + 2.7 \left[\frac{a}{d} \right]^2 \right]}{1 + 2 \left[\frac{a}{d} \right]} \quad [2.7]$$

Although most researchers have used a straight through sawed artificial crack of a depth of one half of the specimen thickness, it is recommended that the average precrack length shall be within the range: $0.35W \leq a \leq 0.60W$ [54].

G.B. Palmer studied the specimen size effect on fracture toughness for a low cement refractory pre-fired to 1200°C[55]. He concluded that fracture toughness was not constant with specimen size but once the specimen displays brittle characteristics then the fracture toughness becomes constant. Also once a critical size was reached, it was shown that the stress to failure for notched specimens was inversely proportional to the specimen size on a log-log scale[55].

The fracture toughness can be measured by this test at low temperatures where fractures are predominantly brittle and the load-displacement curve is essentially linearly elastic to

failure. Experimental tests show that the toughness of refractories usually are in the range of about 0.2 to 1.5 MPa.m^{1/2}, not very large toughness[1]. Refractory castables are at the lower portion of this range and fired bricks at the higher end. Refractories are not very strong since their intrinsic flaws are quite large, as evidenced by the readily visible large aggregates (flaws) in refractory bodies. That means the crack initiation resistance of refractories is not very large. Cracking and fracture may be expected to be of a concern for industrial refractories in many of their applications[1].

2.5.1.1 Indentation Toughness

Indentation technique is another method to measure the fracture toughness of the brittle materials. It is becoming increasingly attractive since it was first proposed by Palmqvist (1962) and developed by Evans et al. (1980) for the measurement of the microstructural toughness of ceramics. Indentation test is easy, quick to perform and requires only a minimum area of mirror finish quality polishing. It can be performed on a standard hardness tester, eliminating complex specimen geometries and experimental procedures. It potentially allows the characterization of both local and fracture properties[56].

Development of the crack during the indentation test depends on indentation load, material properties and type of indenter tip used in the test. In the literature, there are different types of indenter tips used. Although it was originally intended for application with sharp, geometrically self-similar indenters like the Vickers, Berkovich, it can be applied to a variety of axisymmetric indenter geometries including the sphere[56]. Figure 2.35 shows the schematic illustration of some of the indenter tips.

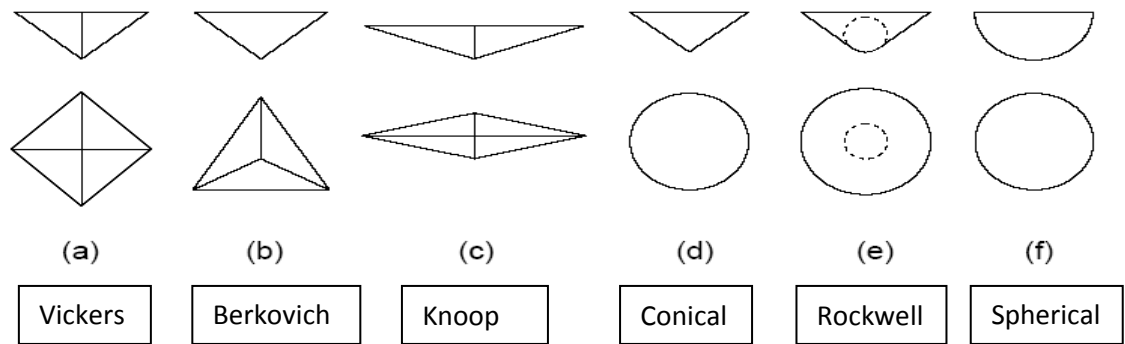


Figure 2.35 Schematic illustration of indenters tips.

The main idea in the indentation fracture toughness is the radial cracking (c) which occurs when brittle materials are indented by a sharp indenter. Then, the length of the radial crack (figure 2.36) is correlated with the fracture toughness (K_{IC}) and is used to calculate fracture toughness values[55]. Figure 2.36 shows a schematic diagram with indentation fracture.

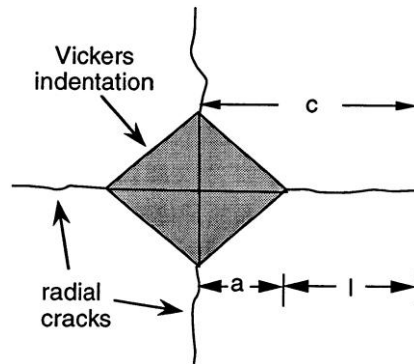


Figure 2.36 Schematic illustration of radial cracking at a Vickers indentation[57].

Initially, a Vickers indenter (four sided pyramid) was used for microhardness indentation test to correlate the length of the radial crack with the fracture toughness[57]. The well-known equation developed by Evans was then used to determine the fracture toughness[58].

$$K_{IC} = \delta \left(\frac{E}{H} \right) \frac{F}{c^{3/2}} \quad [2.8]$$

K_{IC} = Fracture toughness, lbf/in^{3/2}, (Mpa.m^{1/2})

E= Elastic modulus.

H= Hardness.

δ = An empirical constant which depends on the geometry of the indenter (0.016 for Vickers[59-61], 0.032 for berkovich[60-62] and 0.040 for cube-corner[56,57,60,61,69])

c=The length of the radial crack trace on the material surface after the indenter withdrawing.

In this method, a small indentation is made with a Berkovich indenter as the indentation load, P , and displacement, h , are continuously recorded during one complete cycle of loading and unloading. Figure 2.37 shows a typical set of load-displacement data[59]. The important parameters are peak load P_{max} , the displacement at peak load h_{max} , the final displacement after complete unloading h_f , and the initial unloading contact stiffness, $S=dP/dh$, i.e. the slope of the initial portion of the unloading curve. Once the contact area (A) is determined from the load displacement data, the hardness (H) is calculated by $H=P_{max}/A$.

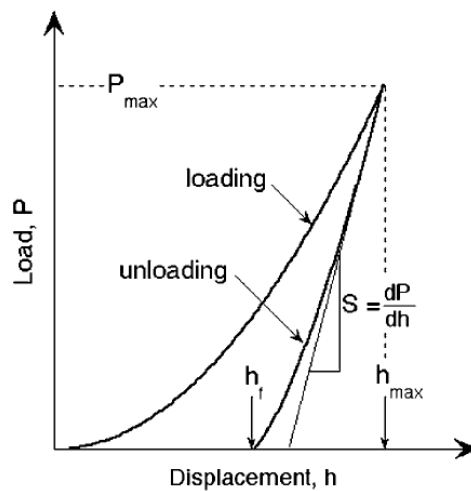


Figure 2.37 Typical load-displacement data[61].

In micro hardness tests, indentations are typically made at loads of 1000g or greater, and the crack lengths are of the order of 100 μ m or more. This method is generally effective method when the radial crack predominates or pyramidal indenters such as Berkovich (three-sided, having the same depth-projected area ratio as a Vickers indenter) and cube-corner (three sided, in the shape of the corner of a cube) are used. In order to measure the fracture toughness of thin films or small volumes using ultra low load indentation (nanoindentation), much smaller indentations are needed[57]. This leads to a significant problem called cracking threshold, below which indentation cracking does not occur. Cracking thresholds in most ceramic materials are about 250 mN or more for Vickers and Berkovich indenters, and the indentations produced at these loads are relatively large (several microns). It should be noted that the cracking threshold depends on the condition of the indenter tip, generally being higher for tips that have been blunted by wear[57].

The cube-corner can reduce the cracking thresholds 1-2 orders because of its much sharper angle when compared with Berkovich and Vickers. The centerline-to-face angle for cube corner is 34.3° whereas for the Berkovich indenter is 65.3°. Moreover, the cube-corner indenter displaces more than three times of volume of material as the Berkovich thus producing greater stresses and strains in the surrounding material. Significantly lower thresholds (less than 10 mN) can be achieved using cube corner-indenter. Larger stresses and strains promote propagation and indentation and reduce the cracking thresholds. Therefore, it is better to use the cube-corner indenter for determining the fracture toughness of brittle materials at a very small scale[57].

Mullins studied at measurement of the microstructural fracture toughness of cortical bone using indentation fracture[56]. He investigated three indenters; Berkovich, Vickers and cube corner as means of initiating cracks in applied loads between 0.05 and 3N. He found that cracks were only initiated with cube corner indenter. Figure 2.38 shows crack produced by using cube corner indenter.

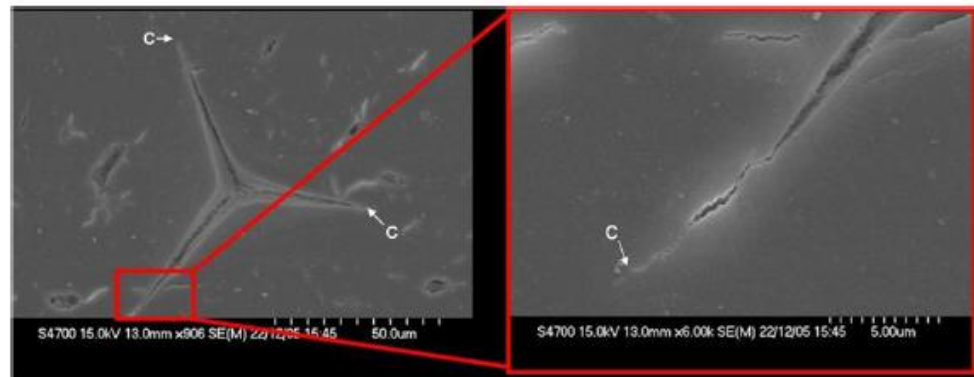


Figure 2.38 Typical cracks produced using a cube-corner indenter under a load of 2.6 N. A radial crack is highlighted. Crack tips are labelled c[56].

Pharr measured the mechanical properties by ultra-low load indentation. He reports that the fracture toughnesses computed from the cube-corner data are subject to errors of approximately $\pm 40\%$ [57,59]. Hardness and elastic modulus can be measured with accuracies of about $\pm 10\%$ in materials which do not exhibit pile-up. If there is pile up, it leads to overestimation of the hardness and modulus as much as 50%. Figure 2.39 shows the well defined radial cracks made by cube corner indenter.

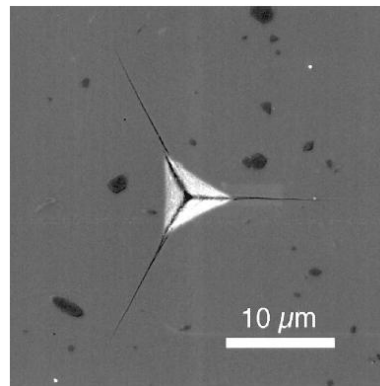


Figure 2.39 A small indentation in glass made with the cube-corner indenter showing well defined radial cracks[57].

Guo studied the nanoindentation characterization of deformation and failure of aluminum oxynitride[62]. He used a Berkovich indenter with different loads: 200mN, 300mN, 450mN and 700mN. Figures 2.40 (a-d) show the SEM micrographs of these indentations.

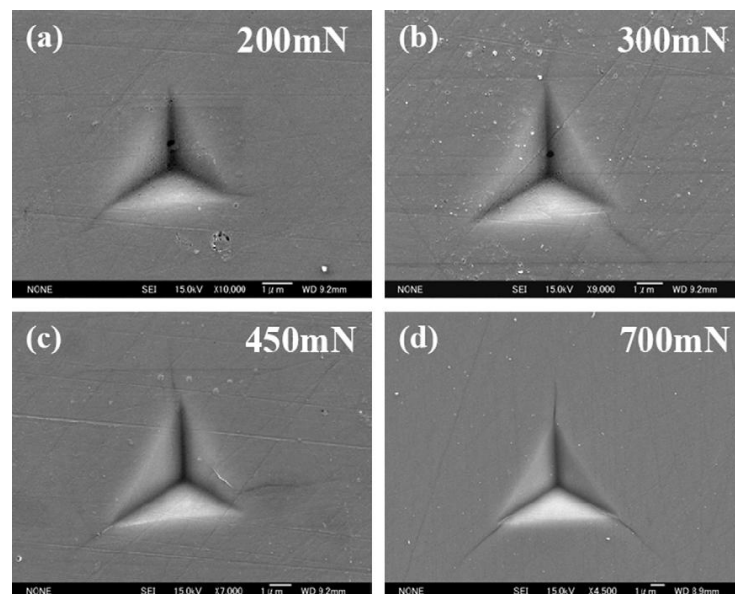


Figure 2.40(a–d) Representative SEM micrographs of nanoindentations made with various loading forces. Cracks at the corners of the indented impression can be observed[62].

In Figure 2.40, Guo showed that the micro-cracks become more distinct with increased crack lengths at all three corners of the Berkovich indentations at higher maximum loads.

Harding researched at cracking nanoindentation and its use in the measurement of

fracture toughness. He concluded that the cube corner indenter performs extremely well at low loads ($<500\text{mN}$) and indentation cracking thresholds can be reduced relative to the Vickers and Berkovich thresholds by more than an order of magnitude[62].

2.5.2 The Crack Process Zone for Refractories

Energy absorbing phenomena happens in the surrounding of the cracks of refractories. While the crack front moves ahead, a large amount of energy is consumed by the propagation phenomena[1]. These events happen in two different regions: the process zone in front of the advancing crack and the following wake region that trails the advancing crack front. Once a crack starts to propagate, it develops a steady-state frontal process zone, but the region behind the crack continues increasing. It is known that large cracks are more difficult to propagate than short cracks. This suggests the following wake region is more important to the crack growth resistance. Figure 2.41 schematically shows the total process zone about the crack, both in front of and following behind the advancing crack front[1].

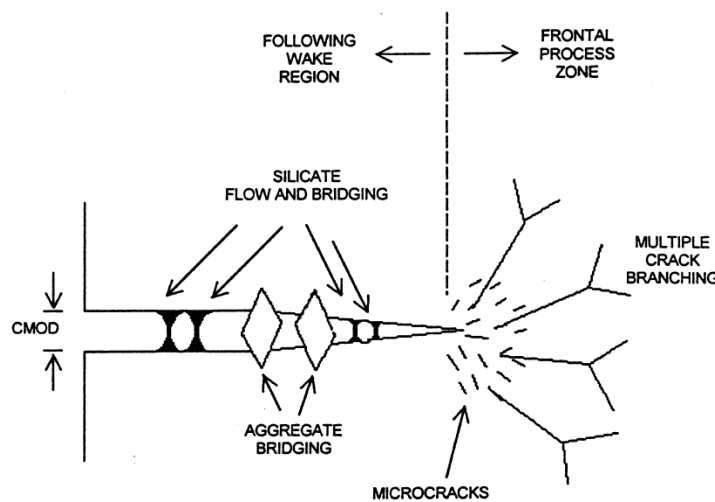


Figure 2.41 Schematic of the crack process zone for refractory materials[1].

Microcracking is occurring in the front of the crack, and there is usually considerable crack branching[1]. The other important region about an advancing crack front in refractories is the region behind the crack front. In brittle materials the crack opening displacement (COD) is not very large and neither is the crack mouth opening displacement (CMOD). Refractory microstructural elements such as the large aggregates are able to interact across the newly formed crack surfaces. It now appears that the phenomena occurring in the following wake region of the crack are the most important of all of the fracture, or cracking related phenomena in refractories. Refractory aggregate bridging and silicate ligament bonding are believed to be the most important toughness promoters in refractories[1].

Silicate ligament bridging of the crack surfaces is only of consequence to refractory fracture at elevated temperatures where the glassy silicates become viscous and can flow and form bonding ligaments between the newly created fracture surfaces. It is necessary that these silicate ligaments have some strength so as to be able to hold the forming crack faces together. They do, but only over a limited temperature range. Once the temperatures get too high, the viscosity of the silicates decreases and they are no longer strong enough to contribute to any significant toughness of the newly formed crack surfaces. This is probably the reason why there is a strength maximum as a function of temperature and a maximum in the work-of-fracture for silicate-containing refractory bodies. The bridging role of the aggregates behind the advancing crack front is monumental to the crack growth resistance of refractory materials but still their contributions to cracking is not completely understood. It is desirable that aggregates are

as large and as strong as possible to encourage crack by pass and consume energy during the bridging phenomena following the crack. An aggregate has to be at least as large as the crack opening displacement (the COD) or perhaps to the crack mouth opening displacement (the CMOD) to bridge the crack, if the aggregate is to bridge the crack at a large distance behind the advancing crack front[1].

The other important parameter is the geometrical aspect of the aggregates. Basically, angular aggregates have better mechanical interlocking effect than spherical ones. Also the use of fiber addition to castables shows that length and aspect ratio are important. Larger aspect ratios will give better crack growth resistance (see figure 2.42). However, mixing of this type geometrical fiber addition into refractory castable is difficult. Stronger and rough surfaces aggregates should be preferred than smooth ones. This subject will be discussed in more detail in the toughening mechanism section[23].

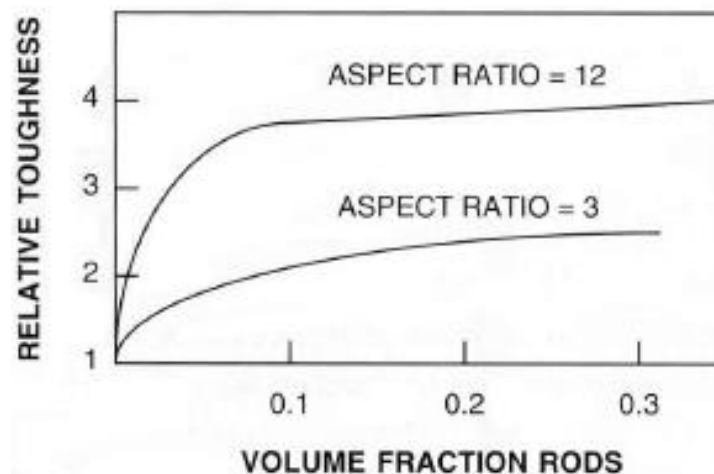


Figure 2.42 Toughening by rods is estimated to increase as the aspect ratio of the rods increases. The other important parameter is the chemistry of the bonding with silicates in the refractory[23].

Also, the highly acceptable phenomena taking place behind the advancing crack front, in the following wake region of a crack, are the most important effects to the crack growth resistance of refractories.

2.5.3 Toughening Mechanism

The fracture toughness of ceramics was first evaluated in the late 1960s[23]. Values of fracture toughness were typically below 5 MPa.m^{1/2} but some materials have now been developed with significantly higher fracture toughness values. (see Table 2.12)

Table 2.12 Some typical fracture toughness values for brittle materials[23]

Material	Mpa.m ^{1/2}
Silicate glasses	1
Barium titanate	1.5
Lead zirconium titanate	1.5
Alumina	2-6
Silicon carbide	2-4
Silicon nitride	3-7
Zirconia ceramics	5-35
Tungsten carbide/cobalt	10-20

Tremendous improvements have been made in the strength of ceramics in the past 40 years. These have lead to the detection of new toughening mechanisms and improved processing methods. Toughening mechanisms in ceramics can be broadly classified into two categories: one involves a process zone around the crack tip, the other is associated with crack bridging by reinforcements such as fibers, whiskers and particulates (Figure 2.42).

2.5.3.1 Transformation Toughening

Transformation toughening is one of the process zone toughening mechanism, considered to increase the intrinsic toughness. Among engineering ceramics, ZrO_2 exhibits an excellent combination of high flexural strength (1GPa) and good fracture toughness ($\sim 10 \text{ Mpa.m}^{1/2}$) but the mechanical properties of zirconia depend on phase structure and composition[24,63,64]. Zirconia has three stable crystal structures (cubic, tetragonal and monoclinic) as shown in Figure 2.43. The tetragonal (t) and monoclinic (m) polymorphs have distorted fluorite structures. On the other hand, cubic (c) zirconia has the ideal fluorite tetragonal. Undoped zirconia shows the following phase transformation: monoclinic is stable from room temperature to 1170°C , tetragonal between 1170°C and 2370°C and cubic above 2370°C all the way to 2750°C (melting point)[24,65-68]. Among these phases tetragonal zirconia exhibits high strength and toughness since the tetragonal to monoclinic transformation can be stress-induced or strain-induced under certain conditions[24,67-69].

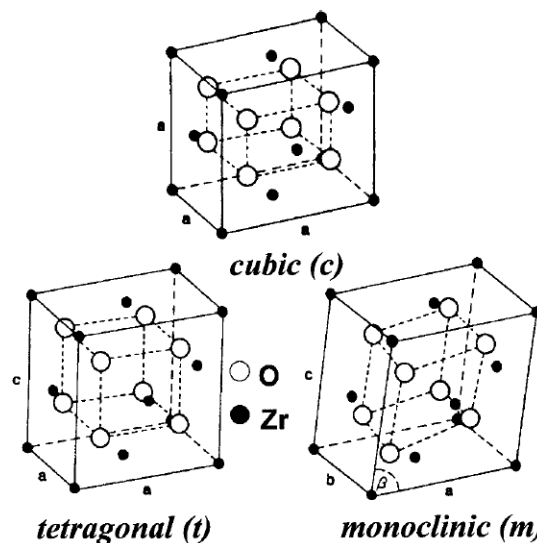


Figure 2.43 Crystal structures of most important zirconia polymorphs: cubic, tetragonal and monoclinic[24]

It has been found that the transformation of tetragonal (t-) ZrO_2 to monoclinic (m-) ZrO_2 is a reversible athermal martensitic transformation. The transformation ($\text{t-ZrO}_2 \rightarrow \text{m-ZrO}_2$) contains a large shear strain (14-15%) and a large volumetric strain (4-5%)[23,24]. The tetragonal phase is usually found at high temperatures and transformation from tetragonal to monoclinic starts at 950°C on cooling. However, the presence of a metastable tetragonal phase is key for the transformation toughening mechanism. In some cases, tetragonal zirconia can be retained at low temperatures by decreasing the grain size or adding a dopant such as Y_2O_3 , MgO , CaO or CeO_2 to suppress the tetragonal to monoclinic transformation upon cooling[64-67, 69-84].

The increase in the stability of t- ZrO_2 with decreasing grain size is considered to be due to increased effectiveness of the interface (relative to the volume fraction of the retained tetragonal phase) in constraining the shape changes accompanying the martensitic transformation. Another explanation is that the number of martensite units that can be accommodated decreases as the parent grain size decreases. Thus, fewer accommodating martensite colonies can form within finer t- ZrO_2 grains. The retention is primarily a result of the constraint on zirconia particles that is produced by the surrounding material, as shown schematically in Figure 2.44. If the transformation proceeds (a to b), a large amount of strain energy is produced in the surrounding material and this acts to 'oppose' the transformation. It has been shown that zirconia particles must be below a critical size for retention to occur[23].

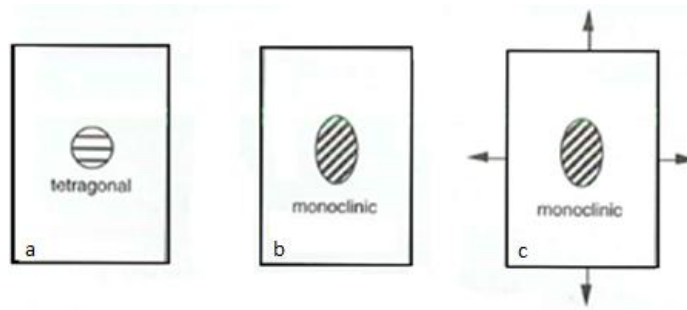


Figure 2.44 The transformation ZrO_2 from tetragonal to monoclinic[23]

When metastable retained $t\text{-ZrO}_2$ transforms to stable $m\text{-ZrO}_2$ phase, transformation toughening happens. The volume expansion (4-5%)[24,69,85] characteristic of the $t \rightarrow m$ transformation introduces a net compressive stress in the process zone around the crack tip. This reduces the local crack tip stress intensity and therefore the driving force for crack propagation, thus increasing the effective toughness of the material (Figure 2.45).

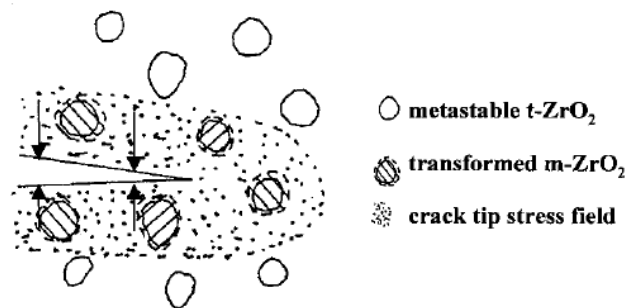


Figure 2.45 Stress induced phase transformation[24]

The mechanism of transformation toughening can be characterized by a change in the stress intensity factor.

$$\Delta K = K_{\text{tip}} - K \quad [2.9]$$

When the crack tip stress intensity factor K_{tip} is less than K ($\Delta K < 0$), crack tip shielding can take place. The retention of the maximum amount of $t\text{-ZrO}_2$ at the service temperature with optimum transformability is necessary for effective transformation toughening[24].

2.5.3.1.1 Thermodynamics of Transformation

Lang[69] proposed a thermodynamics approach based on the total energy involved in the $t \rightarrow m$ transformation and later modified by Becher[71]. The total free energy change per unit volume required for the constrained transformation can be expressed as

$$\begin{aligned}\Delta G_{t \rightarrow m} &= -\Delta F_{CH} + \Delta U_e + \Delta U_s - \Delta U_I \\ &= -\Delta F_{CH} + \Delta S - \Delta U_I\end{aligned}\tag{2.10}$$

ΔF_{CH} = is the chemical free energy, change associated with the $t \rightarrow m$ transformation

ΔU_e = is the strain free energy change

ΔU_s = is the change surface free energy

ΔU_I = is the interaction energy density (related to the application of external stress)

ΔS = is the sum of the changes in surface and strain free energy.

If the total free energy change can be increased, $t\text{-ZrO}_2$ is retained. This can take place by:

- Decreasing the chemical free energy change by alloying with a stabilizing dopant oxide (e.g. yttria, ceria, calcia, magnesia)
- Increasing the strain free energy change by dispersing the tetragonal phase in a constraining elastic matrix (e.g. alumina, cubic zirconia)
- Increasing the surface free energy change, e.g. by reducing the tetragonal grain size[24,69,71].

The effect of particle size on the transformation temperature (during cooling) is illustrated schematically in Figure 2.46. The ease of retention of the tetragonal phase is found to depend on the matrix surrounding the zirconia particles or precipitates[23].

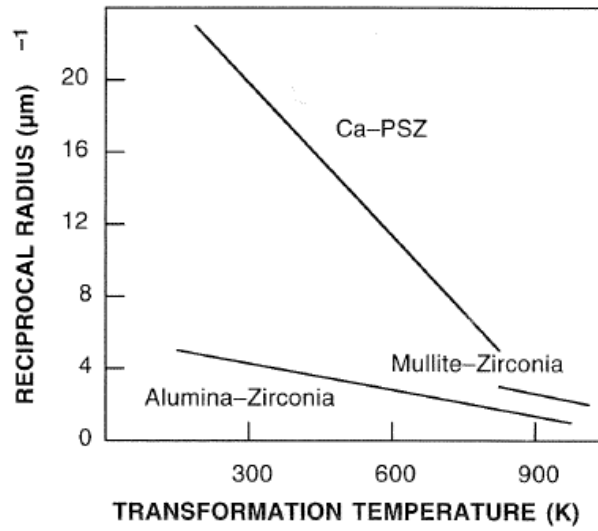


Figure 2.46 Critical particle size for the retention of tetragonal zirconia[23]

Based on the grain size effect, it is widely accepted that tetragonal zirconia can be stabilized at room temperature only if the size of the t-ZrO₂ grains in the sintered microstructure lies in the critical size range[24]. From equation 11, the condition for transformation of retained t-ZrO₂ with a grain size ($d < d_c$) in the crack tip stress field is given by

$$-\Delta U_I = 6 \sum \Delta S \left(\frac{1}{d} - \left(\frac{1}{d_c} \right) \right) \quad [2.11]$$

ΔS = the sum of the interfacial energy terms ($\Delta U_e + \Delta U_s$)

It was further proposed that there is a critical size range ($d_{cl} - d_{cu}$), regardless of the M_s temperature. Retained tetragonal particles can transform in the critical size range under the applied stress field. This means that a particle cannot transform below a lower bound, d_{cl} even if the interaction energy density exceeds the dilatational strain energy density characteristic of the transformation. On the other hand, particles above the upper bound,

d_{cu} spontaneously transform to m-ZrO₂ during cooling from the sintering temperature. This could lead to degradation of mechanical properties, in particular toughness[23,24].

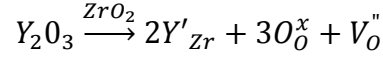
The critical size range for Ca-PSZ (partially stabilized zirconia) and Al₂O₃-ZrO₂ composites were found as 62-95 nm and 0.38-0.45 μ m, respectively[74]. Lange showed that the grain size must be <0.8 μ m to retain a fully tetragonal microstructure for 3Y-TZP[76].

2.5.3.1.2 Stabilization of Tetragonal Zirconia

The transformability/stability of the metastable tetragonal phase plays a critical role in transformation toughening[24,87]. Previous researchers suggested that stabilization is influenced by the size, charge and concentration of dopant cations[65,86]. The tetragonality, expressed as the c/a ratio, is significantly modified by dopant additions and hence influences the tetragonal phase stabilization. The displacement of the oxygen anions from their ideal positions in the fluorite structure affects stability by inducing a change in the electronic structure[24].

Yoshimura estimated the stability of the high temperature zirconia phases from both, thermodynamic and kinetic viewpoints[67]. From thermodynamic aspect, addition of sufficient stabilizing dopants can stabilize the tetragonal phase because its free energy decreases with the increasing dopant content. Another way to stabilize thermodynamically metastable phases (t-or c-ZrO₂) at room temperature is not to overcome the activation energy barrier for the transformation ΔG^* . In a published work, it was found that oxygen vacancies also play an important role in the stabilization of the

tetragonal phase[24]. Based on the Kroger-Vink notation, the defect reaction of zirconia doped yttria can be written as



Y'_{Zr} is an Y atom occupying a Zr lattice, and O_O^x is an oxygen atoms occupying a normal lattice site, and V_O'' shows a vacancy at an oxygen lattice site. Disorder in the ZrO_2 - Y_2O_3 system is increased with an increase in oxygen vacancy concentration. In turn, this leads to increasing stability of the tetragonal phase.

Shukla and Seal[68] researched at the mechanisms of t- ZrO_2 phase stabilization in nanocrystalline (<100nm), submicrometer (0.1-1 μ m) and coarse (>1 μ m) grained bulk ZrO_2 . Mainly, surface energy, strain energy, internal and external hydrostatic pressure, lattice defects were investigated in analyzing the t- ZrO_2 phase stability. Their results showed that the generation of excess oxygen ion vacancies is primarily responsible for room temperature stabilization of t- ZrO_2 in nanocrystalline ZrO_2 materials.

2.5.3.1.3 Yttria Content and Distribution

Previous works have shown that the nature and content of dopant cations largely influence the effectiveness of transformation toughening[24]. It was proposed that the chemical energy term in equation 2.10 is influenced by the yttria content in two different ways[24]. First, increasing yttria or solute content leads to a decrease in the undercooling effect (660°C for 2Y-TZP; 360°C for 3Y-TZP). The benefit of adding yttria is to enable the t- ZrO_2 phase to be retained at low temperatures for a given particle size so the fracture toughness of a transformation-toughened material is expected to increase with

decreasing test temperatures. Figure 2.47 shows the zirconia rich part of the $\text{ZrO}_2\text{-Y}_2\text{O}_3$ phase diagram.

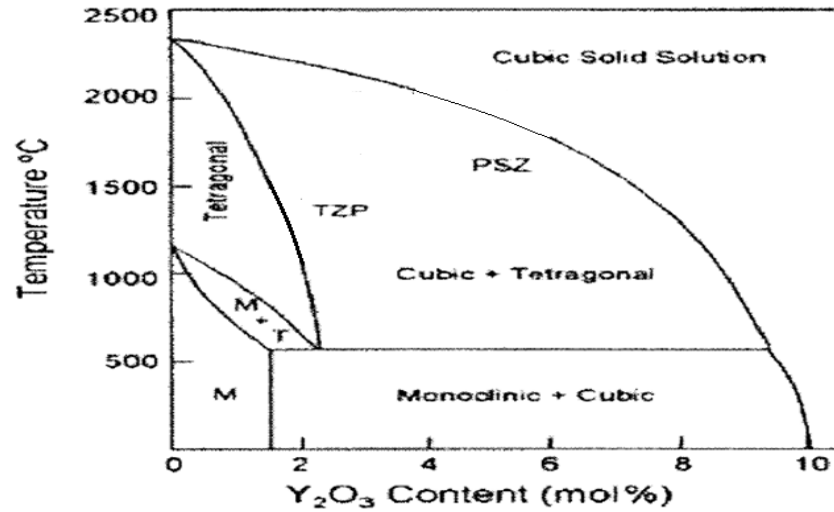


Figure 2.47 ZrO_2 rich portion of $\text{ZrO}_2\text{-Y}_2\text{O}_3$ phase diagram in the system[24]

At some critical temperature T_C , however, it may not be possible to retain the tetragonal phase and the fracture toughness will exhibit a maximum, as shown schematically in figure 2.48[23]. Second, reduced yttria content increases the residual stresses due to differences in the coefficients of thermal expansion (CTE).

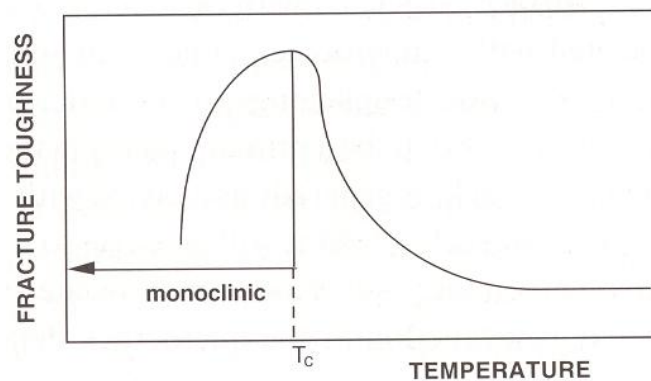


Figure 2.48 Influence of test temperature of fracture toughness. The transformation zone size increases with decreasing temperature, as the tetragonal particles become less stable. At some critical temperature, however, the transformation can become spontaneous[23].

Sakuma[79] used different yttria contents between 1 and 3 mol-% in order to optimize the fracture toughness of arc melted zirconia alloys. He achieved a maximum toughness of $15 \text{ MPa.m}^{1/2}$ in a sample with 1.8 mol-% Y_2O_3 . He also found that the toughness peak occurred at about 2 mol-% Y_2O_3 in Y-TZP ceramics processed by conventional sintering and arc melting. Masaki and Sinjo[80] produced zirconia ceramics with yttria levels of 1.5-5.0 mol-% by hot isostatic pressing. Their results showed that fracture toughness increased non-linearly with decreasing yttria content from 2.5 to 2.0 mol-% with a maximum of $20 \text{ MPa.m}^{1/2}$ for the 2Y-TZP.

Matsui[85] investigated the effect of equivalent grain size to critical yttria content X_{cr} over the mechanical behavior of Y-TZP ceramics. He showed that X_{cr} (critical yttria content) is between 4 and 5 wt-% for a TZP ceramic with $0.3 \mu\text{m}$ average grain size. The driving force for $t \rightarrow m$ transformation is relatively high during cooling from sintering for the tetragonal phase with an yttria content below X_{cr} . As a result, microcracking will happen due to the spontaneous thermally induced tetragonal transformation. Gao[88] found that the fracture toughness in a 2.1 mol-% Y-TZP with a grain size of $2 \mu\text{m}$ and 70% $t\text{-ZrO}_2$ was around $14 \text{ MPa.m}^{1/2}$. In another recent work, it was found by indentation toughness that toughness values of up to $14 \text{ MPa.m}^{1/2}$ can be achieved with 1.5Y-TZP nanoceramics at 1150°C . In general, decreasing the yttria content increases the toughness values.

The $t\text{-ZrO}_2$ transformation and fracture toughness of Y-TZP are also influenced by the yttria distribution. In order to achieve high toughness Y-TZPs, using powders with

widely different yttria contents are an important factor[24]. The presence of wide yttria and grain size distributions leads to high transformability and tougher Y-TZP ceramics.

Basu[64] achieved toughness of 9-10 MPa.m^{1/2} by mixing 8Y-ZrO₂ powders with undoped ZrO₂ to obtain an overall yttria content of 2 mol-%. The inhomogenous yttria distribution was shown by electron probe micro analysis (EPMA) measurements.

Vleugels and co-workers[89] also found high toughness in TZP ceramics with tetragonal microstructures and varying/heterogenous yttria distributions. The high driving force acting on relatively large tetragonal grains with low yttria contents favors the t→m transformation. Subsequently, increasing yttria containing grains transform in an autocatalytic manner characteristic of the martensitic transformation. The M_s (the start temperature for the martensitic transformation) is also another important parameter since the t→m transformation in zirconia is martensitic. Generally, increasing grain size increases to M_s which is independent of yttria content but also increases with decreasing yttria content. The accepted theory for ZrO₂-based ceramics predicts that the M_s for yttria doped (2 mol %) should be high due to the relatively large grain size. In co-precipitated Y-TZPs, the increased transformation toughening contribution from the increased mean grain size is reflected in an increased M_s temperature: 390°C (0.5µm) and 312°C (<0.5µm) for co-precipitated 2Y-TZP and a 2Y-TZP powder mixture-based, respectively. The higher the temperature difference M_s-T, the lower the transformation toughness. Apparently, M_s should be close to room temperature or to the service temperature in order to optimize the transformation-toughening contribution[24].

J.P. Singh[90] studied the effects of unstabilized ZrO_2 on the fracture surface energy and thermal-shock resistance of MgCr_2O_4 . Table 2.13 shows some of his experimental results as a function of the ZrO_2 content. Notice that both, flexural strength and fracture toughness reach a maximum value at 16.5% ZrO_2 content.

Table 2.13 Measured properties of MgCr_2O_4 - ZrO_2 composite specimens with different volume fractions of ZrO_2 inclusions[90]

ZrO_2 (vol.%)	Flexural Strength (MN/m^2)	Fracture Toughness ($\text{MN/m}^{3/2}$)
0	66 ± 7	1.36 ± 0.05
3.8	120 ± 15	1.49 ± 0.06
7.3	105 ± 15	1.54 ± 0.02
10.6	132 ± 11	1.79 ± 0.06
13.6	137 ± 31	2.26 ± 0.17
16.5	154 ± 25	2.84 ± 0.18
21.6	132 ± 31	2.42 ± 0.13

He suggested that these improvements are due to the absorption of energy from microcrack formation in the matrix, resulting from tensile stresses due to the mismatch in thermal expansion coefficients and/or elastic modulus between matrix and inclusions. In addition, a major cause of microcracking is the transformation of ZrO_2 from tetragonal to monoclinic phase, and the associated volume expansions. Also, the degree of improvement in the strength and fracture surface energy of MgCr_2O_4 with ZrO_2 inclusions was found to depend on the agglomerate particle size, size distribution, and volume fraction of ZrO_2 .

2.5.4 Fractography

Fractography is the study of fracture surfaces and it is an important tool in order to identify both, fracture processes, as well as failure origins[23]. Critical information can be obtained by observation of the fracture surfaces of brittle materials since they possess

very distinctive features. Cracks initially propagate on a plane perpendicular to the maximum normal stress. When the failure is unstable, the crack can subsequently branch as shown in figure 2.49. This leads to a large number of fragments from the failure process but careful examination of the branching morphology often allows to identify the region where failure started.

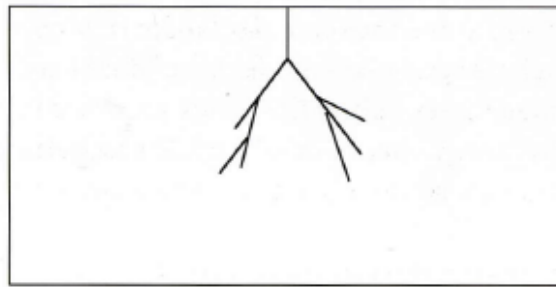


Figure 2.49 Crack initially propagates on a plane but, if failure is unstable, the crack will start branching[23].

An example of a failure origin in a brittle material is shown in Figure 2.50[23]. At the beginning, the region around the failure origin is rather smooth. In glasses, it is usually very reflective and is known as the mirror region. The same region can be seen in polycrystalline materials but the granular nature of the surface reduces the reflectivity. As the crack progresses, the fracture surface increases in roughness and a less reflective region (known as the mist region), is formed. This region is difficult to discern in polycrystalline materials. Finally, the surface becomes extremely rough as the crack branches and striations, known as hackle, are formed. The hackle marks usually ‘point back’ to the failure origin so they are useful for identification of the failure sources[23]. Failure ranges from being exclusively one type to a mixture of features. Intergranular failure is often associated with the presence of low-toughness grain boundaries or residual tensile stresses across these boundaries

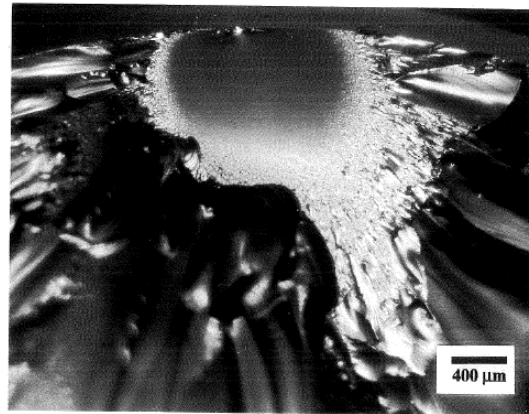


Figure 2.50 Fracture surfaces in brittle materials generally show a smooth region that surrounds the failure origin (mirror region) but the surface increases in roughness as the crack accelerates (mist region) until crack branching occurs. The branched region contain ‘ridges’ known as a hackle Fracture surfaces are often described as to whether a crack passes through grains (transgranular) or between grains (intergranular)[23].

In many cases, sub-critical crack growth is found to be intergranular but changing to transgranular once the crack becomes unstable[23]. It is important to determine the source of failure in order to develop approaches which prevent or remove the source. The failure origin is located at the center of the mirror region. Processing defects are common failure origins and several examples are shown in Figures 2.51-55[23]. Figure 2.51 show pores that act as failure origins.

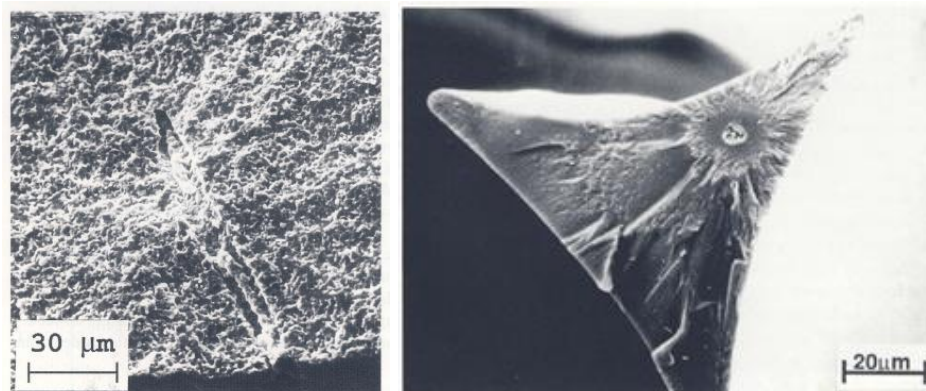


Figure 2.51 (a) Lenticular void that acted as a fracture origin in an alumina-zirconia composite (b) Spherical void that acted as a fracture origin in an open-cell vitreous carbon; scanning electron micrograph[23]

These pores are sometimes associated with organic impurities that are thermally pyrolyzed in the fabrication process, i.e., during sintering. In two phase materials, poor mixing of the two components can cause agglomerates to act as failure origins[23]. Two examples, showing failure from alumina agglomerates in alumina-zirconia are given in Figure 2.52

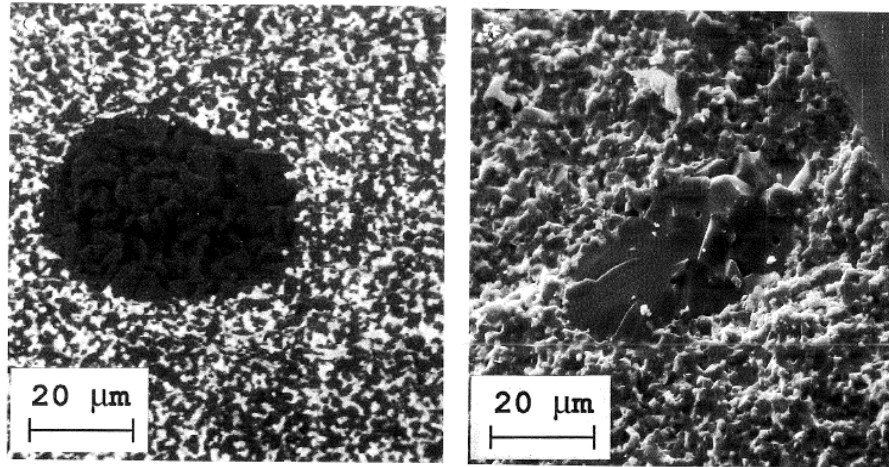


Figure 2.52 Scanning electron microscopes showing processing defects that act as fracture origins in alumina-zirconia composites: (a) porous alumina agglomerate; (b) large alumina grain[23]

An example of failure from a zirconia agglomerate is given in figure 2.53. Clearly, inclusions picked up as impurities during processing can also act as failure origins.

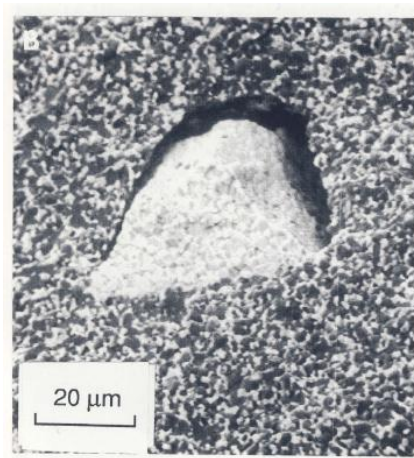


Figure 2.53 Failure origin in a zirconia-toughened alumina, caused by the presence of a zirconia aggregate in starting powder[23].

Contact-induced flaws are also common in brittle materials and usually result from machining damage, impact or simply surface contact figure 2.54(b) shows failure from a surface flaw in a sapphire (single-crystal alumina) fiber.

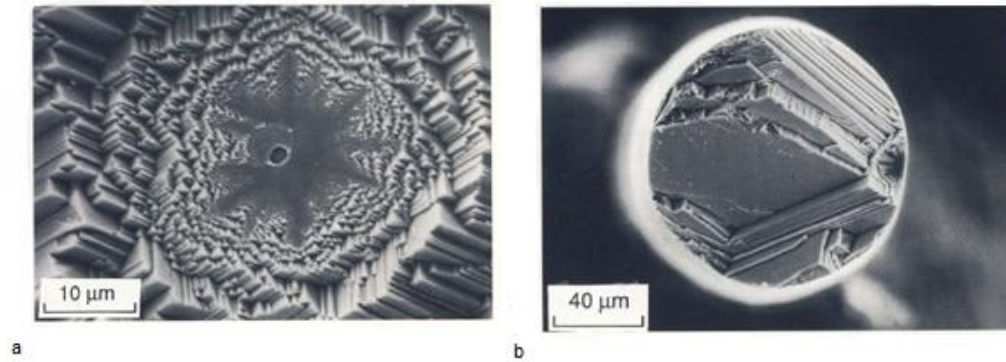


Figure 2.54 Scanning electron micrographs showing failure origins in single crystal alumina (sapphire) fibers : (a) internal pore: (b) surface flaw[23]

An example is given in figure 2.55, in which a silicon carbide inclusion in silicon nitride acts as a failure origin. In this case, it was concluded that the inclusions would be in residual tension at low temperatures and these stresses would aid in the crack initiation process.

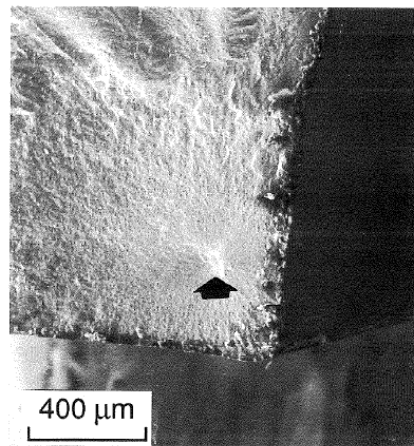


Figure 2.55 Silicon carbide inclusions that acted as fracture origin in silicon nitride; scanning electron micrograph.

CHAPTER 3- SCOPE and OBJECTIVES

3.1 Experimental Research

Among the goals of this research is to investigate the effect of cement and nano zirconia (ZrO_2)/ yttria stabilized zirconia (YSZ) on the properties of self-flow refractory castables. For this purpose, samples were heated up at different temperatures after designing formulations for improving the self-flow property. In order to find useful correlations between cement ratio, nano ZrO_2 /YSZ and the exhibited refractory physical properties, various refractory tests were carried out such as apparent porosity (AP), water absorption (WA), bulk density (BD), weight loss (WL), zeta potential (ZP), particle size distribution (PSD), cold crushing strength (CCS), modulus of rupture (MOR) and fracture toughness (K_{IC}). Moreover, the work included microstructural characterization by X-ray diffraction (XRD), scanning electron microscope (SEM), energy dispersive X-ray spectroscopy (EDX) and thermogravimetric analysis (TGA).

3.2 Experimental Refractory Compositions

In this research, the combination of different size Tabular Alumina, Microsilica, Calcined Alumina, Hydrated Alumina, different types of Cement and Nano-Zirconia and different additives such as; Darvan 811D, Citric Acid, M-ADS and M-ADW were used in the refractory mix.

3.2.1 Refractory Aggregate

- Tabular Alumina, Alcoa World Alumina, LLC, 99% Al_2O_3 fractions: (3-6mm) , (1-3mm), (0-1 mm) and (<45 micron)

3.2.2 Refractory Fillers and Modifiers

- Microsilica, 971U, Elkem, Norway
- Calcined Alumina, A-1000SG, Alcoa World Alumina, LLC,

3.2.3 Bonding Agents

- Calcium Aluminate Cement, Secar 71, Lafarge
- Calcium Aluminate Cement, CA-14M, Alcoa World Alumina, LLC
- Hydrated Alumina, Alphabond-300, Alcoa World Alumina, LL

3.2.4 Additives

- Polyacrylates, Darvan 811D, R.T. Vanderbilt Company, Inc
- Citric Acid
- Dispersing Aluminas M-ADS/M-ADW, Alcoa World Alumina, LLC,
- ZrO_2 and 8 mol Ytria stabilized ZrO_2 (99.9% purity, 30-60 nm), Advanced Materials US

The experimental compositions were designed in order to obtain outstanding self flow properties at low water levels. All castables were made based on tabular alumina refractory aggregates. Accordingly, the ceramic components of the binding system for low cement castables containing 5wt% cement (SFC-5) are calcined alumina, microsilica and calcium aluminate cement (CAC). The ceramic components of the binding system of

ultra low cement castables formulations containing 3wt% (SFC-3) and 1wt% (SFC-1) cements are calcined alumina, microsilica, hydrated alumina and calcium aluminate cement (CAC). Table 3.14 shows the compositions of the investigated refractory castables.

Table 3.14 Experimental composition of SFCs.

	%		
	SFC-5	SFC-3	SFC-1
Tabular Alumina			
3-6 mm	17	17	17
1-3 mm	26	26	26
0-1 mm	27	27	27
<45 micron	13	14	14
Calcium Aluminate Cement	5	3	1
Hydratable Alumina (Alphabond 300)	-	1	3
Calcined Alumina (A 1000SG)	7	7	7
Microsilica (971U)	5	5	5
Accelerater (M-ADS)	-	0.9	0.9
Retarder M-ADW)	-	0.1	0.1
Darvan-811D	0.05	-	-
Citric Acid (Retarder)	0.05	-	-
Water	5.5	5.5	5.5

3.3 Preparation of Nanoparticles

Different ratios of ZrO_2/YSZ nanoparticles (0.01, 0.1, 1, 3 and 5% of binder system) were mixed with 0.9% M-ADS and 0.05% Darvan 811D additives with total mixing water in a Branson 3510 ultrasound mixer for 20 minutes.

3.4 Self-Flowing Test

All self flow measurements followed the ASTM-C71. Measurement of the flow value was achieved by pouring the castable suspension into the truncated flow cone as described in the ASTM standard C230 (Figure 3.56). After filling the castable into the cone, the cone was removed and the castable allowed to spread under the effect of gravity. When the spreading stops approximately after two minutes, the percentage increase in the diameter of the spread cone is measured (Figure 3.57) and it is known as the free flow value (equation 3.1).

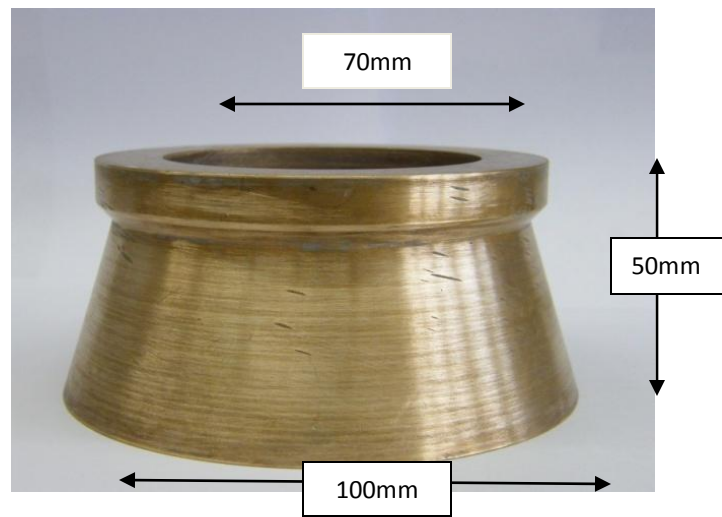


Figure 3.56 The truncated flow cone described by ASTM C230.

$$\text{Self Flow} = \frac{\text{Average final diameter} - \text{Initial diameter}}{\text{Initial Diameter}} \times 100$$

The refractory compositions were prepared using the Andreassen Mathematical Model where the q-value (Andreassen distribution coefficient) is determined using the EMMA

Elkem Material Mix Analyzer-Software. The experimental work shows that 5.5 % water is sufficient to obtain a self-flow well dispersed castable system. In addition, the basic flow properties of the refractory castables were investigated as a function of the amount of cement and nano-ZrO₂/YSZ.



Figure 3.57 The measurement of self flow value of castable after pouring from truncated cone.

3.5 Determination of Particle Size Distribution, Zeta Potential and pH of Nanoparticles

A dynamic light scattering equipment (DLS) (Brookhaven Instrument) was used in order to measure the particle size distribution (PSD), zeta potential (ZP) and PH of nano ZrO₂/YSZ particles. The DLS was ready to measure PSD after the prepared solutions containing nano-ZrO₂/YSZ nanoparticles were diluted with de-ionized water. Each measurement consisted of 5 runs, each of 60 seconds duration over the full range of capacity of the instrument and the average results were used. In order to determine the zeta potential (ZP), the prepared solutions, were diluted in 1μm KCL and phase analysis

light scattering (PALS) was used for determinations of the velocity of the moving particles through their effect on scattering laser light. Also, PH measurements were necessary since the zeta potential (ZP) is a meaningless number without considering the PH. Thus, the prepared solutions were connected to the DLS in order to measure the PH of the solutions.

3.6 Bulk Density, Apparent Porosity, Water Absorption and Density

The bulk density (BD), apparent porosity (AP) and water absorption (WA) were measured by using the Archimedian evacuation method according to the ASTM C 20-97 standard. For this purpose, the samples were dried at 110°C for 24 hours to a constant mass and weighted in air. The samples were then placed in water and boiled for 2 hours. After boiling, the specimens were kept immersed in water for 24 hours, and re-weighed while suspended in the liquid. Finally, the soaked samples were re-weighted in air. Eqs. 3.2, 3.3, 3.4 and 3.5 were used for calculations of the bulk density, apparent density, water density and density, respectively.

$$\text{Bulk density} = \frac{\text{weight in air}}{\text{soaked weight} - \text{suspended weight}} \times \text{liquid density}$$

$$\text{Apparent porosity} = \frac{\text{soaked weight} - \text{mass in air}}{\text{soaked weight} - \text{suspended weight}} \times 100$$

$$\text{Water absorption} = \frac{\text{soaked weight} - \text{weight in air}}{\text{weight in air}}$$

$$\text{Bulk Density} = \frac{\text{weight in air}}{\text{Exterior Volume (soaked weight} - \text{suspended weight)}}$$

All of these properties are primary properties of the fired refractory castables and they have an intimate influence over properties such as the refractory thermal conductivity and thermal shock resistance. Low porosity materials have low water absorption properties, higher density and better resistance to chemical attack when compared with high porosity materials.

3.7 Microstructural Analysis

Experimental castable refractories including the binding systems were analyzed after various thermal treatments in order to identify their exhibited microstructural features . The binding systems were investigated using X-ray diffraction (XRD) in order to determine any phase formation after exposure to 110°C for 24 hours and 1000°C, 1300°C and 1500°C for 3 hours. Fracture surfaces and binding systems of samples were observed in an SEM with an EDX detector. Both, refractory samples and binding systems were coated with Au-Pd and for SEM determinations at 15kv accelerating voltage. In addition, in order to determine thermal stability of the specimens, thermogravimetric analysis were made in a SDT 2960, TGA equipment. Weight changes in the samples were measured as a function time and temperature. The measurements were carried out on milligram size samples with a heat rate of 20°C/min all the way to 1000°C in a 100ml/min argon flow.

3.8 Cold Crushing Strength (CCS), Modulus of Rupture (MOR), Fracture Toughness (K_{IC}) and Indentation Toughness of Castables

After drying and firing of the castable compositions, mechanical properties were determined by measuring cold compressive strength (CCS) using an universal testing instrument INSTRON and the Modulus of Rupture and Fracture Toughness using SATEC universal testing machine. The CCS measures the refractory strength of the grains and of the bonding system. In order to measure the CCS, samples were cast on cube-type molds (50x50x50mm). Equation 3.6 is used for calculations of the CCS.

$$S = \frac{W}{A}$$

S= cold crushing strength, lbf/in², (MPa)

W= total maximum load indicated by the testing machine lbf, (N) and

A= average of the areas of the top and bottom of the specimen perpendicular to the line of application of the load, in², (mm²).

The MOR is indicative of the strength of the bonding system for the refractory product. Determinations by three point bending tests were made on 160x40x40 mm bars at a 100 mm span using a crosshead speed of 0.05 in/min. These samples were used to measure the strength of the bond including the aggregates. The test configuration in Figure 3.58 shows the specimen loading location between two support bearings and the load application at the center of the bar by a loading arm.

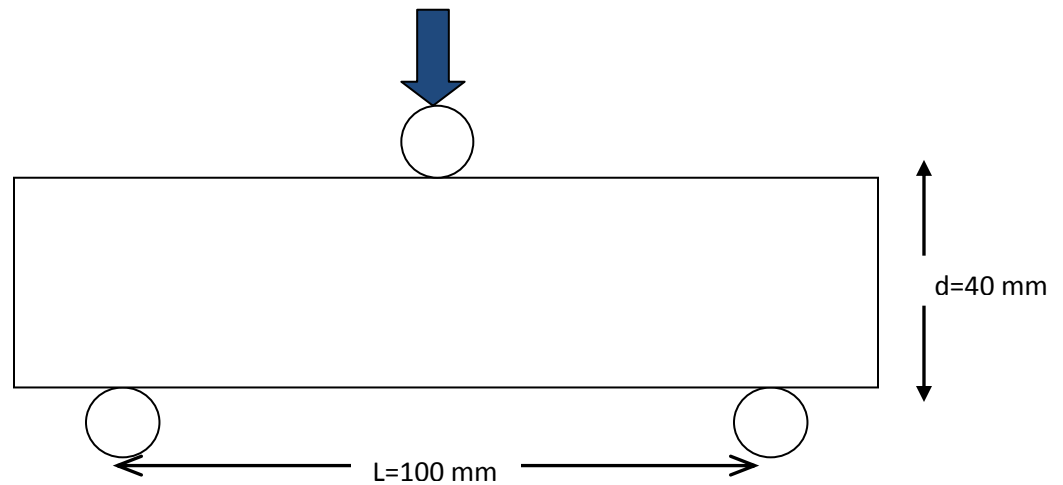


Figure 3.58 Three point bending test.

A second MOR experiment was implemented to measure the strength of the binder alone. In this case, less than 150 micron powders were used to prepare the samples. The sample dimensions were 25x10x10 mm at a crosshead speed of 0.2mm/min. Equation 2.4 gives the standard formula for the calculation of MOR in three point flexure

$$MOR = \frac{3PL}{2bd^2}$$

MOR=modulus of rupture, lbf/in² or (MPa)

P=maximum applied at rupture, lbf or (N)

L=span between supports, in. (mm),

b=breadth or width of specimens, in. (mm), and

d=depth of specimen, in. (mm)

Toughness values were determined using two different methods. In the first method, fracture toughness values were determined using 160x40x40mm specimens with a sharp

notch at a crosshead speed of 0.5 mm/min. The sharp notch of approximately 14 mm and 0.35 mm of depth, was cut in the middle of the specimens using diamond saw (Figure 3.59). In addition, 25x10x10mm specimens were prepared in order to determine the fracture toughness of the binding system. A crosshead speed of 0.1 mm/min was used for fracture toughness testing and the K_{Ic} values determined using Eq. 2.6.

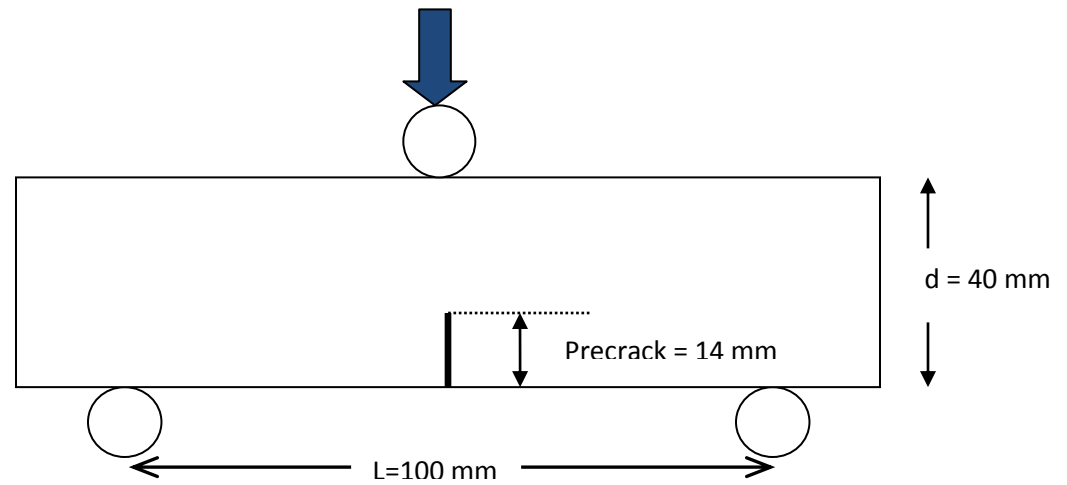


Figure 3.59 Schematic illustration of fracture toughness test.

$$K_{IC} = \left[\frac{3P_{\max} L}{2bd^{3/2}} \right] \left[\frac{[a/d]^{1/2}}{[1-a/d]^{3/2}} \right] f\left\{ \frac{a}{d} \right\}$$

K_{IC} = Fracture toughness, lbf/in^{3/2}, (Mpa.m^{1/2})

a = Crack length, in, (mm)

$f\{a/d\}$ = function of the ratio of the crack length to the specimen thickness, is given by Eq. 2.7

$$f\left(\frac{a}{d}\right) = \frac{1.99 - \left[\frac{a}{d}\right] \left[1 - \frac{a}{d}\right] \left[2.15 - 3.93\left[\frac{a}{d}\right] + 2.7\left[\frac{a}{d}\right]^2\right]}{1 + 2\left[\frac{a}{d}\right]}$$

In addition to fracture toughness, an indentation toughness method was used. Prior to indentation testing, the surfaces of the samples were mechanically polished with 400, 600, 800 and 1200 SiC grit paper and then polished with a water based diamond solution of 3 and 1 μm in size. Final polishing was completed with using 0.05 μm alumina suspension. Elastic modulus and hardness values were determined with using a Berkovich tip in an Agilent G200 nano-indenter machine. All nano-indentation tests were performed at an allowable drift of 0.33 and an applied force of 50 gf. A standard vickers HV hardness indenter (Buehler Micromet II micro hardness tester) was also used to measure the hardness values and for crack initiation. The applied force was 500gf and 1kgf with a dwell time of 15 second. Crack lengths were measured in the microhardness tester with an optical instrument as shown in Figure 3.60(a-b) .

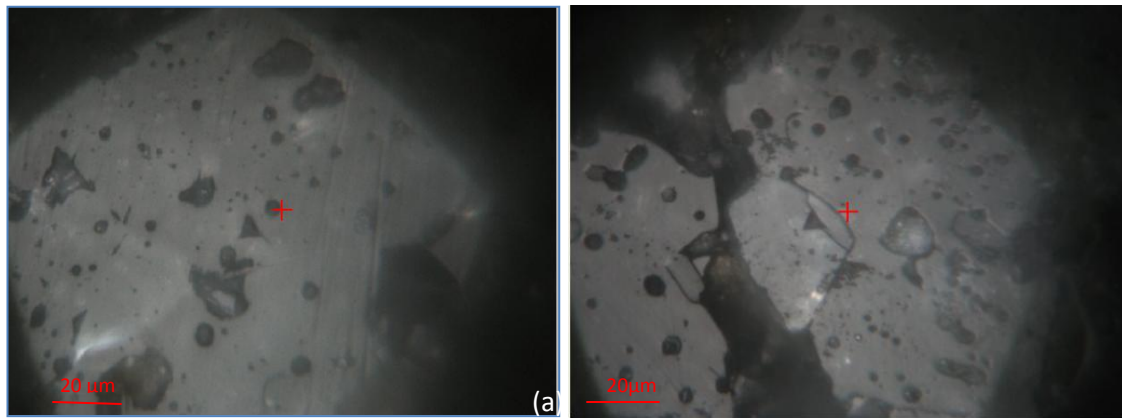


Figure 3.60 (a-b) Cracks created by berkovich indenter in nanoindentation test

Equation 2.8 was used to calculate the indentation toughness of samples using the indentation fracture method.

$$K_{IC} = \delta \left(\frac{E}{H} \right) \frac{F}{c^{3/2}}$$

K_{IC} = Fracture toughness, lbf/in^{3/2}, (Mpa.m^{1/2})

E= Elastic modulus

H= Hardness

δ = Empirical constant which depends on the geometry of the indenter (0.016 for Vickers, 0.032 for Berkovich)

c= Length of the radial crack trace on the material surface after the indenter withdraws

3.9 Rheology and Flow Measurements of Castable Refractories

The study of rheology of self flowing low and ultra low castables was focused on following subjects:

- Effect of different amounts of cement and ZrO₂/YSZ nanoparticles on self flow behavior;
- Determination of optimum particle size distribution (PSD) of refractory castables;
- Influence of additives on Zeta Potential (ZP), pH and particle size distribution (PSD) of ZrO₂/YSZ nanoparticles;
- Effect of ultrasonification and additives on distribution of ZrO₂/YSZ nanoparticles in the water based solution;

The goal of this research was to establish for a direct correlation between the flow properties and cement amount and additives. In addition, maintain the homogenous distribution of ZrO₂/YSZ nanoparticles in the system and provide tool for optimization and design of self flowing LCCs and ULLCs and improve the MOR and fracture toughness of castables.

CHAPTER 4 - EXPERIMENTAL RESULTS and DISCUSSION

4.1 Determination of Andreassen Distribution Coefficient

The flow properties of the castables were studied using the Andreassen distribution model . Figure 4.61 shows the Andreassen distribution coefficient (q value) of the experimental castables as compared with the reference data (q=0.25).

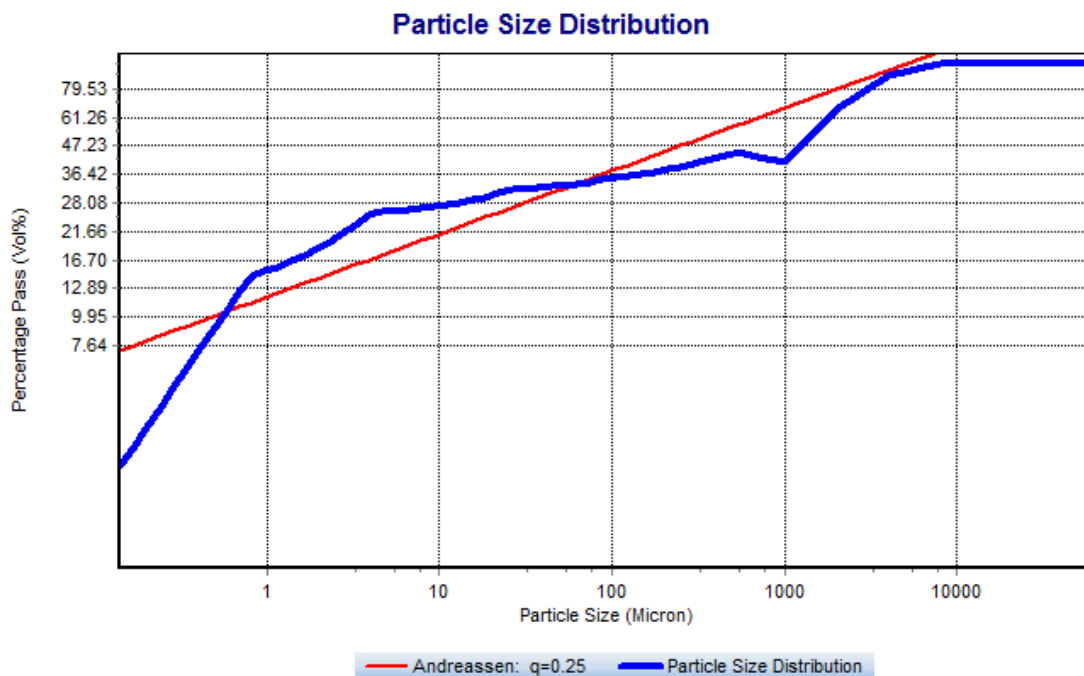


Figure 4.61 Andreassen distribution coefficient (q value) for the experimental castables

As mentioned before in chapter I, in order to get dense castables the q value should be ≤ 0.37 whereas a q value above 0.37 results in castables with voids. For vibratable castables, the q value should be ≤ 0.30 . In order to get good self flow behavior, the q value should be ≤ 0.25 . As seen in the above figure 4.59, the q value of SFCs fits approximately 0.25, indicating that it is in the proper range for q values of SFCs. Notice

that lower q values means smaller particle sizes and increasingly dense castables. In contrast, high q values means large particle sizes and less dense castables. It is important to know that small particles do the main contribution to flowability whereas large particles do not play a good role in flowability. In addition, it is necessary to use proper additives to get good self flow behavior at lower water contents since these additives increase flowability with electrically charged particles and thus decrease the water content. Notice that the water content can help the flowability but it evaporates at elevated temperatures, resulting in porosity in the castable system. As a conclusion, proper selection of the components in the castable system, using additives and by determining the Andreassen distribution coefficient (q value) are crucial to get good self flow properties.

4.2 X-Ray Diffraction (XRD) Analysis of SFCs

Figure 4.62 shows the X-ray diffraction patterns (XRD) of the refractory castables dried at 110°C for 24h. As expected from the X-ray results, strong diffraction peaks corresponding to the corundum phase (α -Al₂O₃), with a rhombohedral structure and lattice parameters $a=b=0.4758$ and $c=1.2991$) was found in the experimental castables.

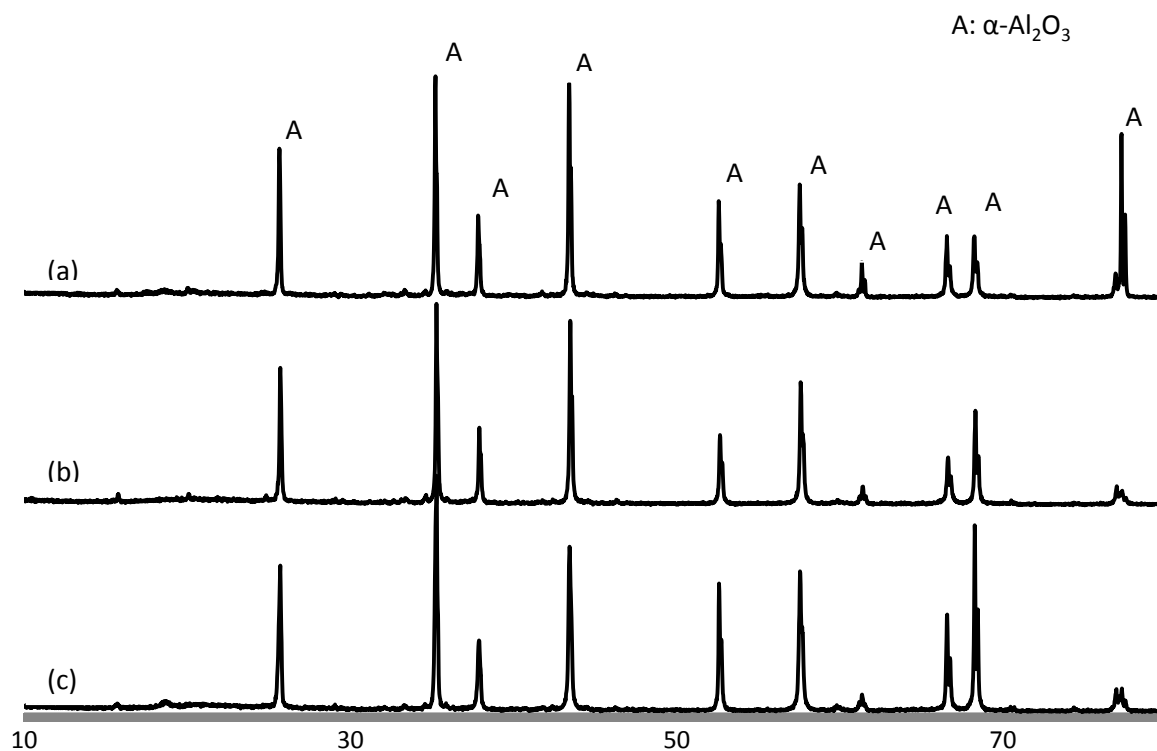


Figure 4.62 XRD patterns for (a) SFC-5, (b) SFC-3 and (c) SFC-1 dried at 110°C for 24h.

After firing at 1000°C for 3h, XRD results revealed that there were no new phases detected in both, SFC-3 and SFC-1 samples besides corundum as shown in figure 4.61. In contrast, the formation of anorthite with a chemical formula $\text{CaAl}_2\text{Si}_2\text{O}_8$, (a triclinic structure with lattice parameters $a=0.8165\text{nm}$, $b=1.2872$, and $c=1.41827\text{nm}$) was observed in SFC-5 samples, containing 5% cement as seen in Figure 4.63. In Turn, this suggests that at increasing cement contents, there is an early development of ceramic bonding when compared with hydratable alumina (e g no new phases detected in SFC-3 and SFC-1 samples).

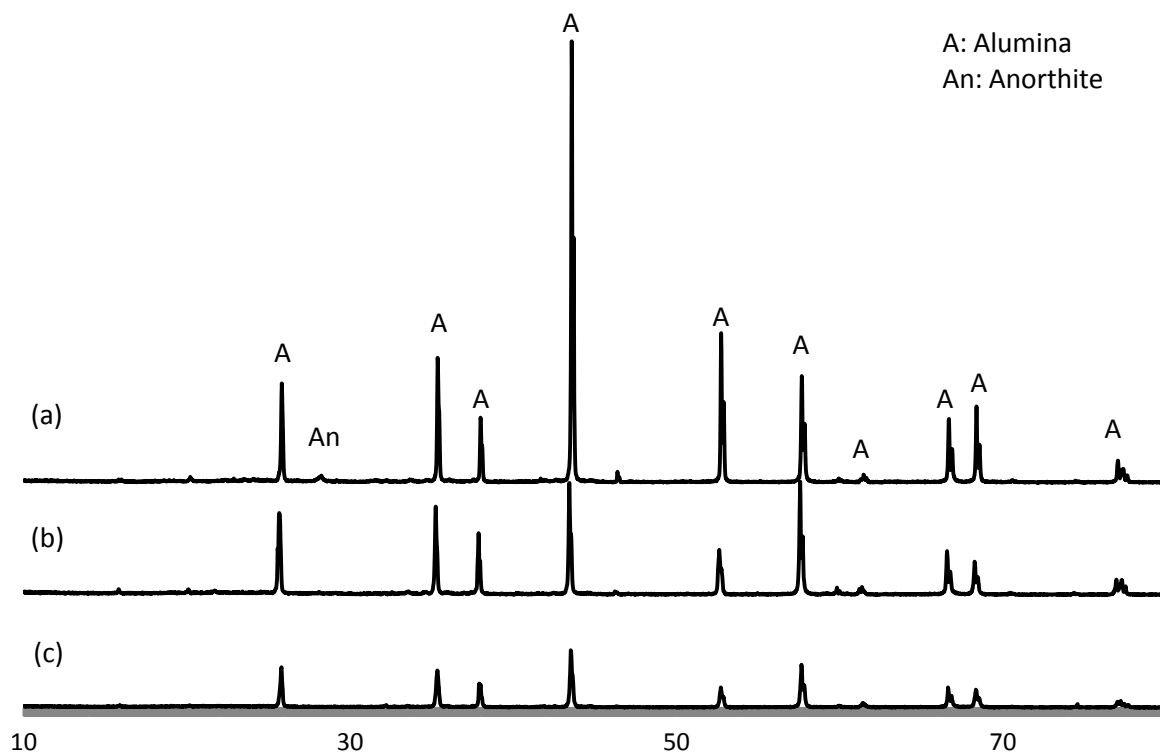


Figure 4.63 XRD pattern for (a) SFC-5, (b) SFC-3, (c) SFC-1 fired at 1000°C for 3h.

Figure 4.64 shows XRD patterns for SFCs after firing at 1300°C for 3h. Notice that in addition to the corundum phase, Cristobalite, SiO_2 (tetragonal structure with lattice parameters $a=b=0.47932$ nm and $c=0.69236$ nm) was detected in SFC-1 samples. This crystalline form of SiO_2 indicates a devitrification process of the microsilica particles starting at 1075°C, as indicated by Chakravorty and Ghosh [91]. The formation of minor contents of anorthite was detected in SFC-3 samples after firing at 1300°C for 3h (see Fig. 4.64). There are no new phases detected in SFC-5 samples besides anorthite and corundum. In particular, notice that the intensity peaks corresponding to anorthite are increased in the SFC-5 castable when the firing temperature increases from 1000°C to 1300°C.

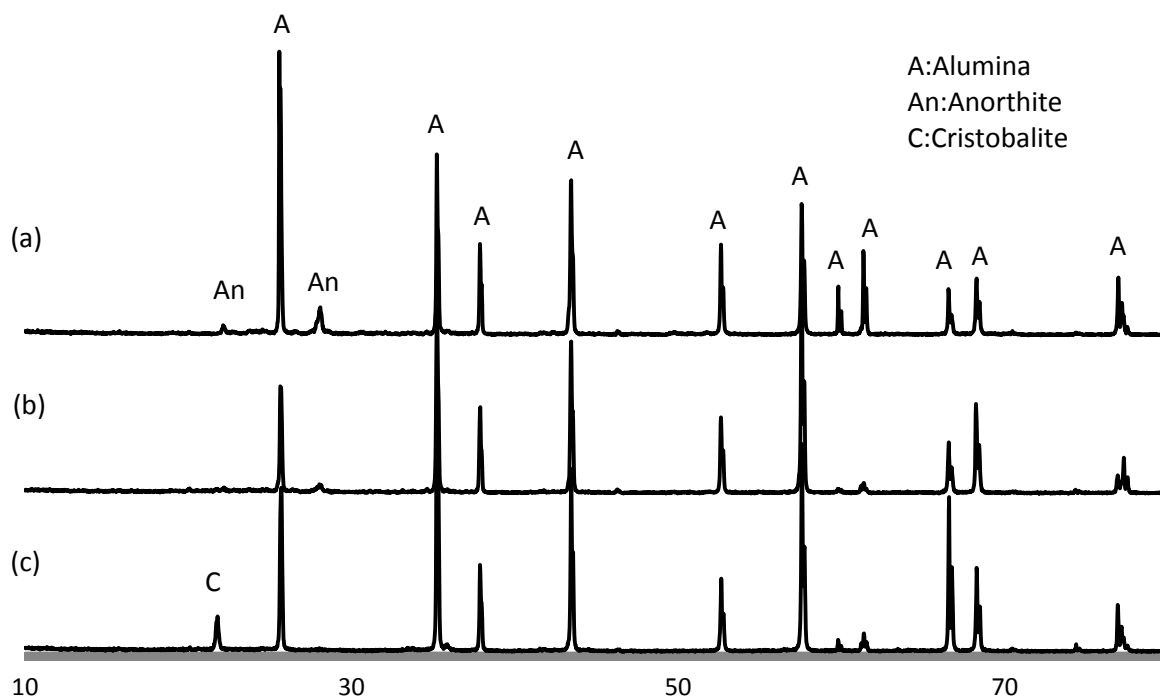


Figure 4.64 XRD pattern for (a) SFC-5, (b) SFC-3, (c) SFC-1 fired at 1300°C for 3h.

Figure 4.65 shows the XRD patterns of the SFCs fired at 1500°C for 3h. Notice the formation of mullite, $\text{Al}_6\text{Si}_2\text{O}_{13}$ (orthorhombic structure with lattice parameters $a=0.75456$ nm, $b=0.76898$ nm and $c=0.28842$ nm) at this temperature. Also, notice that the mullite intensity peaks decrease with increasing cement content (1, 3 and 5%). This is attributed to the relatively large amounts of cement which attack the mullite phase inhibiting its formation [39]. Moreover, the cristobalite intensity peaks disappear in the SFC-1 sample after firing at 1500°C for 3h. Apparently, this minor amount of cristobalite reacts with the alumina from the matrix and forms mullite at high temperatures ($\geq 1400^\circ\text{C}$). The similar XRD pattern has been reported by Gerotto[92,93] While the formation of anorthite was observed in the both, SFC-5 and SFC-3 samples, it was not

detected in the SFC-1 sample (see Fig. 4.65). Notice in particular that anorthite was first detected at 1000°C in SFC-5 samples and at 1300°C in SFC-3 samples.

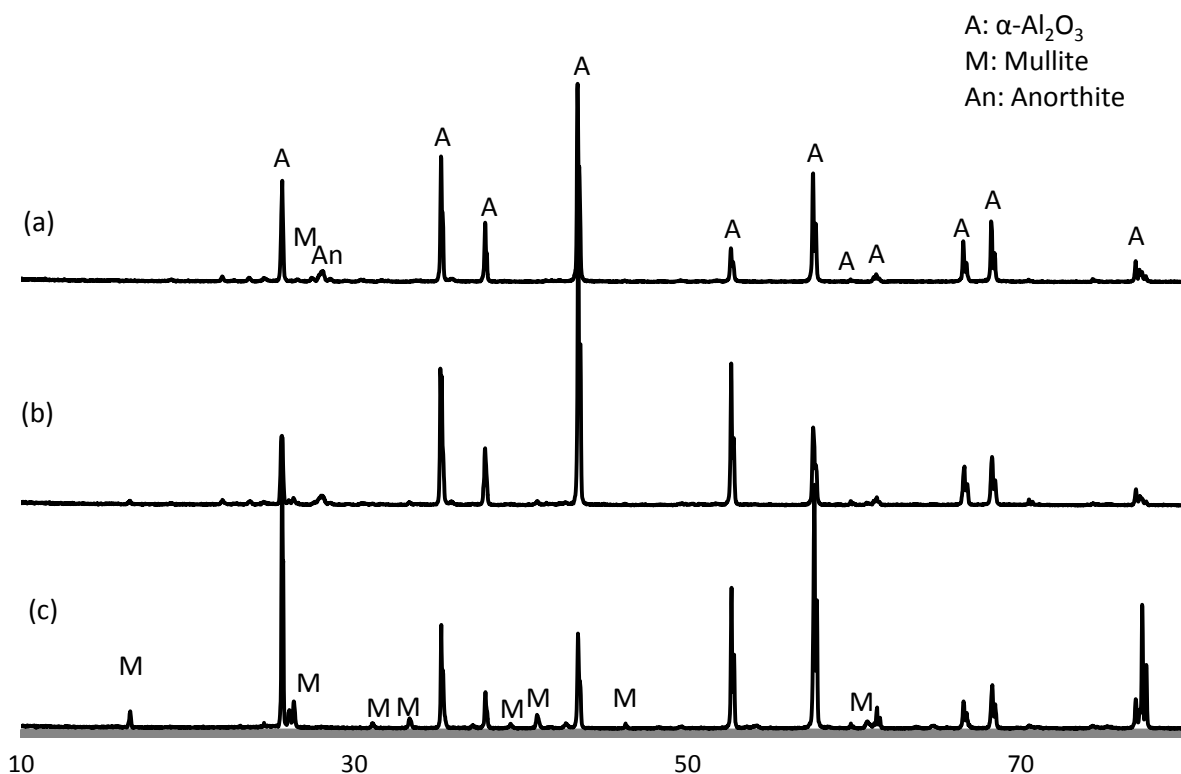


Figure 4.65 XRD pattern for (a) SFC-5, (b) SFC-3, (c) SFC-1 fired at 1500°C for 3h.

4.3 Castables Self-flow Measurements

Water addition (5.5%) was used to achieve full self-flowing properties. Under these conditions, the castables self-flowed under their own weight and easily filled intricate shape molds without any vibration. Figure 4.66 shows the self-flow values of the castables as a function of the cement content. These results show that the self-flow property values decrease from 150% to 140% when the cement content is reduced from 5% to 1%. This can be explained by the increasing hydraulic alumina content. Hydraulic alumina needs more water than cement in order to set the castables. In order to control

the setting time of the castables, it has been reported that small additions, usually around 0.5% of cement may be necessary [1]. Hence, increasing additions of hydraulic alumina would require increasing water mixing to maintain the flow. However, this approach would result in increasing castable porosity.

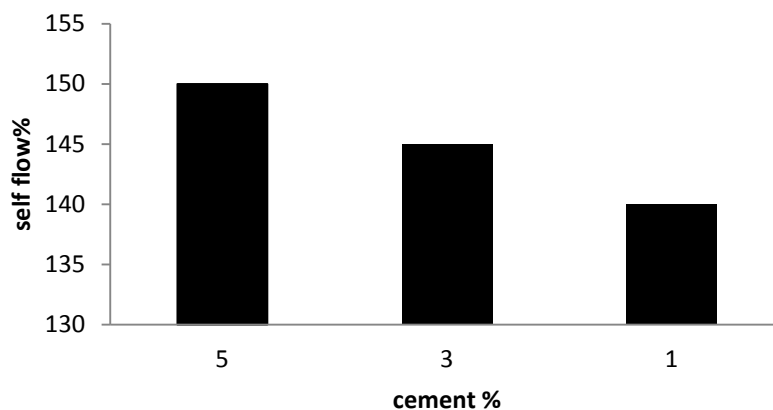


Figure 4.66 Self flow values of SFCs as a function of cement content

Figure 4.67 shows self-flow values of castables as a function of nano ZrO_2/YSZ additions. Notice that additions of nano- ZrO_2/YSZ of up to 0.1% do not have any influence on the self-flow behavior of the castables.

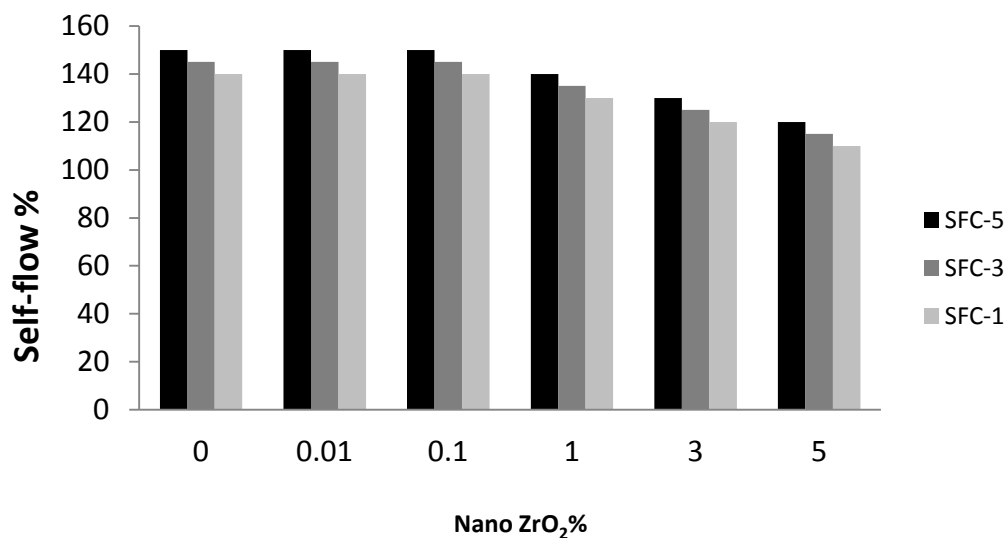


Figure 4.67 Self flow values of castables as a function of nano ZrO_2/YSZ addition.

Additions of 1% nano-ZrO₂/YSZ decrease by 10 % the self-flow values of castables as seen in Figure 4.65. Afterwards, the self-flow values steadily decrease from 10% down to 30% when the additions of nano-ZrO₂/YSZ increase from 1 to 5%.

4.4 Correlation of Zeta Potential, pH and Particle Size Distribution of Nano-ZrO₂ Powder

As mentioned before, additives have a large effect on the self-flow behavior of castables and on the uniform distribution of nano-ZrO₂/YZS particles in water based solution. D-811D and M-ADS/M-ADW are used as additives during the experiments to optimize the self-flow behavior of the castables. In order to fully understand the effect of additives on the solution, measurements were made of the zeta potential (ZP), pH and particle size distribution (PSD) of the nano particles.

Figure 4.68(a) shows the PSD of nano-ZrO₂ particles in the water based solution. The average size of commercial nano-ZrO₂ particles is 1782 nm due to agglomeration of nano-ZrO₂ particles because of the ineffective mixing method. The Zeta potential of the particles is 24.24 and the corresponding pH is 7.52. After ultrasound mixing for 20 minutes the average particle size of the nano-ZrO₂ decreases down to 185.8 nm as shown in Figure 4.68(b). Ultrasonification results in negatively charged particles and ZP changes from 24.24 to -41.39, while the pH stays constant at 7.52. Figure 4.68(c) shows the bi-modal PSD of the nano-ZrO₂ particles with the additive, D-881D (pH is 8.77). The results show that the average particle size of nano ZrO₂ is reduced from 185.8 nm down to 23.4 nm. The corresponding ZP of the particles is -52.24, proving that D811 negatively charges particles, increasing the pH from 7.52 to 9.

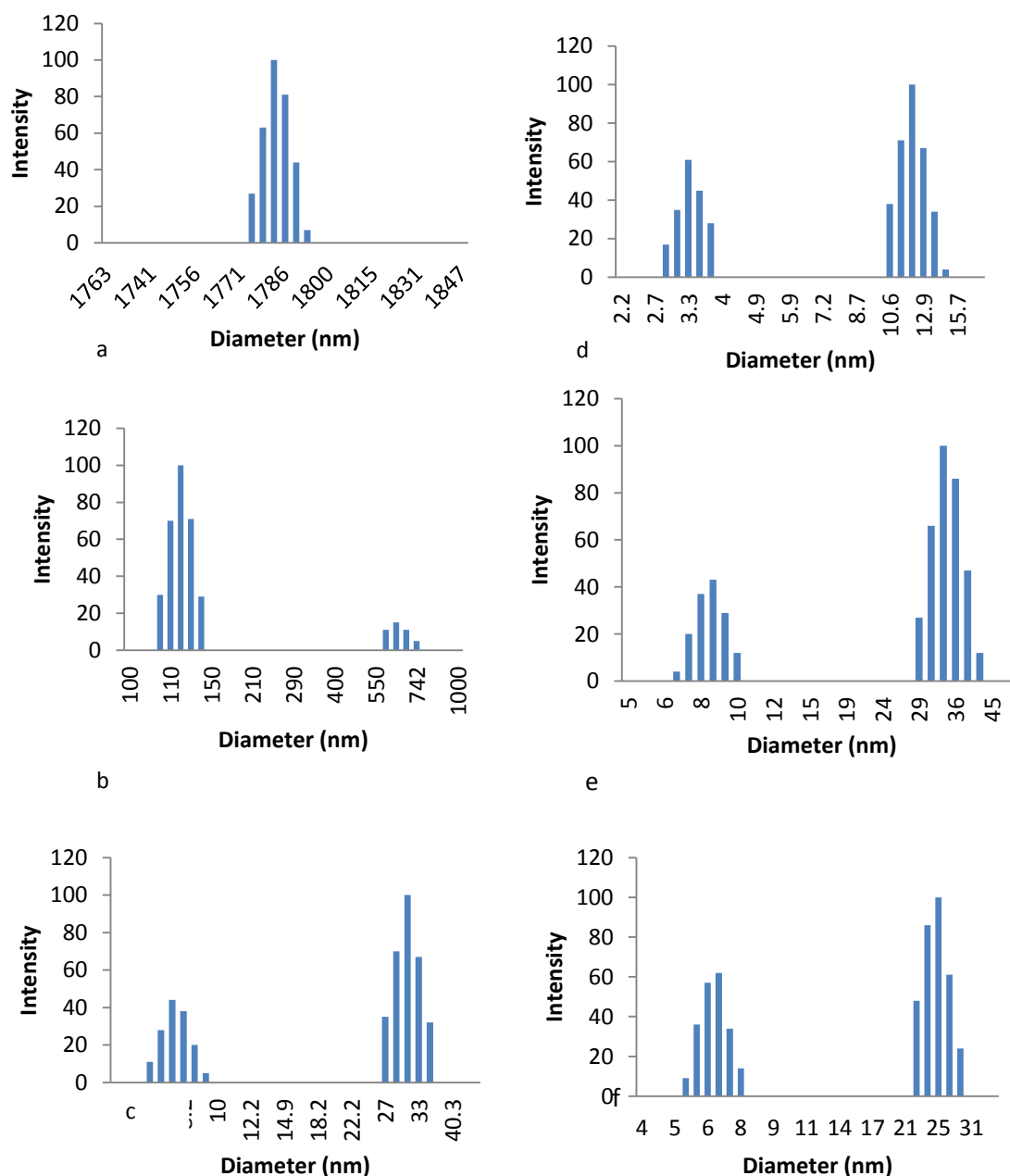


Figure 4.68 (a) PSD of nano-ZrO₂ particles in the water solution. (b) PSD of ultrasonicated nano-ZrO₂ particles in the water solution. (c) PSD of nano-ZrO₂ particles dispersed with additive (D-811D) in water. (d). The effect of ultrasonication on the PSD of nano-ZrO₂ particles with D-811D in water. (e) PSD of nano-ZrO₂ particles dispersed with additive (M-ADS) in water. (f) The effect of ultrasonication on the PSD of nano-ZrO₂ particles with M-ADS in water

Figure 4.68(d) shows the average particle size of nano-ZrO₂ with additive (D-811D) after ultrasonification for 20 minutes. The effect of ultrasound with additive further improves

the PSD, decreasing the average particle size down to 8.9 nm. While the ZP increases to -56.64, the pH remains constant at 9. Figure 4.68(e) shows the PSD of nano-ZrO₂ particles with additive (M-ADS) in the water solution. The pH of M-ADS is measured as 5.42. These results show that the average particle size is reduced down to 26.8 nm. Also, the ZP and pH are -43.95 and 5.4 respectively. In turn, this is an indication that the M-ADS negatively charges particles, thus increasing the ZP while lowering the pH and acting effectively in de-agglomeration solution. When nano-ZrO₂ particles are mixed with additive (M-ADS) in the water solution after 20 minutes of ultrasonification (see Figure 4.68(f)), the ZP increases from -43.95 to -62.33. In turn, this leads to decrease in the average particle size from 26.8 nm to 17.7 nm, resulting in a highly uniform distribution (bimodal distribution with average particle size of 6.5 nm and 23.5 nm of nano-ZrO₂ particles). There is also a slight increase in the pH from 5.4 to 5.76. Overall, the results show that the PSD of nano-ZrO₂ can be enhanced by ultrasonification and by proper use of additives like D811 and M-ADS. Alternatively, long ultrasounification times can cause heat and lead to particle agglomeration. It is found that 20 minutes of ultrasonification is the optimum time to distribute the particles efficiently.

4.5 Bulk Density, Apparent Porosity and Water Absorption of SFCs

Bulk density (BD), apparent porosity (AP) and water absorption (WA) are good indicators of the refractories quality. Hence, the main goal in the refractory industry is to produce low porosity, low water absorption and high density refractories in order to resist chemical attack at elevated temperatures. ASTM C 20-97 was used to measure the BD,

AP and WA of refractory castables at 110°C, 1000°C, 1300°C and 1500°C respectively.

Figure 4.67 shows the BD and AP of SFCs as a function of the firing temperatures.

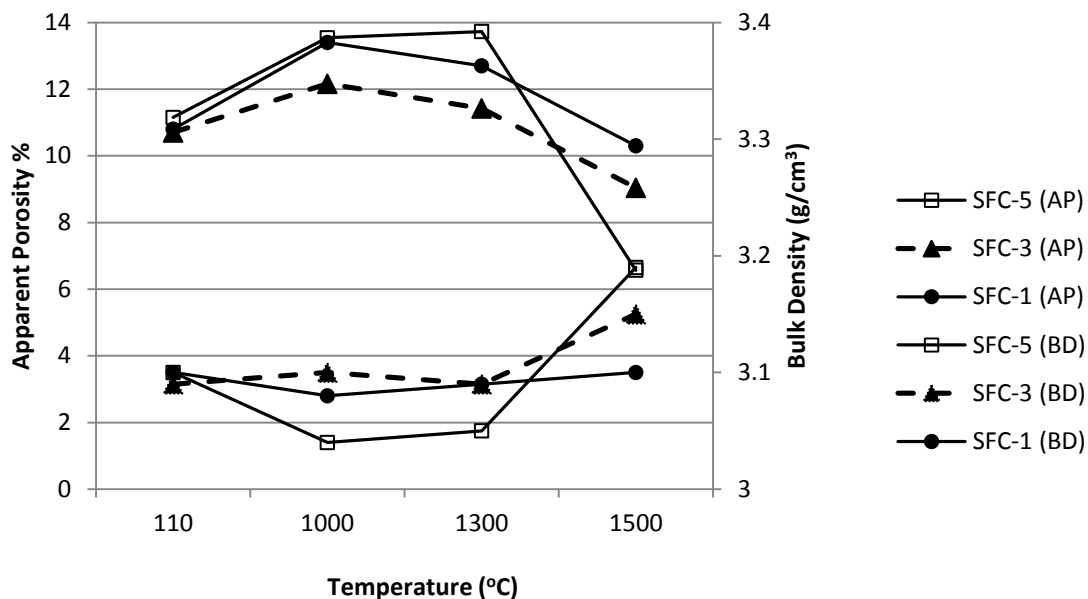


Figure 4.69 AP and BD of SFCs at different firing temperatures.

The bulk density (BD) and apparent porosity (AP) of the experimental SFCs as a function of the firing temperatures (110, 1000, 1300 and 1500°C) is given in figure 4.69. The BD of SFC-5 samples dried at 110°C for 24h was $3.096 \pm 0.09 \text{ g.cm}^{-3}$, but decreases slightly to $3.046 \pm 0.0064 \text{ g.cm}^{-3}$ after firing to 1300°C, and it increases to $3.205 \pm 0.02169 \text{ g.cm}^{-3}$ when fired at 1500°C. Water evaporation in SFC-5 creates porosity, which results in decreased BD and increased AP (10.995 ± 0.843) at 1300°C. The higher AP observed at 1300°C in the SFC-5 indicates that the pores produced during water evaporation could not be eliminated. As a result, an increased amount of anorthite ($2.74\text{--}2.76 \text{ g.cm}^{-3}$) was observed at 1300°C in the SFC-5 sample (see Figure 4.62). However, above 1300°C due to transformation of metastable liquid in the SFC-5 into mullite ($3.11\text{--}3.26 \text{ g.cm}^{-3}$), there is a significant reduction in AP to 7.0499 ± 2.30 . The BD of the SFC-3 sample dried

at 110°C for 24h, $3.092 \pm 0.075 \text{ g.cm}^{-3}$ increases to $3.157 \pm 0.0282 \text{ g.cm}^{-3}$ at 1500°C due to the formation of mullite and to the densification process. The AP of SFC-3 decreased from 11.292 ± 1.191 at 110°C to 8.776 ± 0.645 at 1500°C which confirms densification of the SFC-3 at elevated temperatures. The BD of SFC-1 slightly decreased from 3.106 ± 0.0006 at 110°C to 3.08 ± 0.0254 at 1000°C due to the dehydration process which leads to an increased AP (14.00 ± 1.09) at 1000°C. In addition, the BD gradually increases to 3.112 ± 0.008 with the formation of mullite at 1500°C, resulting in reduced AP (11.137 ± 1.38). Notice that hydrated alumina does not easily release the chemically bonded water at elevated temperatures due to its gel structure. As a result, SFC-1 containing 3% hydrated alumina develops higher AP than both, the SFC-3 (1% hydrated alumina) and the SFC-5 (zero hydrated alumina) after firing at 1500°C.

Finally, at 1500°C, the increase in BD of SFCs can be explained by the densification behavior associated with the formation of the high density mullite phase ($3.11\text{-}3.26 \text{ g/cm}^3$) and the low melting phase anorthite (CaSi_2) which fills the interspaces of the castable components. The final values in BD can be influenced to some extent by the cement content since the formation of anorthite increases at high cement contents. It is worth mentioning that the first anorthite formation was observed at 1000°C and 1300°C in SFC-5 and SFC-3 samples, respectively. No anorthite formation was observed in SFC-1 samples. Anorthite can act as a filler, helping the formation of mullite and thus contributing to ceramic bonding. In addition, up to 1300°C, the increase in the AP of castables can be attributed to the dehydration processes. Nevertheless, above 1300°C, the

AP starts to drop due to densification and to the development of new phases like anorthite, cristobalite and mullite.

Figure 4.70 gives the water absorption (WA) data based on firing temperatures and result AP values. It is evident from this figure the nature of the densification process thus confirming the AP and BD results of Fig. 4.69. WA% increases at 1000°C due to an increase in AP, but then decreases at 1500°C, as a result of the densification process in the SFCs.

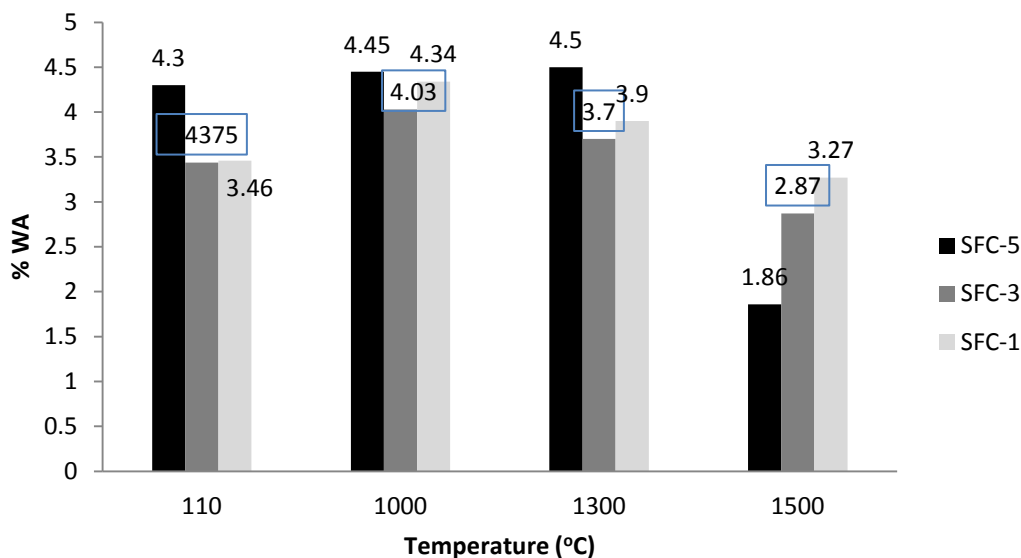


Figure 4.70 Water absorption of SFCs as a function of firing temperature.

Figure 4.71 shows the weight losses (WL) of SFCs as a function of the firing temperatures. All the castables were dried at 110°C for 24 hours in order to remove the free water which degrades the physical properties of the refractories at elevated temperatures. As seen in Figure 4.71, the WL of the castables is highest at 110°C indicating successful removal of free water. The WL of SFC-5 decreased from 1.44 at 1000°C to 1.245 at 1500°C due to densification. The WL of SFC-3 increases from 0.859

at 1000°C to 0.952 at 1300°C but then decreases to 0.919 at 1500°C after the formation of anorthite and mullite phases at 1300°C and 1500°C respectively. The WL of SFC-1 steadily increases from 0.97 at 1000°C to 1.215 at 1500°C which indicates that densification in SFC-1 is not as fast as in SFC-5 and SFC-3 samples due to the increasing amount of hydratable alumina. Notice that hydratable alumina needs more water than cement in order to develop a ceramic bond at elevated temperatures. Also, it takes time to release the chemically bonded water due to its gel structure.

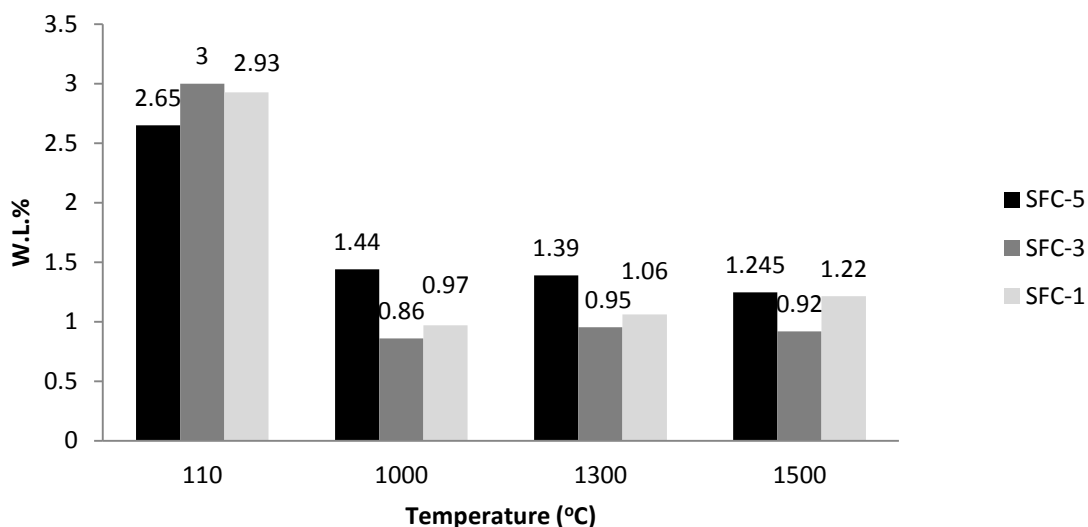


Figure 4.71 Weight losses of SFCs as a function of firing temperatures.

4.6 Thermogravimetric Analysis (TGA) and Differential Thermal Analysis (DTA) of Castables

Figure 4.72 shows TGA and DTA results of SFCs in terms of weight loss (%) and temperature difference (°C/mg) respectively as a function of firing temperatures. As expected, all the SFCs showed weight loss at elevated temperatures. In particular, there is

a characteristic drop in the weight of castables in the temperature range of 200-300°C. This weight loss is associated with the dehydration of hydrated cement of AH_3 and C_3AH_6 . Where C=CaO, A= Al_2O_3 , and H= H_2O

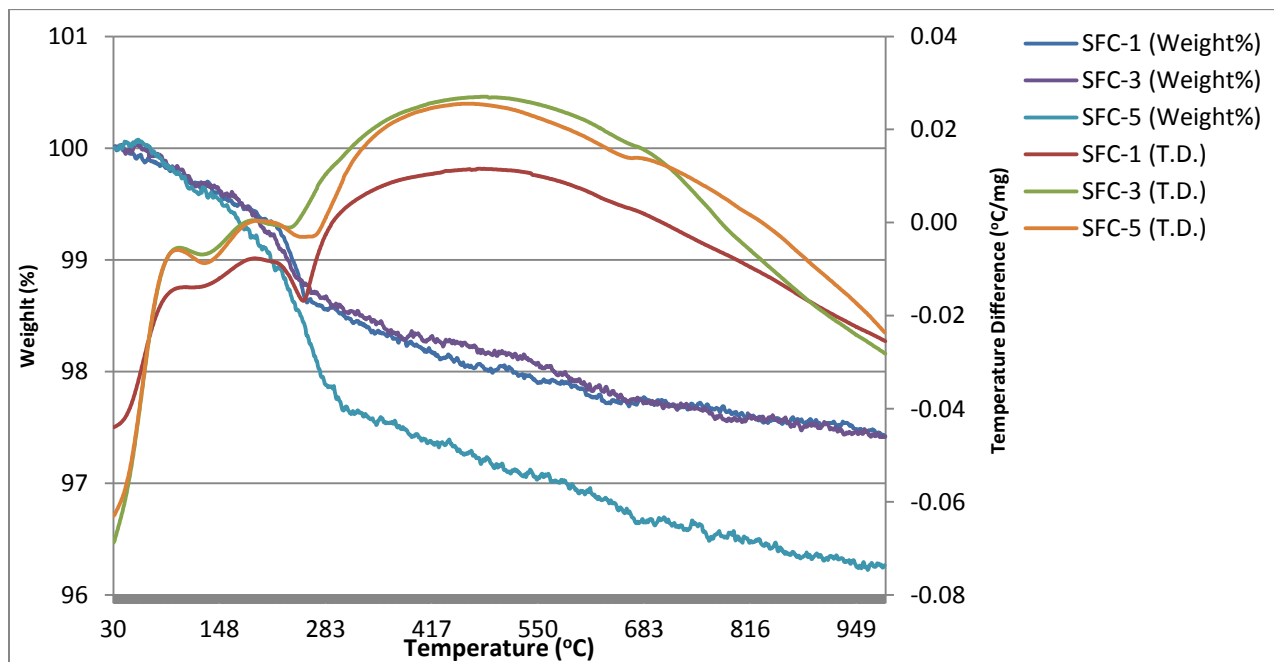
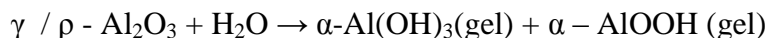


Figure 4.72 TGA and DTA of SFCs at elevated temperatures

According to the literature [1,2] dehydrating temperatures of AH_3 and C_3AH_6 are between 210-300°C and 300-360°C respectively. Advantages of the high density stable hydrates (AH_3 and C_3AH_6) at higher curing temperatures produce significant porosity with large pore sizes so that any vapor species can escape upon drying. In turn, this promotes a sharp decrease in the weight of castables as seen in the above Figure 4.72. Notice that weight loss (%) is higher in SFC-5 than in either SFC-3 or SFC-1. Since both, SFC-3 and SFC-1 contain hydrated (transitional) alumina (γ or ρ - Al_2O_3), they do not release chemically bonded water easily at elevated temperatures due to its gel

structure compared to cement. A reported [1] hydration reaction mechanism for hydrated alumina is;



The DTA results of the castables show endothermic reactions coupled with the dehydration of hydrated phases (AH_3 and C_3AH_6) at around 200-300°C. Notice that hydration starts when cement is in contact with water (exothermic reaction) and internal castable temperatures can reach temperatures of up to 75°C. C_3AH_6 is the normal, stable hydrate phase when cement curing temperatures of >35°C occur in the castable mass. The hydraulic properties of CAC are attributed to CA (calcium monoaluminate), the main phase of all kinds of CACs and hydrates per the following equation [28]:



As the temperature is increased, the process of hydration followed by dehydration process continues until all phases lose their water of crystallization. TGA results show gradually increased in weight loss (%) of castables in temperature range between 300-1000°C. In contrast, DTA results of castables show almost linear line after 300°C.

4.7 Cold Crushing Strength (CCS) of Castables

Figure 4.73 shows the exhibited cold crushing strength (CCS) as a function of the firing temperatures. At 110°C, SFC-5 containing 5% cement shows the highest CCS values due to the higher amount of cement hydrated products CAH_{10} and AH_3 that play a role in

bonding. Decrease in the cement content to 1 % (SFC-1) results in deterioration of the strength. The CCS of SFC-1 is reduced by approximately 50% and 60% when compared with SFC-3 and SFC-5 samples, respectively. In this case, the amount of cement is too small to obtain good bonding at low temperatures.

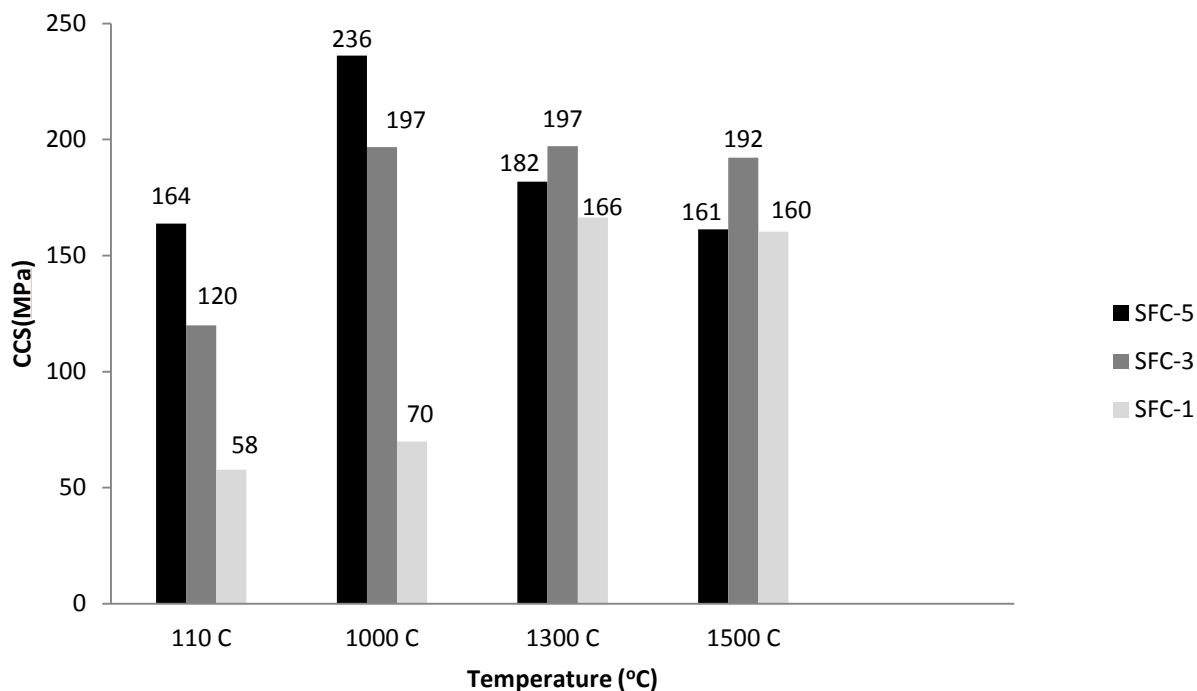


Figure 4.73 The CCS values of SFCs as a function of temperature.

The CCS of SFC-5 increases from 164 ± 22.58 MPa at 110°C to 236.13 ± 19.13 MPa at 1000°C due to the development of the ceramic bonding through the formation of anorthite. After heating at 1500°C 3h, there is reduction in the strength in the SFC-5 samples, which coincides with the increase in the formation of low melting anorthite phase. The CCS of SFC-3 increases from 119.93 ± 15.8 MPa at 110°C to 192.15 ± 9.2 at 1500°C . The increase in the CCS at increasing temperatures is attributed to the enhanced densification in the SFC-3 and to the development of ceramic phases such as anorthite at

1300°C and mullite at 1500°C. In SFC-1, there is a gradual increase strength from 57.8±4.9 MPa at 110°C to 69.9±14.2 MPa at 1000°C due to the breakdown of hydraulic bonds and to the lack of ceramic reactions. After heating at 1300°C for 3h, the CCS values of SFC-1 exhibit a significant increase to 166.4±20.763 MPa due to the crystallization of the cristobalite phase. Notice that there are no appreciable changes in the CCSs of SFCs at 1500°C even though new phases are formed. It is also important to mention that the formation of cracks was observed on the surfaces of SFCs after heating at 1500°C for 3h. Those cracks vary depending on the cement content (SFC-5 containing 5 % cement has more cracks than the SFC-3 containing 3% cement). This is explained by thermal expansion differences between the alumina aggregates and the new phases formed (anorthite, cristobalite and mullite) at elevated temperatures. These cracks can lead to a reduction in the strength and corrosion resistance of SFCs at elevated temperatures.

4.8 Modulus of Rupture (MOR) of Castables

The measured modulus of rupture (MOR) of the SFCs as a function of the firing temperature is given in Figure 4.74. At 110°C, the MOR values of SFC-5, SFC-3 and SFC-1 are 18.56±0.47 MPa, 10.39±1.87 MPa and 8.54±1.13 MPa respectively, indicating the MOR values decrease with decreased cement content. This is explained by the effect of hydratable alumina which does not lead to high amounts of hydrated products such as CAH_{10} and AH_3 at room temperature like cement does it. Hence, up to 1000°C, the SFC-5 samples show the highest MOR values due to the highest cement content (5%). In addition, the MOR is also benefited by early development of ceramic bonding due to the

formation of anorthite. After firing at 1300°C for 3h, both SFC-3 and SFC-1 show promising improvements in the MOR, as a result of the development of anorthite in SFC-3 and cristobalite in SFC-1. In contrast, the MOR of SFC-5 is negatively affected by a reduction in the formation of anorthite from 44.35 ± 4.42 MPa at 1000°C to 36.34 ± 1.3 MPa at 1300°C. At 1500°C, all the SFCs show a gradual increase in MOR values and they can be associated to the formation of the mullite phase.

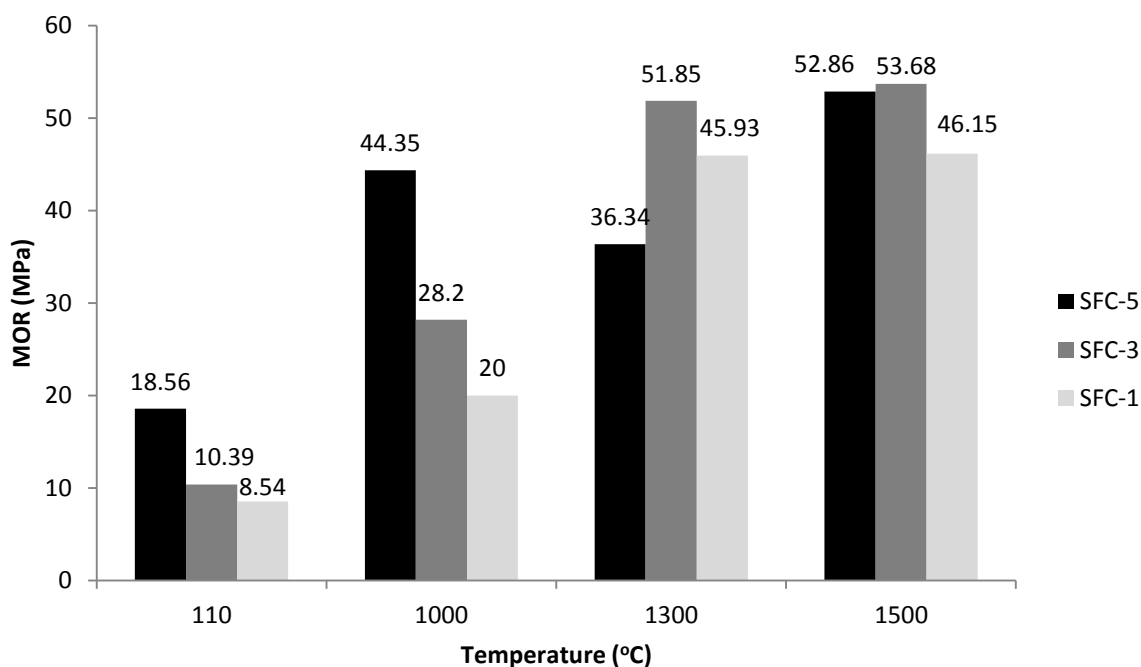


Figure 4.74 The MOR of SFCs as a function of temperature

Increase in the MOR of SFCs at 1500°C is explained by the volume increase of the alumina silica as it transforms to mullite. If the transformation takes place within the liquid phase (SFC-5 and SFC-3), the expansion causes movement of the liquid. Therefore, more pores in the castables become filled with liquid thus increasing the volume fraction where mullite can develop and contribute to the bond.

4.9 Fracture Toughness (K_{IC}) of Castables

Figure 4.75 shows the fracture toughness (K_{IC}) values of self-flowing castables (SFCs) as a function of temperature. At 110°C, K_{IC} values of SFC-5, SFC-3 and SFC-1 are 1.594 ± 0.029 , 1.09 ± 0.19 and 0.757 ± 0.03 MPa.m^{1/2} respectively. Notice that SFC-5 has the highest K_{IC} values due to the high cement content (5%), indicating that cement is a better binder than hydrated alumina at low temperatures. The K_{IC} results follow similar trends to those of MOR test results i.e., SFC-5 has the highest MOR at 110°C, and then followed by SFC-3 and SFC-1 respectively.

At 1000°C, K_{IC} of SFC-5 increases from 1.59 ± 0.03 MPa.m^{1/2} at 110°C to 3.47 ± 0.07 MPa.m^{1/2} at 1000°C, and the XRD results of SFC-5 (Figure 4.63) show that anorthite crystallizes at 1000°C. The K_{IC} of SFC-3 increases from 1.09 ± 0.19 MPa.m^{1/2} at 110°C to 3.16 ± 0.042 MPa.m^{1/2} at 1000°C as a result of densification behavior. Also, the K_{IC} of SFC-1 gradually increases from 0.757 ± 0.035 MPa.m^{1/2} to 1.373 ± 0.287 MPa.m^{1/2} which is still far lower than SFC-5 and SFC-3 due to the reduced amount of cement. At 1300°C, the K_{IC} of SFC-5 decreases from 3.47 ± 0.07 MPa.m^{1/2} at 1000°C to 2.98 ± 0.317 MPa.m^{1/2} at 1300°C due to an increase in the crystallization of anorthite as observed by XRD (Figure 4.64). In turn, this leads to degradation of the fracture toughness properties of SFC-5. The K_{IC} of SFC-3 increases from 3.16 ± 0.042 MPa.m^{1/2} at 1000°C to 3.53 ± 0.00 MPa.m^{1/2} at 1300°C. XRD results of SFC-3 (figure 4.62) detected the formation of anorthite in addition to corundum (α -Al₂O₃) at 1300°C. The K_{IC} of SFC-1 increases from 1.373 ± 0.287 MPa.m^{1/2} 1000°C to 3.055 ± 0.247 MPa.m^{1/2} at 1300°C. XRD pattern of SFC-1 (figure 4.62) shows the crystallization of cristobalite.

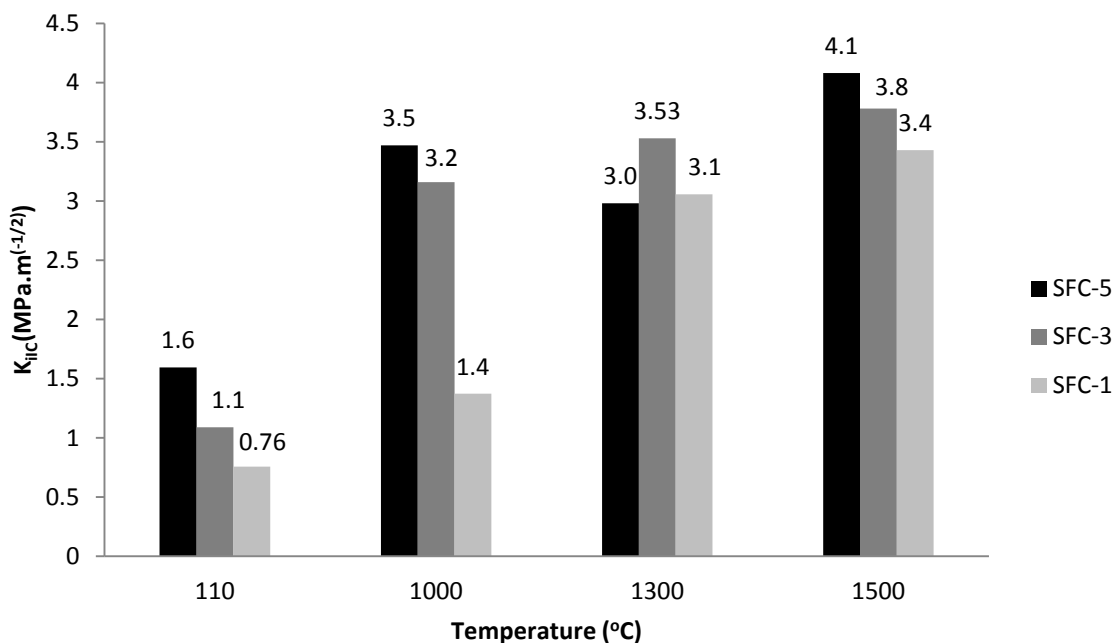


Figure 4.75 Fracture toughness values of SFCs as a function of temperature.

At 1500°C, the K_{IC} of SFC-5 increases from 2.98 ± 0.317 MPa.m^{1/2} at 1300°C to 4.08 ± 0.26 MPa.m^{1/2} at 1500°C. XRD results (Figure 4.65) show the formation of mullite and anorthite phases, including the recrystallization of corundum (α -Al₂O₃). The increase in K_{IC} is attributed to mullite due to its high density (3.16-3.22 g/cm³) and also to the low melting phase (anorthite) which fills the interspaces among the constituents. The K_{IC} of SFC-3 increases from 3.53 ± 0.00 MPa.m^{1/2} at 1300°C to 3.78 ± 0.157 MPa.m^{1/2} at 1500°C. This is in agreement with the XRD results of SFC-5 at 1500°C, which show that higher amounts of mullite and lower amounts of anorthite develop in SFC-3 (Figure 4.65). The K_{IC} of SFC-1 increases from 3.055 ± 0.247 MPa.m^{1/2} at 1300°C to 3.43 ± 0.08 MPa.m^{1/2} at 1500°C. The highest amount of mullite (based on the peak intensity) was detected in SFC-1 compared to SFC-5 and SFC-3 (Figure 4.65). In addition to mullite, recrystallization of corundum (α -Al₂O₃) was detected.

4.10 Indentation Toughness of Castables

Figure 4.76 shows indentation toughness results for SFCs as a function of the firing temperatures. As seen from Figure 4.76, the indentation toughness of SFCs increases with firing temperatures.

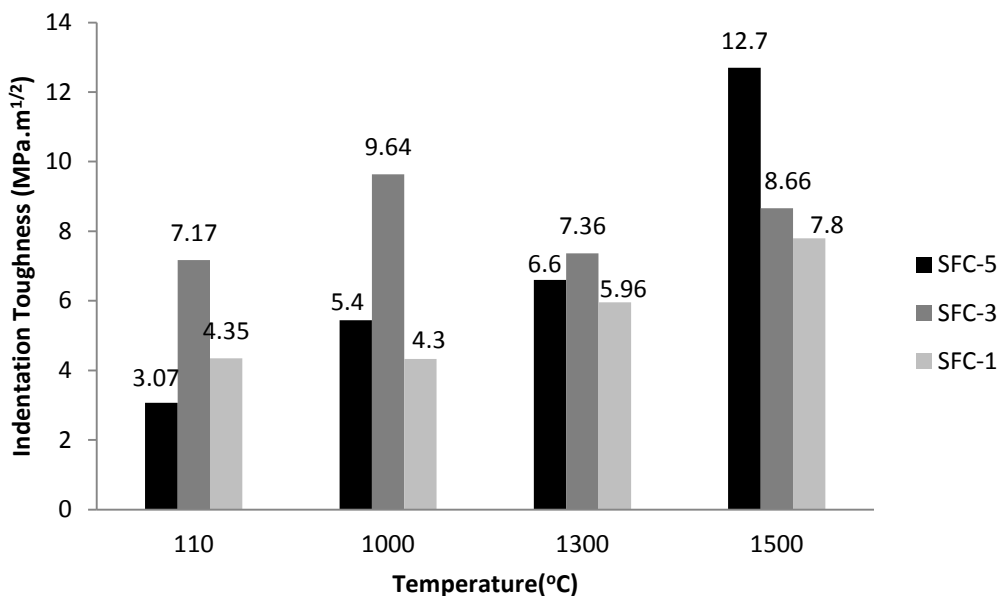


Figure 4.76 Indentation toughness of SFCs as a function of firing temperatures

In addition, indentation toughness results for SFCs based on nanoindentation are much higher than the fracture toughness results (see Chapter IV). In nanoindentation toughness measurements, it is necessary to prepare the surface of the samples prior to testing. The polishing step is crucial as it reveals the microstructure of the samples for microhardness and nanoindentation tests. Hardness and elastic modulus measurements depend on the selected area in the sample and they can vary as the matrix consists of aggregates and a binding system which have different mechanical properties. Moreover it is easier to polish the aggregate than the binding system since the binding system is rather soft.

Figure 4.77 is an optical micrograph of the binding system. Notice that in general it is made of the dark regions that surround the aggregates. Making hardness measurements on the binding system is rather difficult as it usually ends up giving rise to a blurry area. Indentation toughness measurements lead to high K_{IC} values when compared with those obtained by conventional fracture toughness determinations due to a large extent on the effect of both, aggregate and binder, as well as microstructural discontinuities (pores and microcracks) that might be inherent to specimen size effects in brittle solids.



Figure 4.77 Optical microscope picture of SFC after nanoindentation test at 400X

The crack created during hardness testing might be another reason for deviation in indentation toughness results. Figures 4.78 (a) and (b) show a crack generated using a Berkovich indenter in the nanoindentation test.

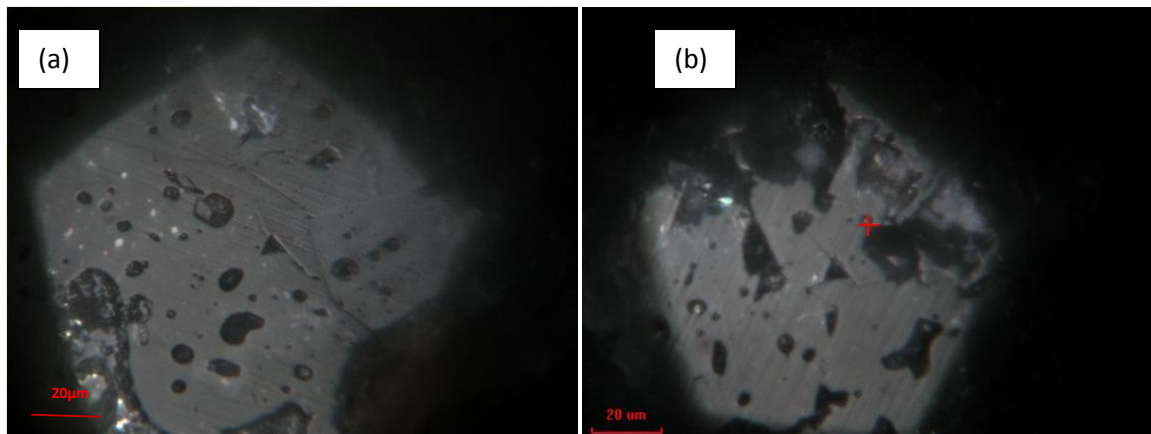


Figure 4.78 (a) Linear crack (b) Non-linear crack created by Berkovich indenter at 400X

In order to estimate the K_{IC} from indentation toughness the length of the crack needs to be measured (see Eq. 3.9). Notice that the crack should have a straight path for proper determinations. Figure 4.78(a) shows the development of a linear crack created by the indenter. On the other hand, Figure 4.78(b) shows a non-linear crack, leading to uneven results in indentation toughness. In order to avoid non-linear cracks, cube-corner indenters are desirable instead of Berkovich or vickers since cube corners are rather sharp and it is easy to generate cracks. In the literature, Berkovich type indenters are typically used to measure hardness and elastic modulus.

4.11 Effect of nano-ZrO₂ and YSZ Addition on the Modulus of Rupture (MOR) of SFCs

Effect of different amounts of nano-ZrO₂ and YSZ additions is investigated as to whether it leads to improvements in either the MOR and/or the fracture toughness of SFCs. X-ray results show that nano-ZrO₂ and 8 mol% YSZ nanopowders have a monoclinic and a cubic structure, respectively as seen Figure 4.79.

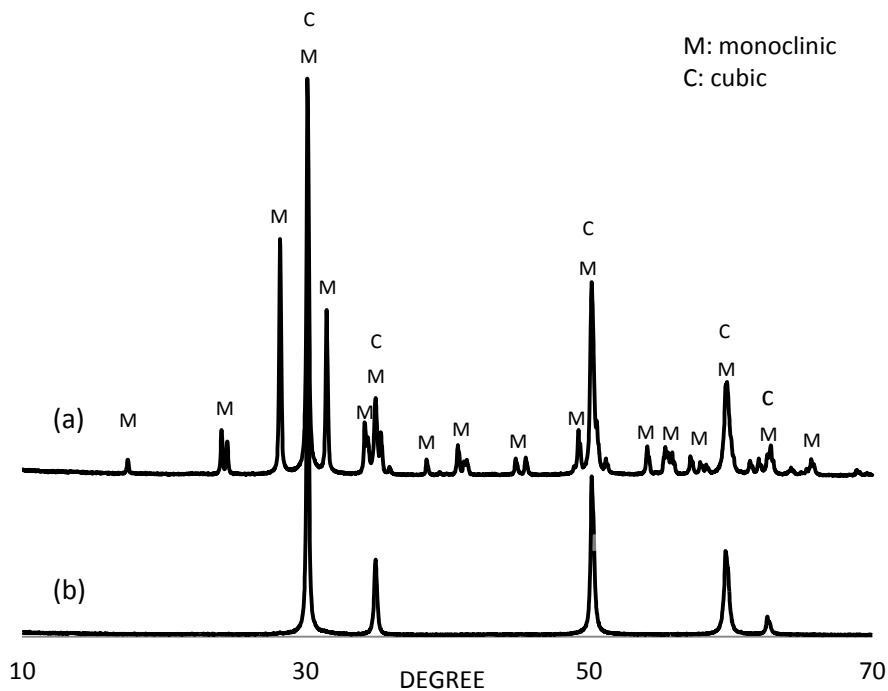


Figure 4.79 XRD patterns of (a) nano-ZrO₂ and (b) 8% mol YSZ powders

The XRD results clearly show the presence of monoclinic ZrO₂ and the formation of cubic ZrO₂ after addition of 1% YSZ at 1300°C (see Figure 4.80). In addition, anorthite and α -Al₂O₃ phases were observed. The stabilization of tetragonal ZrO₂ was not detected at additions of 8 mol% YSZ in SFC-5.

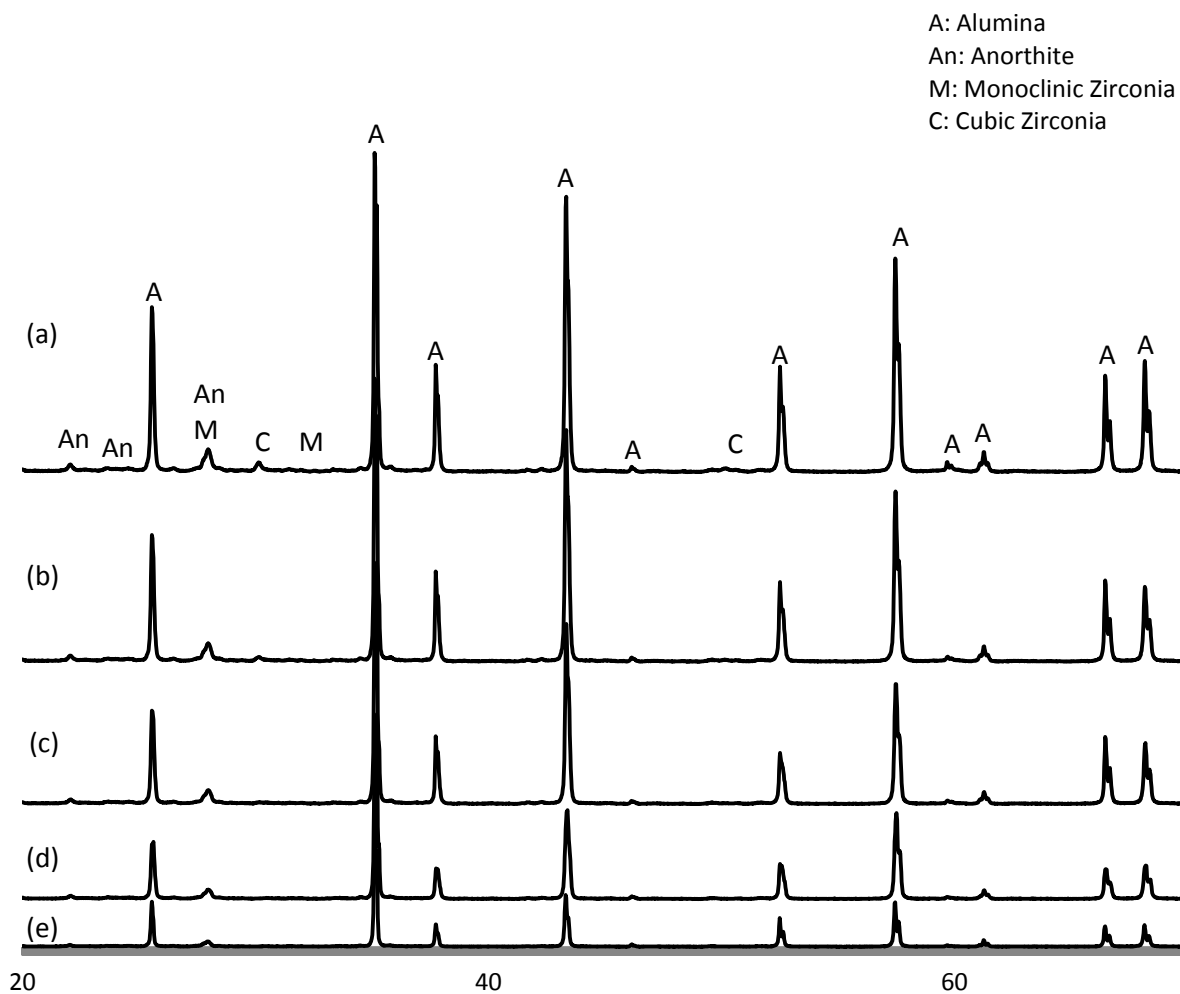


Figure 4.80 XRD data of (a) 5%, (b) 3%, (c) 1%, (d) 0.1%, (e) 0.01% - 8 mol %YSZ reinforced SFC-5 at 1300°C.

Figure 4.81 shows XRD results of ZrO₂-reinforced SFC-5 fired at 1300°C for 3 h. Diffraction peaks corresponding to t-ZrO₂ were observed after the addition of 1% ZrO₂ (Figure 4.81). In addition to t-ZrO₂, the α-Al₂O₃ (corundum), anorthite, and m-ZrO₂ were also detected.

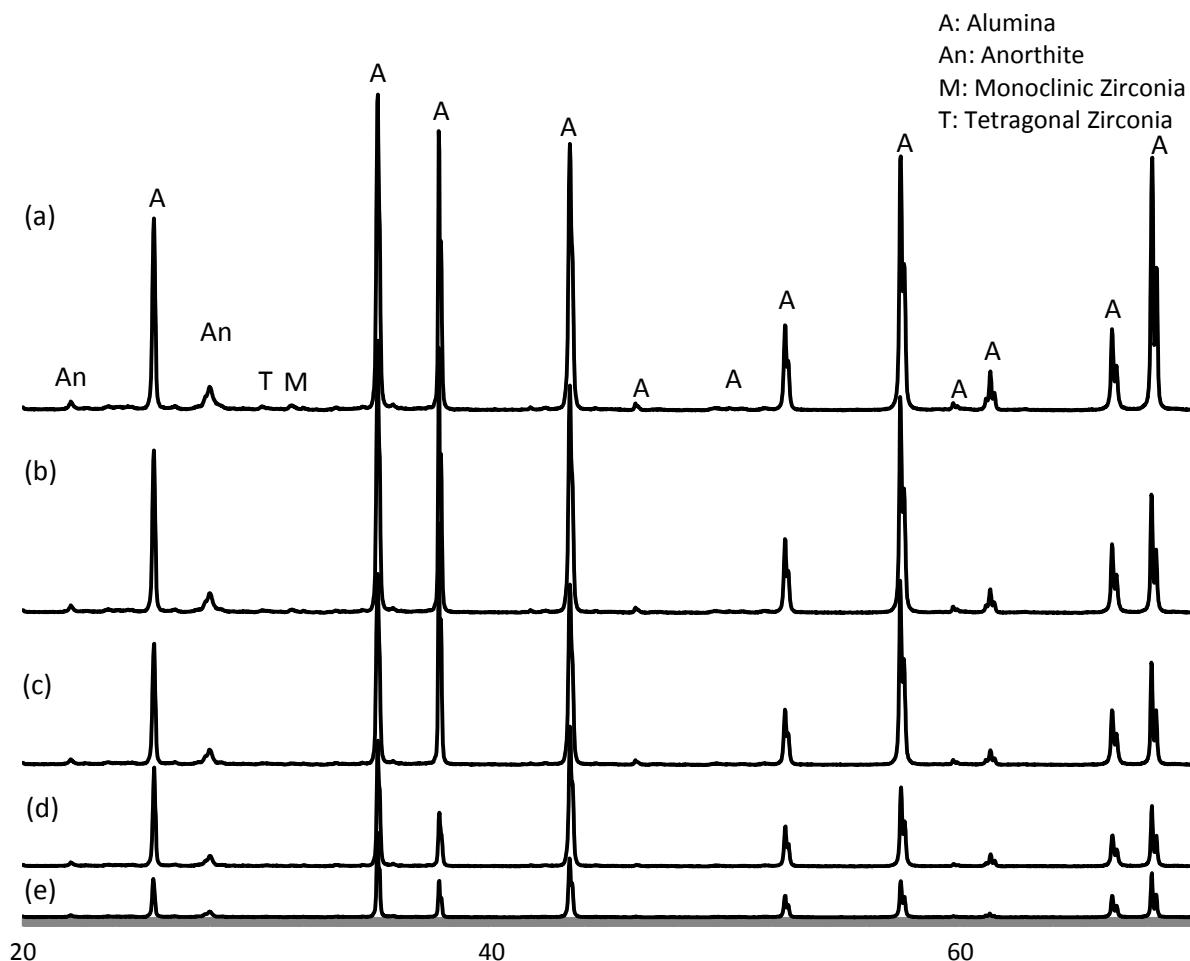


Figure 4.81 XRD data of (a) 5%, (b) 3%, (c) 1%, (d) 0.1%, (e) 0.01% - nano ZrO_2 reinforced SFC-5 at 1300°C .

The MOR of SFC-5 with nano- ZrO_2 and 8 mol% YSZ fired at 1300°C is shown in Figure 4.82. Notice that addition of 3% ZrO_2 increased the MOR from 36.34 ± 1.3 MPa to 44.32 ± 9.19 MPa. This is explained by the stabilization of t- ZrO_2 , which was detected in refractory castables (see Figure 4.81). Notice that retention of a maximum amount of t- ZrO_2 at the service temperature is important for effective transformation toughening. Thus, the stabilization of tetragonal ZrO_2 improves the MOR around 20 % with the

addition of 3% nano-ZrO₂. On the other hand, the addition of nano-YSZ does not have influence on the MOR of SFC-5 like nano-ZrO₂ did. The addition of 3% YSZ increased the MOR from 36.34±1.3 MPa to 40.42±4.98 MPa. Although there was a slight increase in the MOR of SFC-5, tetragonal ZrO₂ was not observed in the XRD results of Figure 4.78. This is attributed to the increased in packing density of the castables.

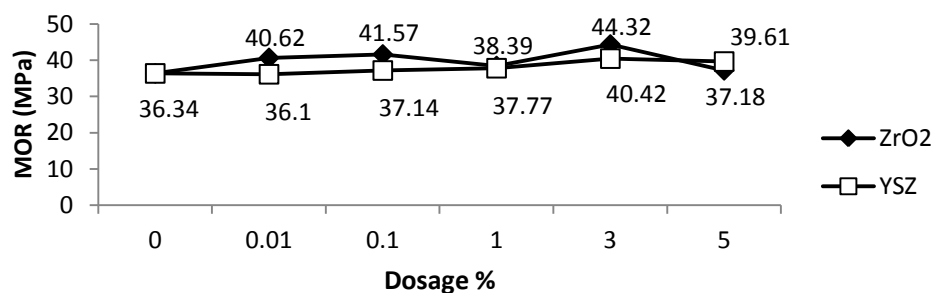


Figure 4.82 MOR of nano-ZrO₂ and YSZ reinforced SFC-5 at 1300°C.

Figure 4.83 shows K_{IC} of nano ZrO₂ and 8 mol % YSZ reinforced SFC-5 at 1300°C. As seen from Figure 4.83, the K_{IC} of SFC-5 with nano-ZrO₂ is between 2.77±0.19 - 2.94±0.26 MPa.m^{1/2}.

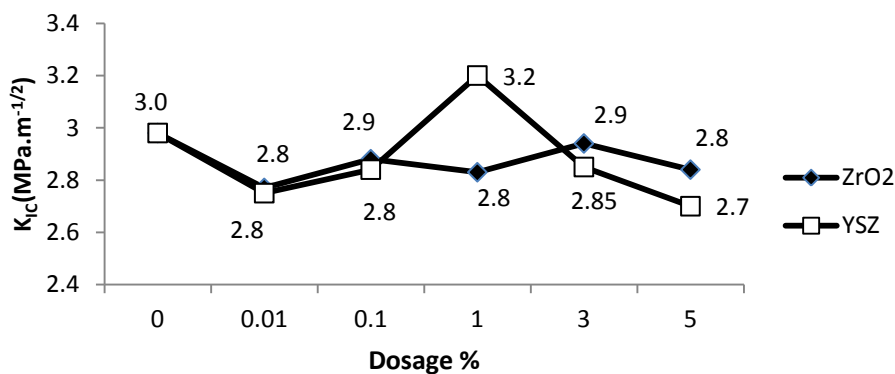


Figure 4.83 Fracture toughness of nano-ZrO₂ and YSZ reinforced SFC-5 at 1300°C.

Although retention of t-ZrO₂ is achieved, the addition of nano-ZrO₂ does not have a major effect on the K_{IC} of refractories. The addition of YSZ changes the K_{IC} of castables between 2.75 ± 0.22 - 3.2 ± 0.11 MPa.m^{1/2}, which is slightly higher when compared with the reference. Thus, there is no significance effect of the additions of nano-ZrO₂ and 8 mol% YSZ on K_{IC} of SFC-5. Figure 4.84 shows XRD pattern of ZrO₂ reinforced SFC-3 at 1300°C. Also, t-ZrO₂ was observed after addition of 0.1% ZrO₂. In addition to t-ZrO₂, α-Al₂O₃, anorthite and m-ZrO₂ were detected in XRD.

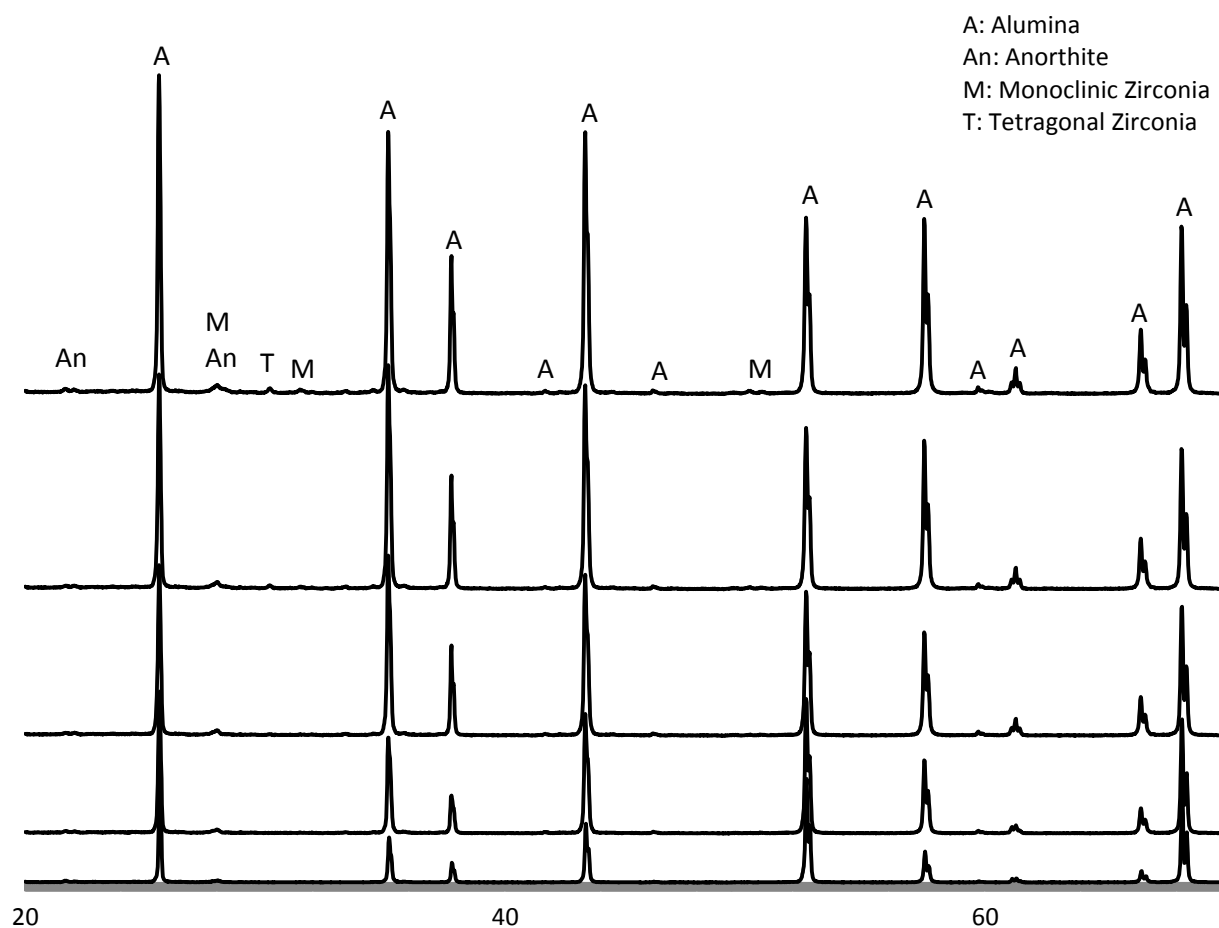


Figure 4.84 XRD data of (a) 5%, (b) 3%, (c) 1%, (d) 0.1%, (e) 0.01% nano-ZrO₂-reinforced SFC-3 fired at 1300°C

Figure 4.85 shows XRD data of 8 mol% YSZ reinforced SFC-3 after firing at 1300°C for 3h. From the diffraction peaks, c-ZrO₂ was detected after addition of 1% YSZ. In addition, m-ZrO₂, α -alumina and anorthite phases were detected. The formation of t-ZrO₂ was not detected with the addition of YSZ.

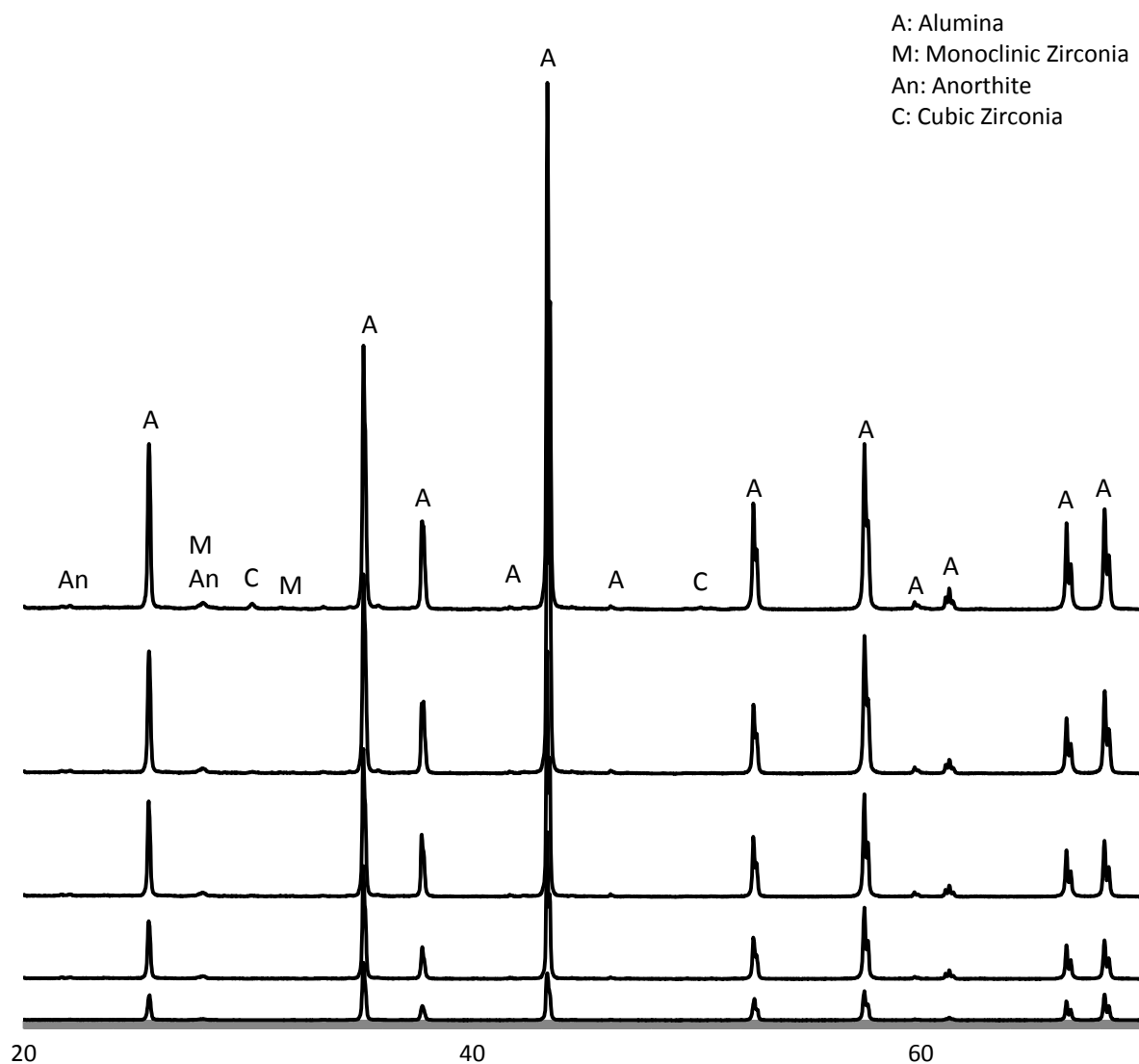


Figure 4.85 XRD data of (a) 5%, (b) 3%, (c) 1%, (d) 0.1%, (e) 0.01% - 8 % mol YSZ reinforced SFC-3 fired at 1300°C.

The MOR for SFC-3 with nano-ZrO₂ and YSZ fired at 1300°C is shown in Figure 4.86. The addition of 3% ZrO₂ increased the MOR from 51.9±2.5 MPa to 59.5±2.5 MPa. This is attributed to the stabilization of tetragonal ZrO₂, which was detected in SFC-3 (Figure 4.84). The addition of YSZ does not have a major influence on the MOR of SFC-3 since the stabilization of tetragonal ZrO₂ was not achieved in YSZ-reinforced castables (Figure 4.85).

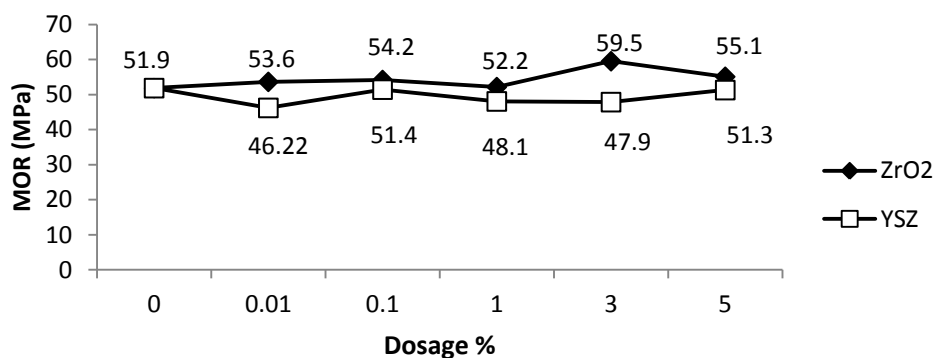


Figure 4.86 MOR of 8 mol%-YSZ and ZrO₂ reinforced SFC-3 at 1300°C for 3h.

The K_{IC} of SFC-3 with nano-ZrO₂ is between 3.0±0.3 and 3.6±0.3 MPa.m^{1/2}. Although retention of t-ZrO₂ is achieved, the addition of nano-ZrO₂ does not have a major influence on the K_{IC} of SFC-3. The addition of YSZ changes the K_{IC} of SFC-3 between 3.0±0 and 3.4±0.3 MPa.m^{1/2}, which is slightly reduced when compared with the reference as seen Figure 4.87.

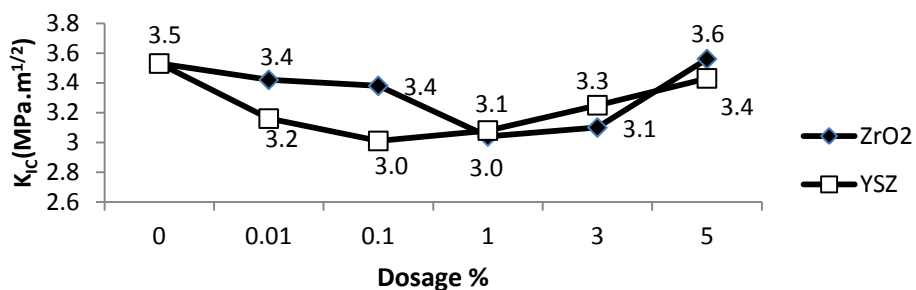


Figure 4.87 K_{IC} of nano-ZrO₂ and 8 mol % YSZ reinforced SFC-3 at 1300°C.

Figure 4.88 shows XRD data of nano-ZrO₂ reinforced SFC-1 fired at 1300°C. Diffraction peak of t-ZrO₂ was observed after addition of 1% ZrO₂. In addition, diffraction peaks belonging to α -Al₂O₃, m-ZrO₂ and cristobalite were observed as seen Figure 4.88.

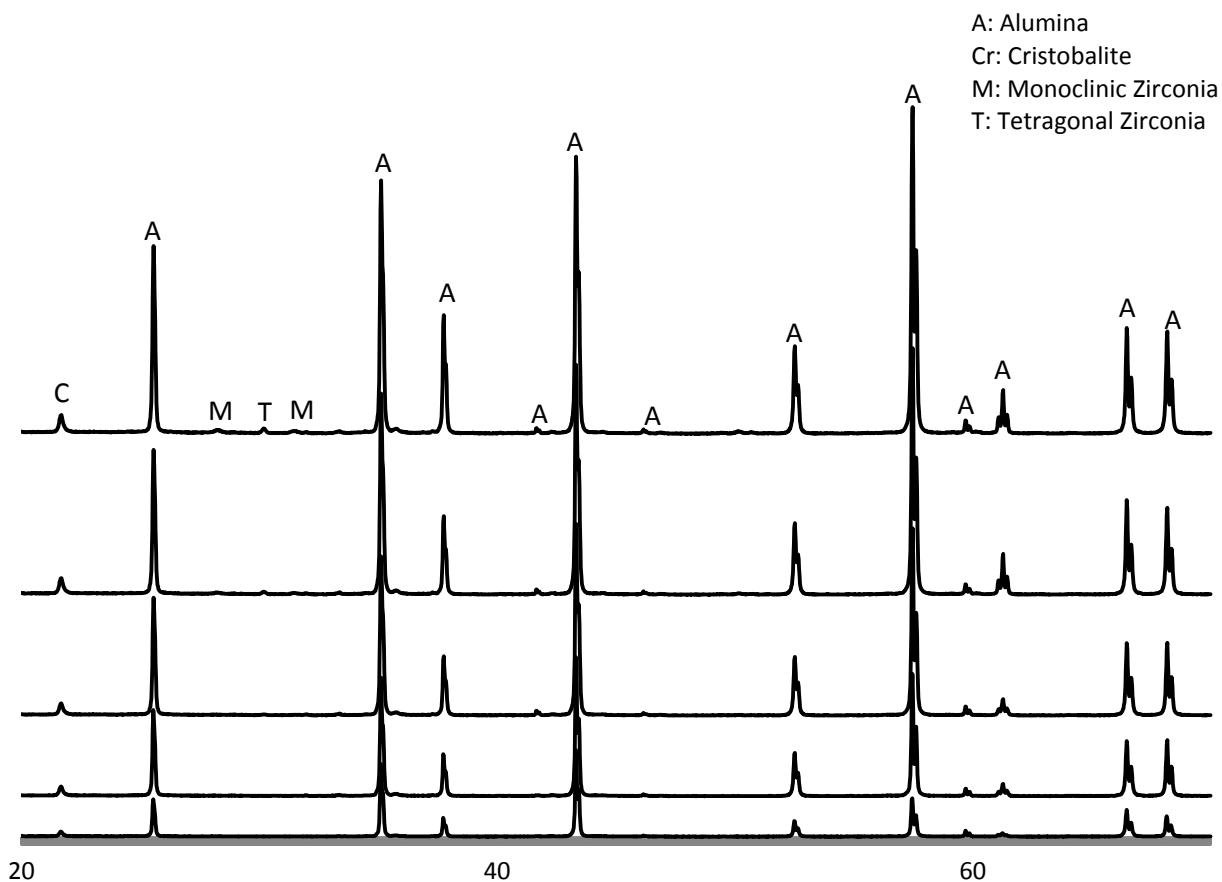


Figure 4.88 XRD data of (a) 5%, (b) 3%, (c) 1%, (d) 0.1%, (e) 0.01% nano-ZrO₂-reinforced SFC-1 fired at 1300°C for 3h.

Figure 4.89 shows XRD patterns of an 8 mol % YSZ reinforced SFC-1 at 1300°C. c-ZrO₂ was detected after addition of 1% YSZ. In addition, α -Al₂O₃, m-ZrO₂ and the formation of cristobalite phases were detected as those observed in nano-ZrO₂ reinforced SFC-1. The retention of t-ZrO₂ was not detected at room temperature.

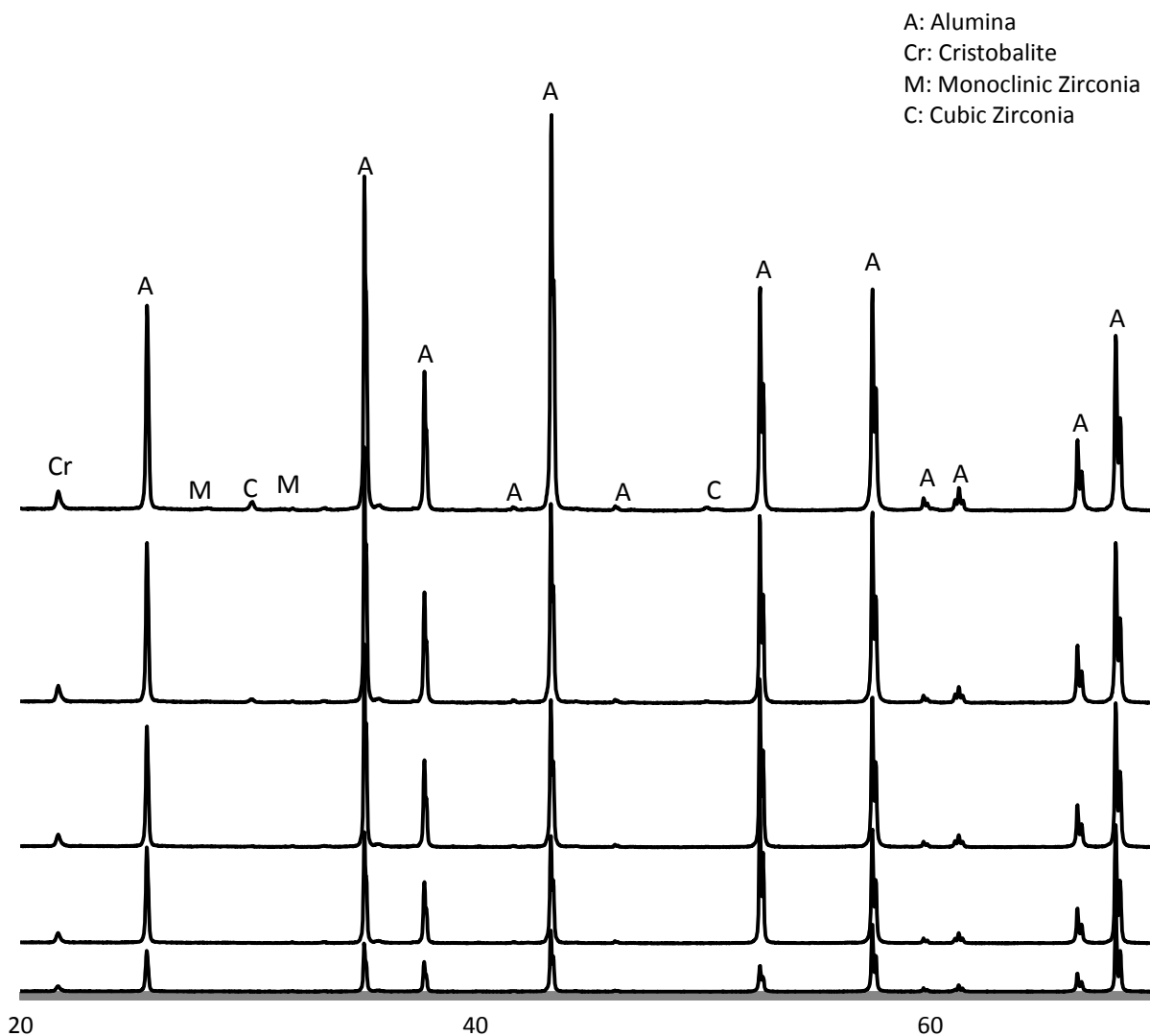


Figure 4.89 XRD data of (a) 5%, (b) 3%, (c) 1%, (d) 0.1%, (e) 0.01% - 8 % mol YSZ reinforced SFC-1 fired at 1300°C

Figure 4.90 shows the MOR of nano-ZrO₂ reinforced SFC-1 fired at 1300°C. The addition of 3% nano-ZrO₂ increased the MOR from 45.9±1.71 MPa to 52±1.39 MPa. That is attributed to stabilization of t- ZrO₂ at room temperature which is similar to both, the SFC-5 and SFC-3 samples. On the other hand, the addition of YSZ slightly changed the MOR of SFC-1 due to the fact that retention of t-ZrO₂ at room temperature was not detected in YSZ reinforced SFC-1 samples as seen Figure 4.90.

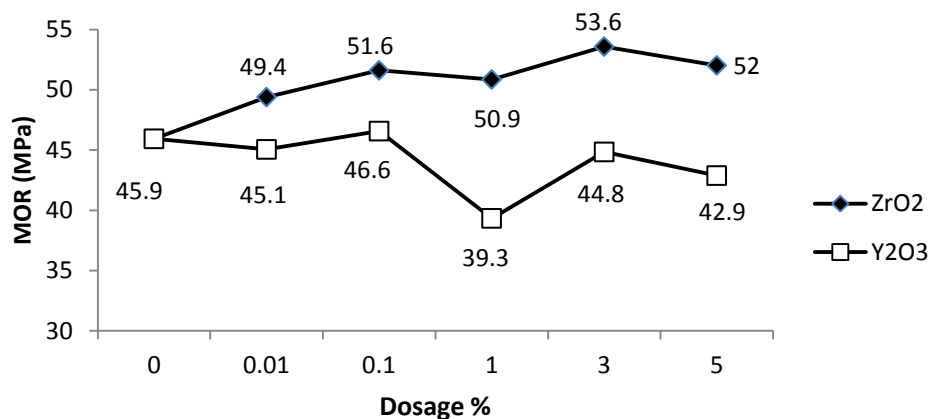


Figure 4.90 The MOR of 8 mol %YSZ and ZrO₂ reinforced SFC-1 at 1300°C.

The K_{IC} results of nano-ZrO₂ and 8 mol% YSZ reinforced SFC-1 fired at 1300°C for 3h are given in Figure 4.91. Notice that the addition of nano-ZrO₂ and 8 mol% YSZ changed the K_{IC} between 3 ± 0.15 - 3.3 ± 0.425 MPa.m^{1/2} and 2.7 ± 0.08 - 3.2 ± 0.789 MPa.m^{1/2} respectively. The addition of both, nano-ZrO₂ and YSZ does not show any effect on the K_{IC} of SFC-1 samples regardless of the retention of t-ZrO₂.

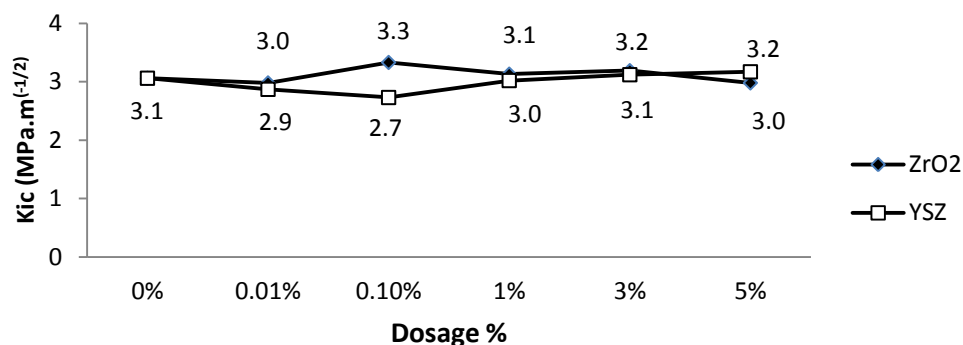


Figure 4.91 Fracture toughness of nano- ZrO₂ and 8 mol % YSZ reinforced SFC-1 at 1300°C.

Consequently, it is found that the addition of nano-ZrO₂ on the experimental tests show that there are some benefits in some of the experimental castables. Figures 4.82, 4.86 and 4.90 show the MOR of nano-ZrO₂ reinforced SFCs fired at 1300°C for 3h. Notice that the MOR of all SFCs exhibited an increase of around 20% with the addition of 3% nano-ZrO₂. Apparently, this is attributed to the stabilization of tetragonal-ZrO₂ at room temperature (see XRD results Figures 4.81, 4.84 and 4.88). In contrast, additions of nano-ZrO₂ did not lead to appreciable improvements in the fracture toughness (K_{IC}) of the experimental castables, regardless of cement content and firing temperatures (see Figures 4.83, 4.87 and 4.91). The X-ray diffraction of the nanopowders added to SFCs shows a monoclinic structure as seen Figure 4.79. In the nano-ZrO₂ reinforced castables, no new phases were identified that could be attributed to the presence of nano-ZrO₂ as shown in Figures 4.81, 4.84 and 4.88. In these Figures, XRD intensity peaks corresponding to t-ZrO₂, α-Al₂O₃ (corundum), m-ZrO₂, anorthite(CaAl₂Si₂O₈) and cristobalite phases were detected depending on the cement content. It is important to optimize the tetragonal ZrO₂ structure at service temperature since transformation toughening occurs by stabilization

of tetragonal ZrO_2 at room temperature. Although XRD pattern shows the tetragonal ZrO_2 peak in nano- ZrO_2 addition, amount of t- ZrO_2 is not enough to improve the fracture toughness. On the other hand, no tetragonal ZrO_2 peak is seen in 8 mol% YSZ in XRD results (see Figures 4.80, 4.85 and 4.89)., indicating that transformation toughening does not take place.

4.12 Modulus of Rupture of Binding System

Less than 150 micron powders were used in order to determine the strength of the binding systems. The MOR of binding systems of SFCs is given in Figure 4.92. The results are similar to the MOR results of the matrix system (Figure 4.74). Up to 1000°C , the binding of SFC-5 shows the highest MOR due to early development of ceramic bonding such as: anorthite due to the higher cement content.

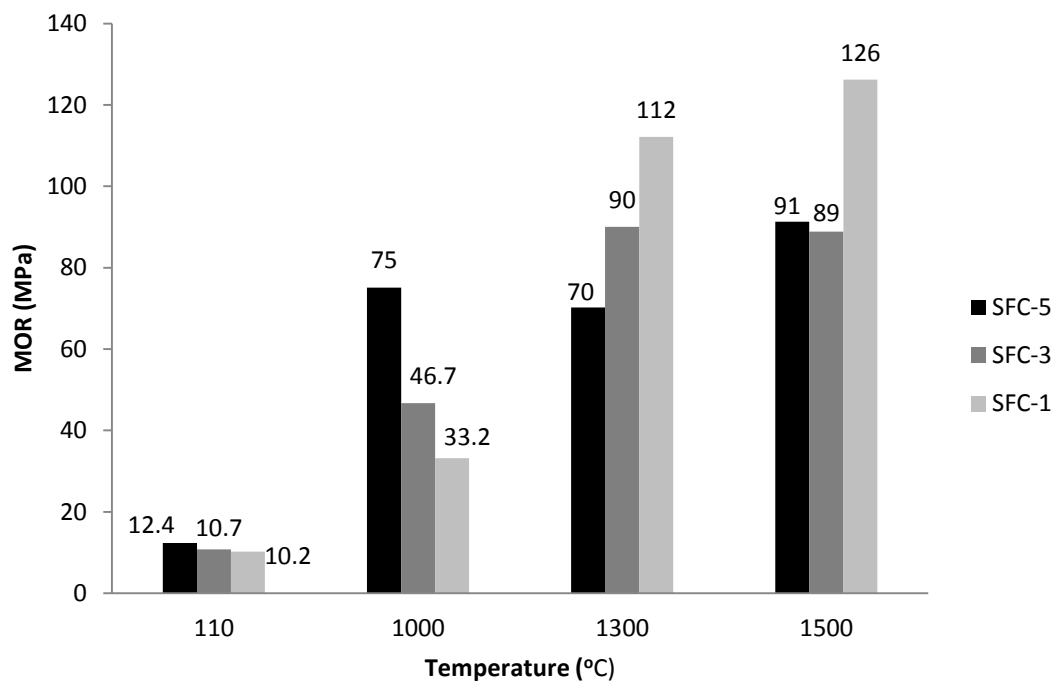


Figure 4.92 The MOR of binding systems of SFCs as a function of temperature.

After firing at 1300°C for 3h, the binding systems of SFC-3 and SFC-1 show a significant increase in the MOR because of development of ceramic bonding through anorthite for SFC-3 and cristobalite for SFC-1 which is similar to the matrix systems. On the other hand, the MOR of SFC-5 is negatively affected by increasing amounts of anorthite formation fired at 1300°C. At 1500°C, the MOR of SFCs increased through the formation of mullite. The MOR results of binding systems of SFCs are noticeably higher than in the matrix systems of SFCs at elevated temperatures. This is attributed to the development of ceramic bonding through the binding system, leading the stronger bonding since aggregates do not have any effect on the development of ceramic bonding.

Notice that there is no crack formation observed in the binding systems as opposed to the matrix systems of SFCs. This is attributed to thermal expansion differences between alumina aggregates and the phases formed at elevated temperatures such as; anorthite, cristobalite and mullite, leading to cracking. Notice that amount of cracks increases with higher cement content due to increasing amount slow melting phase (anorthite) as seen figure 4.105. It is important to keep in mind that these cracks would reduce the corrosion resistance of castables at elevated temperatures, leading reduced service times of castables.

4.13 Fracture Toughness of Binding Systems of Castables

Fracture toughness of binding systems of SFCs as a function of firing temperatures is given Figure 4.93. Up to 1000°C, the K_{IC} of binding system increases with increased

cement content since the higher cement leads to early development of ceramic matrix as previously mentioned.

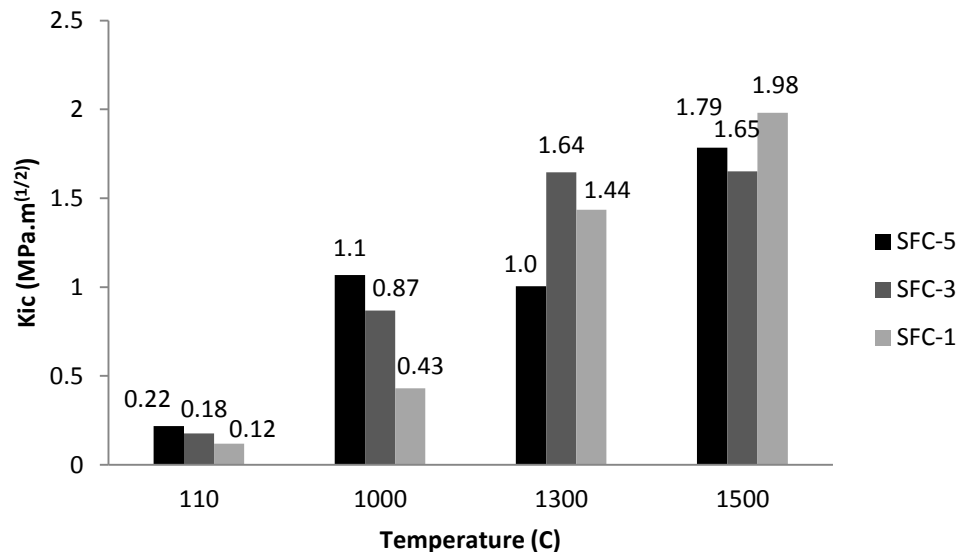


Figure 4.93 K_{IC} of binding systems of SFCs as a function of firing temperature

At 1300°C, there was a slight decrease in the composition based on SFC-5 due to increasing amounts of anorthite formation. On the other hand, a significant increase was observed in the compositions based on SFC-3 and SFC-1, indicating the formation of ceramic bonding. At 1500°C, the K_{IC} of binding systems increases with the formation of mullite phase at this temperature. In general, the K_{IC} results of the binding systems were gradually lower than those of the matrix systems of SFCs (see Figure 4.75). This can be explained by the effect of aggregates since bonding with the binding system at elevated temperatures, leading to an increase in fracture toughness of SFCs. In particular, the formation of the anorthite phase leads to improved binding between aggregate and the binding system since anorthite acts as a filler between aggregate and the binding system.

The results are also confirmed by experimental observations of fracture in the aggregates as seen Figure 4.103(b).

4.14 Effect of Nano-ZrO₂ addition on the MOR of Binding System of Castables

Figure 4.94 shows the MOR of nano-ZrO₂ and YSZ reinforced binding systems of SFC-5 as a function of firing temperatures. Up to 1000°C, there was no big difference in the MOR of nano-ZrO₂ and YSZ reinforced samples. After firing at 1300°C, YSZ increased the MOR of binding system from 79.9±10.2 MPa at 1000°C to 113±5.6 MPa at 1300°C which is higher compared to nano-ZrO₂ reinforced samples. At 1500°C, nano-ZrO₂ addition shows the highest MOR values from 93±2.2 MPa at 1300°C to 142±13.9 MPa at 1500°C. Notice that nano-ZrO₂ and YSZ reinforced SFC-5 do not show any effect in the MOR after firing at 1300°C compared with non-reinforced samples as seen Figure 4.94.

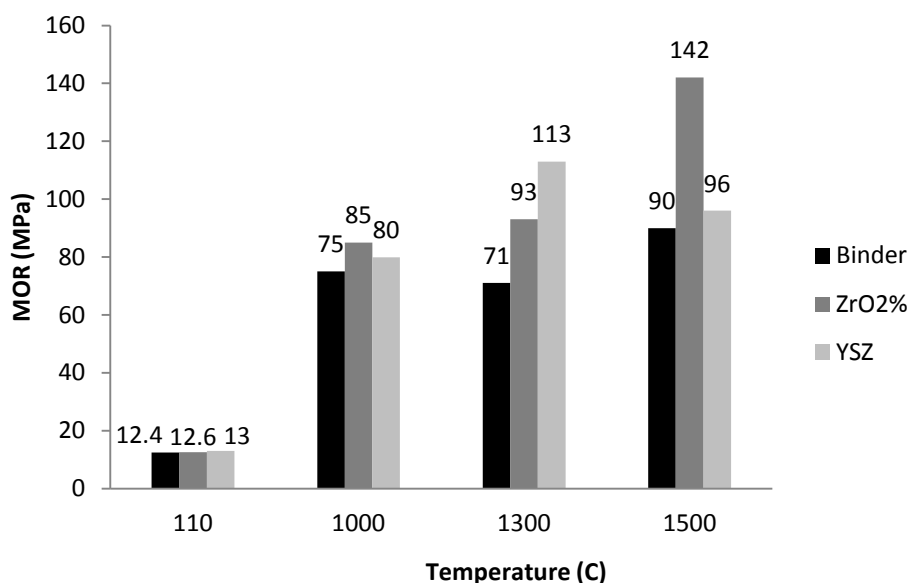


Figure 4.94 MOR of binding system of SFC-5 as a function of firing temperatures

Figure 4.95 shows the MOR of nano-ZrO₂ and YSZ reinforced binding systems of SFC-3 at elevated temperatures. Nano-ZrO₂ addition shows the highest MOR after firing at 1300°C (117.82±9.34 MPa). At 1500°C, the addition of both nano-ZrO₂ and YSZ increases the MOR compared with non-reinforced samples.

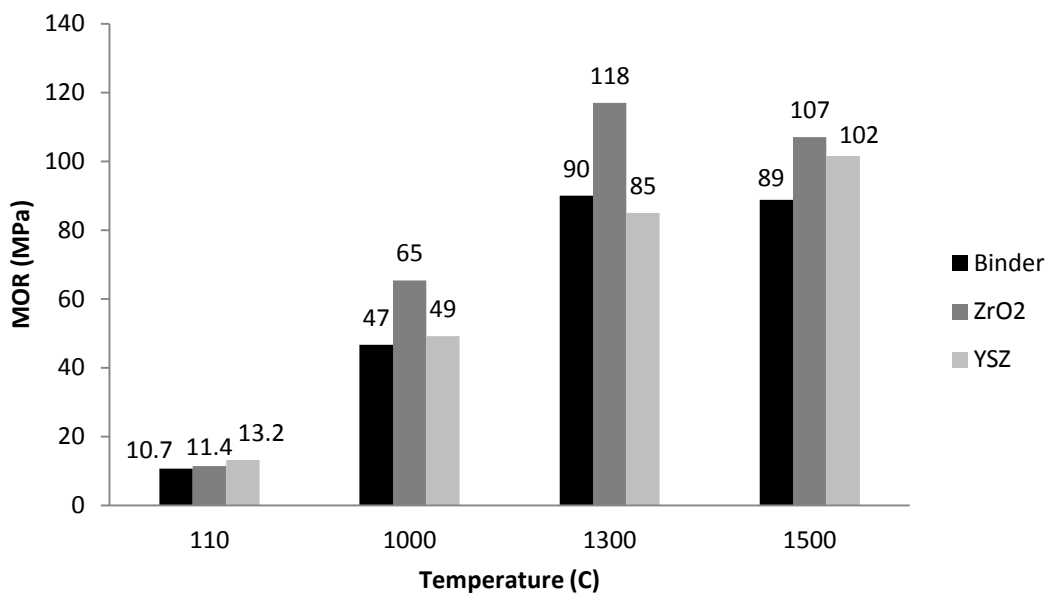


Figure 4.95 MOR of binding system of SFC-3 as a function of firing temperatures.

Figure 4.96 shows the MOR of nano-ZrO₂ and YSZ reinforced binding systems of SFC-1 as a function of the firing temperatures.

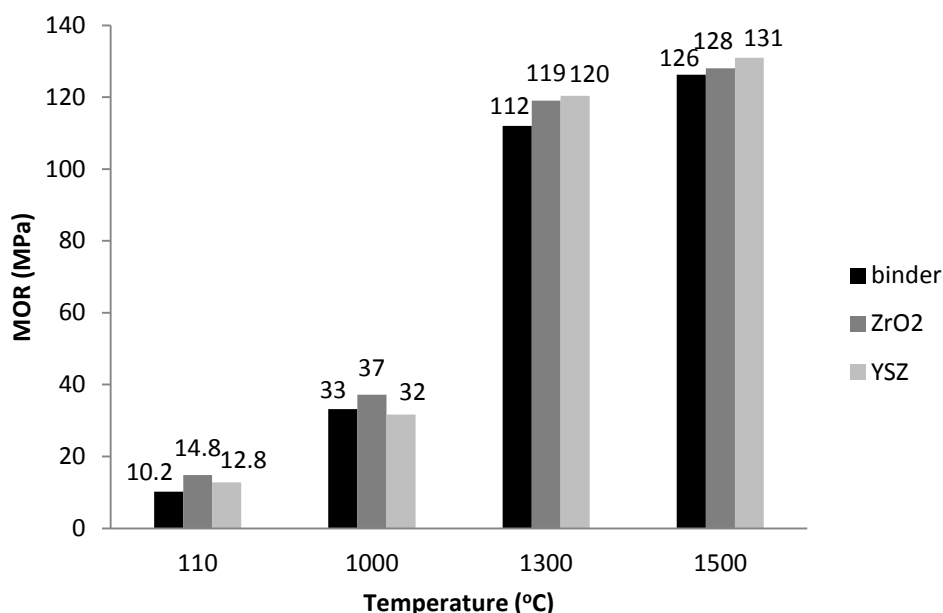


Figure 4.96 MOR of binding system of SFC-1 as a function of elevated temperature.

The addition of nano-ZrO₂ and YSZ gradually increases the MOR of binding systems compared to non-reinforced samples but there was no significant improvement in the MOR of samples. Notice that the MOR of nano-ZrO₂ and YSZ reinforced and non-reinforced SFC-1 steadily increases at elevated temperatures.

4. 15 Effect of Yttria Distribution of Nano-ZrO₂ Reinforced Refractory Castables

Yttria distribution in nano zirconia has a strong effect on the stabilization of the tetragonal phase at the service temperatures so it influences both, the K_{IC} and the MOR of the samples. In order to investigate the effect of yttria distribution, 8Y-ZrO₂ was mixed with undoped ZrO₂ to obtain overall yttria content of 1, 2 and 3 mol-%. Figure 4.97 shows the MOR of binding system of SFC-3 as a function of firing temperatures. Notice that 3%C-YSZ refers to 3%YSZ in the as received condition.

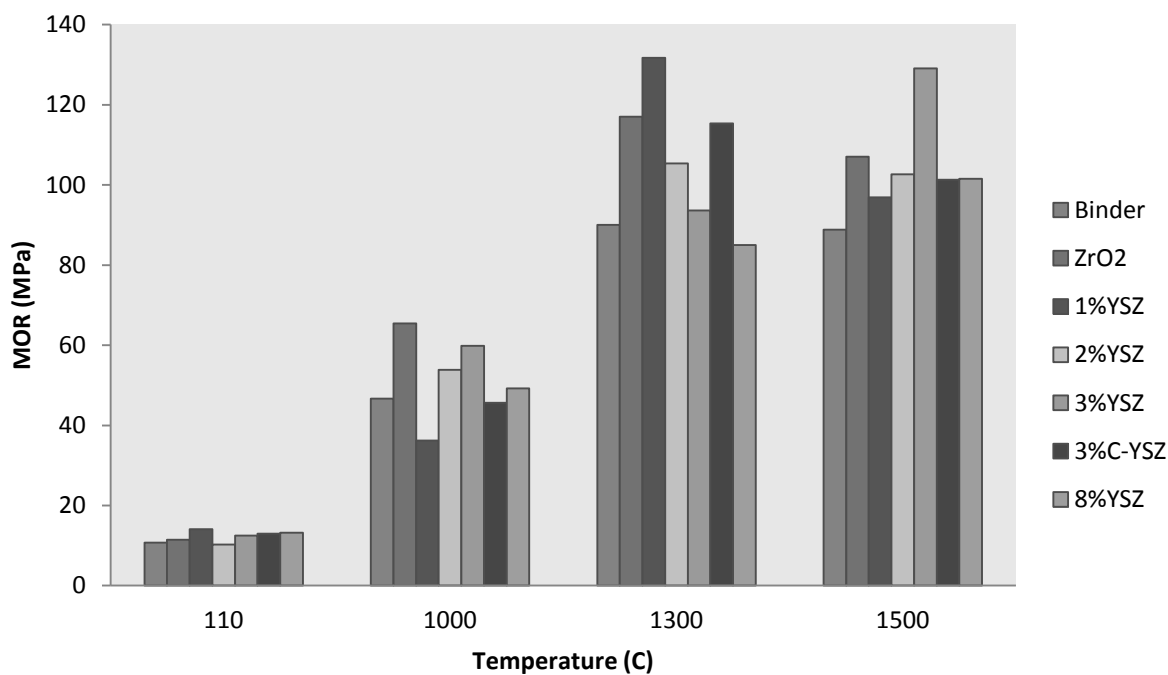


Figure 4.97 MOR of binding system of SFC-3 at elevated temperatures as a function of yttria distribution

Results show that the addition of nano-ZrO₂ increases the MOR steadily at elevated temperatures. After drying at 110°C, there is no significant difference in the MOR of the samples. At 1000°C, the addition of undoped nano-ZrO₂ shows the highest MOR values at 65.4±3.36 MPa. At 1300°C, the most significant increase was observed in the MOR with addition of 1Y-ZrO₂ from 36.7 MPa at 1000°C to 131.7 MPa at 1300°C, this is followed by undoped-ZrO₂. After firing at 1500°C, the addition of 3Y-ZrO₂ shows the highest MOR at 129.1 MPa compared with the other SFCs.

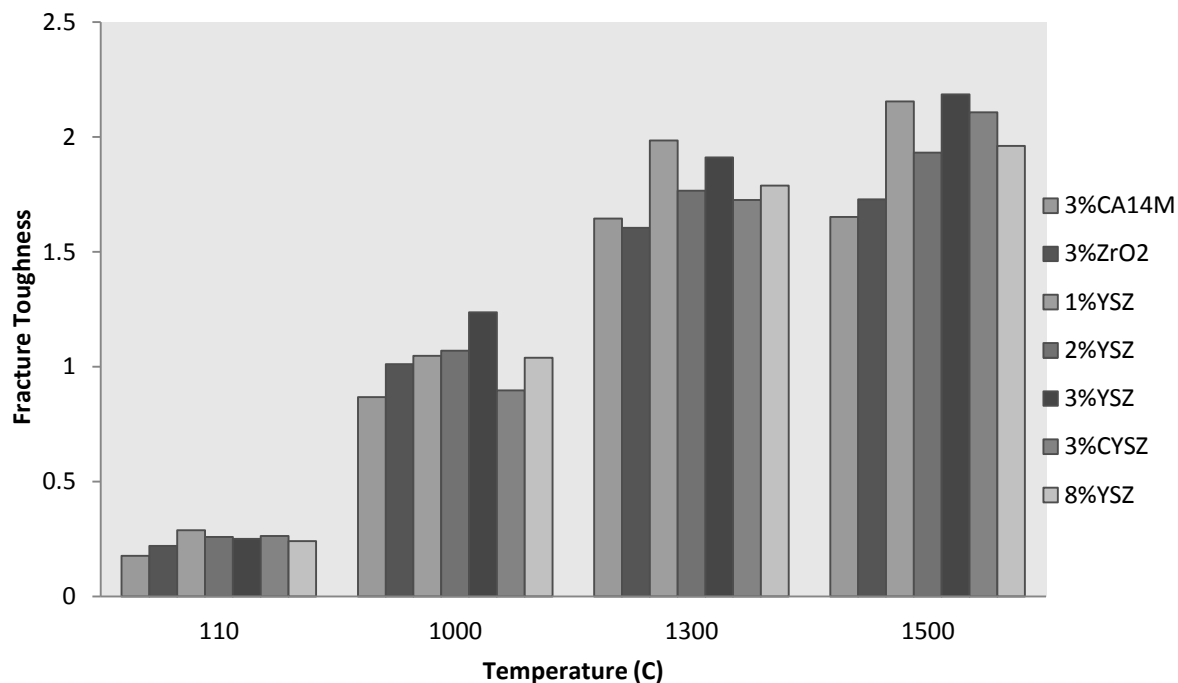


Figure 4.98 Fracture toughness of binding systems of SFC-3 as a function of firing temperature.

The K_{IC} (fracture toughness) of binding system of SFC-3 as a function of firing temperatures is illustrated in Figure 4.98. K_{IC} values of all samples steadily increase at elevated temperatures as seen figure. Although the addition of nano- ZrO_2 gradually increases the K_{IC} of the binding systems, there was no promising improvement seen in these samples. In general, the addition of 3Y- ZrO_2 increases the K_{IC} of the binding systems slightly when compared with the other samples at elevated temperatures.

4.16 Effect of Drying on Modulus of Rupture of Binding System

In order to measure the effect of drying on the MOR of SFCs, two groups of samples were prepared after de-molded. The first group of samples was dried at 110°C for 24 hour while the others were not. Finally, the MOR of both dried and non-dried samples were

measured as a function of time 1th, 7th and 28th day, respectively using three point bending testing. Figures 4.99(a-c) show the drying effect on the MOR of the binding systems of SFCs as a function of time.

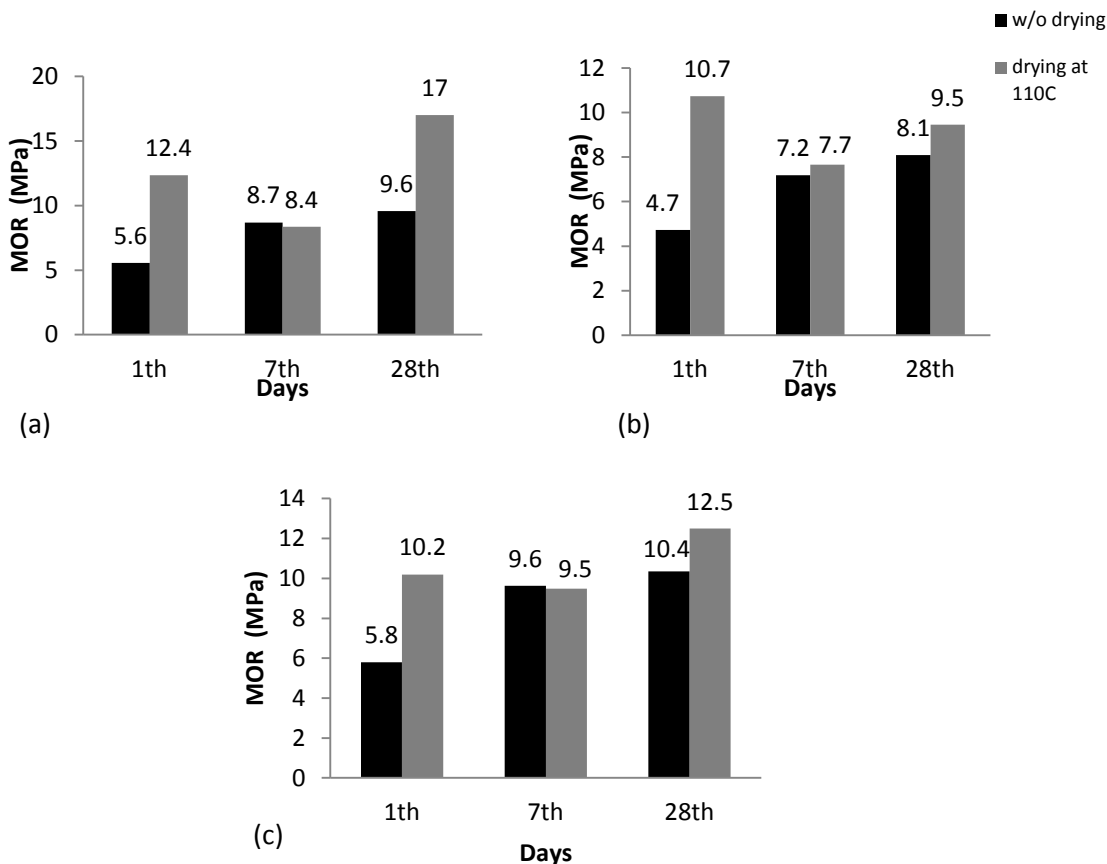


Figure 4.99 Drying effect of the MOR of binding system of (a) SFC-5, (b) SFC-3 and (c) SFC-1 as a function of time

After the 1th day, the MOR of non-dried samples is lower than the samples dried at 110°C. That is explained by the free water present in non-dried samples degrading the physical properties of castables. After the 7th day, the MOR values of non-dried sample increased with decrease in their free water content with time i.e., getting lighter. On the other hand, the MOR values of dried samples decreased because of humidity coming from air i.e., the samples gained weight. After the 28th day, the MOR values of both non-dried and dried samples increased due to the drying effect (i.e., the both samples were

getting lighter). Consequently, the MOR of non-dried samples steadily increases with drying time due to losing their free water. On the other hand, the MOR of dried samples decreases after the 7th day due to humidity from the air (i.e, gaining weight) and then increases again due to drying becoming the dominant effect. Notice that the drying step of castables is very crucial for both mechanical and physical properties. There is a significant difference between dried and non-dried samples respect to the MOR values after the 1st day since free water in non-dried samples degrades to mechanical properties of samples. Drying at 110°C is needed to remove all superficial and free water. This also fully converts any metastable phases (CAH_{10} and C_2AH_8) into cubic hydrates and crystalline gibbsite, and provides higher strength development for the binder/aggregate system cured 24 hours at higher temperatures. Although the MOR of non-dried samples increases with time, it doesn't reach the same value comparing to dried samples, indicating that drying of castables is necessary to improve the strength of samples. In addition, elimination of free water from samples with drying at 110°C permits to fire up the samples at elevated temperatures because free water in the samples can lead to the development of cracks or fracture at elevated temperatures.

4.17 Microstructural Investigation of Fracture Surfaces

It is critical to be able to correlate the evolution of thermo-mechanical properties of castables with the microstructural evolution of the binding system. This, in order to better understand the initial stages formation of the ceramic bond and how it affects the fracture toughness of self-flow castables (SFCs). Scanning electron microscopy (SEM) was used to evaluate the resultant microstructures of SFCs. Figures 4.100(a-c) show SEM

pictures and EDS pattern of fracture surface of SFCs at dried 110°C for 24 hours. Fracture took place at the binding system as indicated by the EDS pattern in figure 4.100(c).

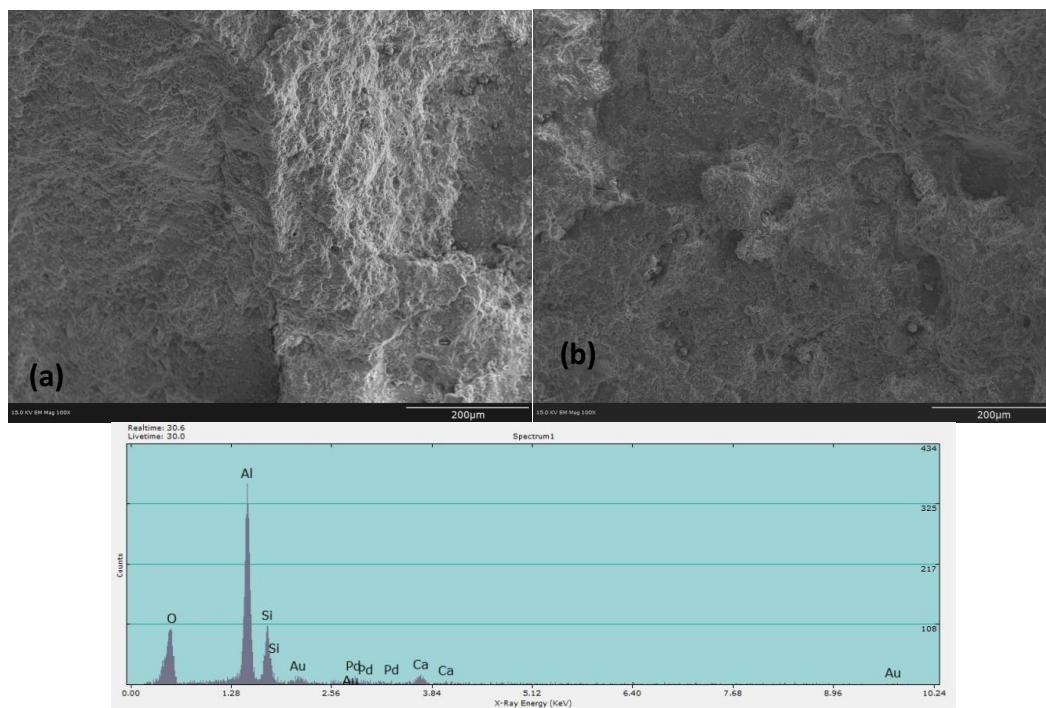


Figure 4.100 (a) and (b) Fracture surface of SFC-5 and SFC-3 at 110°C for 24 hours respectively and (c) EDS pattern of fracture surface of SFC-5 sample at 100X.

As seen from this figure, the EDS pattern shows Al, Si, Ca and O elemental peaks, corresponding to the composition of matrix system. At 110°C, fracture occurred on the binding system since the ceramic bond has not been developed yet and corundum aggregate. The fracture surface is flat and smooth, indicating the brittle fracture behavior, thus confirming the fracture toughness results. As seen in Figure 4.101(a), the aggregates debonded from the matrix since the ceramic bonding hasn't developed yet after drying at 110°C for 24h. Figure 4.101(b) is an SEM picture of a debonded aggregate, indicating the weak bonding between aggregate and the binding system. Figure 4.101(c) shows the porosity and the formation of cracks around the porosity.

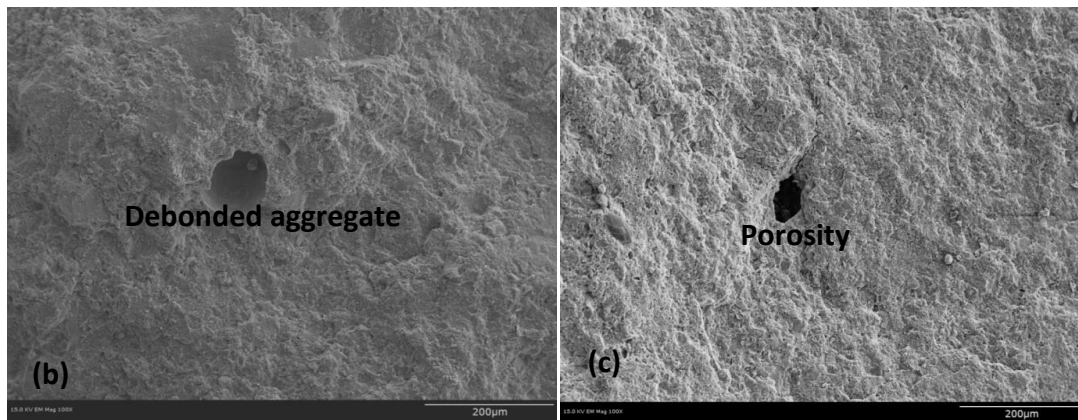
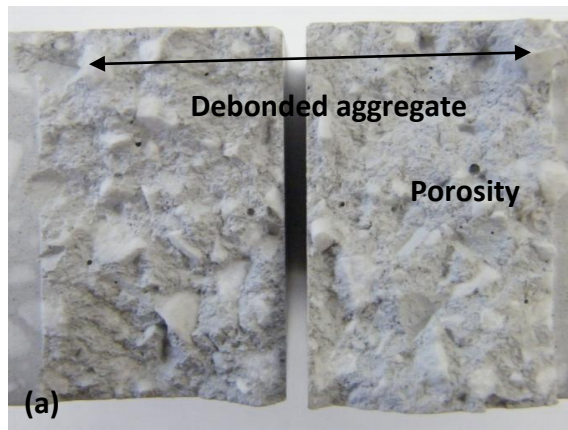


Figure 4.101 (a) Fracture surface of SFC-5 dried at 110°C for 24h (b) and (c) SEM pictures of SFC-5 at 100X

Ceramics are porous materials and this is one of the reasons why they are brittle. Porosity is a common flaw in brittle materials. As seen from Figures 4.102, castables have different size and shapes of pores, leading to brittle fracture.

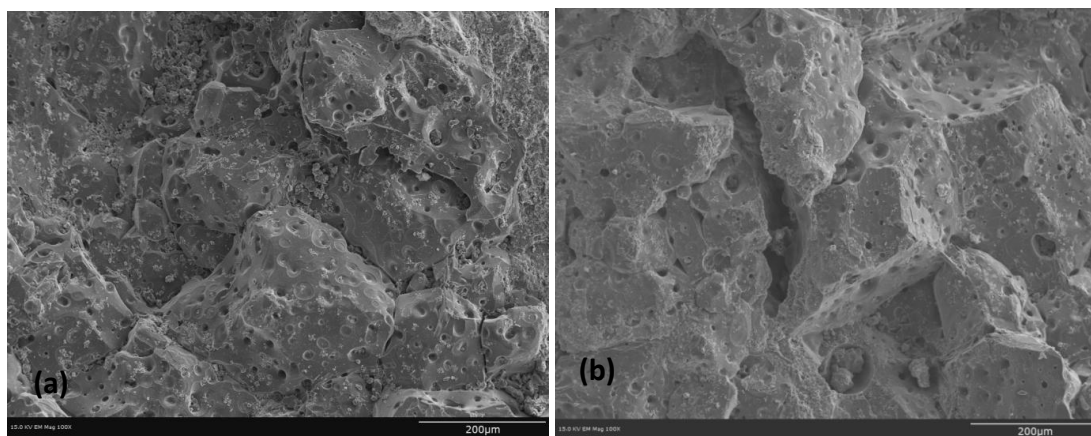


Figure 4.102 Fracture surfaces of (a)SFC-5 and (b)SFC-3 after drying at 110°C for 24 h at 100X

The properties of the castables changed at elevated temperatures due the development of ceramic bonding. As seen Figure 4.103(a) and (b), the fracture surface of a SFC-5 sample after firing at 1000°C shows that fracture evolves through both, the binding system and the alumina aggregate through the development of a ceramic bonding as confirmed by the EDS pattern in Figure 4.104(a-b).

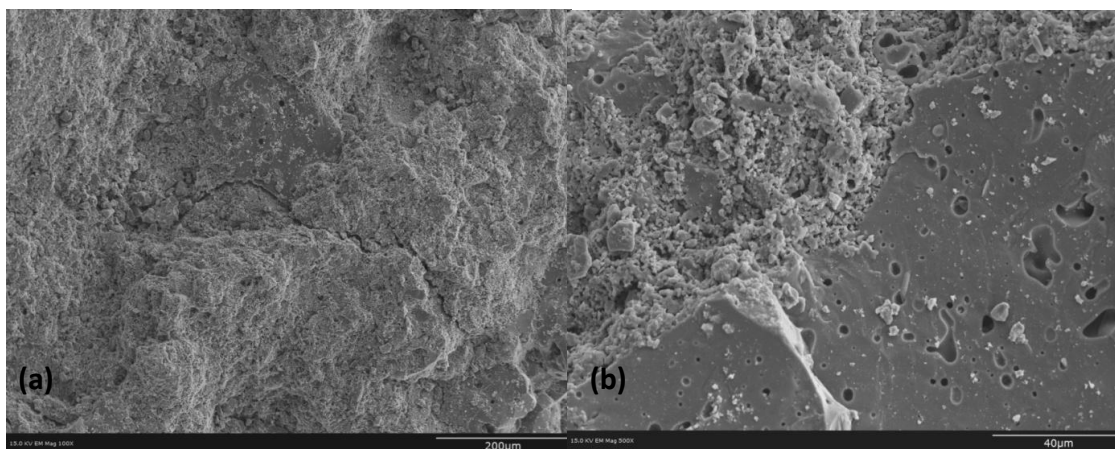


Figure 4.103 Fracture surface of SFC-5 (a) at 100X and (b) at 500X after firing at 1000°C for 3h

As seen in Figure 4.104(a) and (b), the fracture surface is getting rough with the development of ceramic bonding at elevated temperatures. Figure 4.104(a-b) shows the elemental composition of binding system and aggregate respectively, indicating fracture

of the aggregate after firing at 1000°C in SFC-5 as bonding is developed. Notice that the fracture toughness results of SFC-5 show an increase after firing at 1000°C in SFC-5 as seen Figure 4.75.

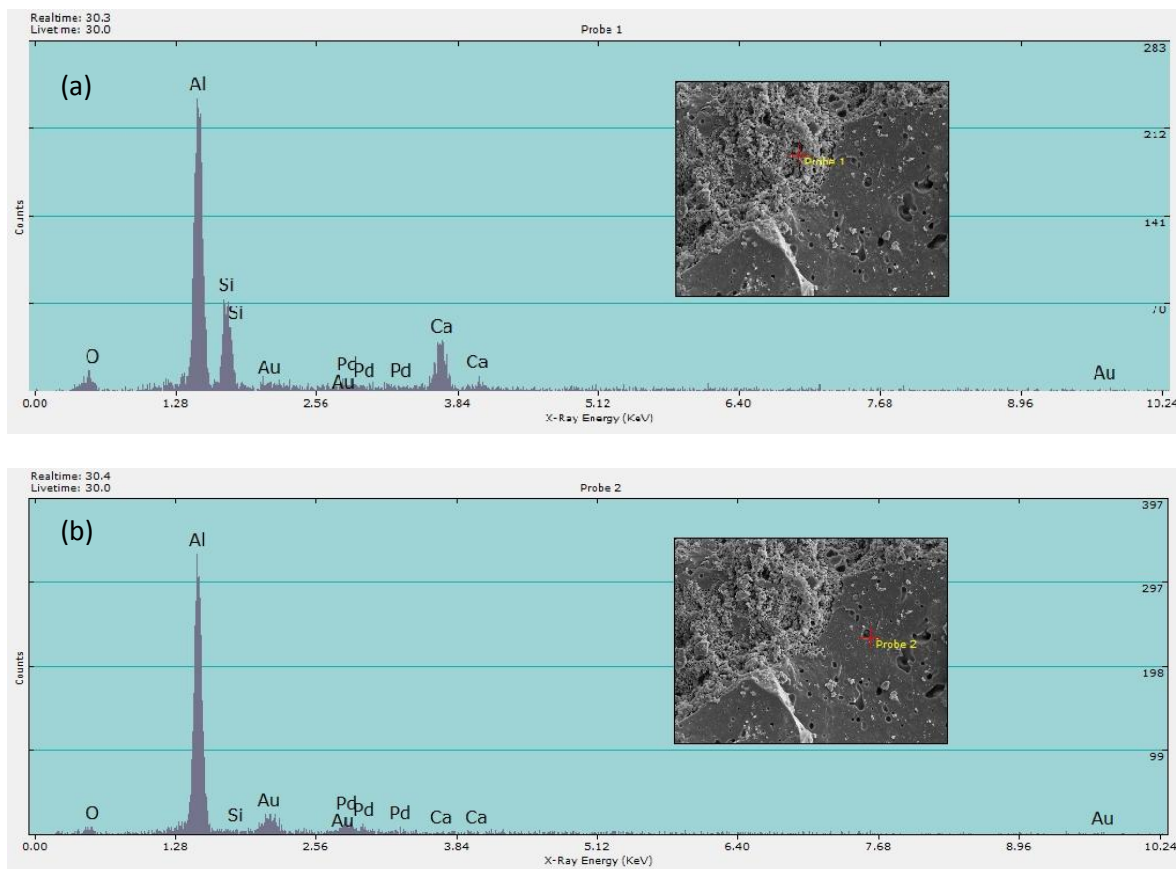


Figure 4. 104 (a) and (b) EDS patterns of SFC-5 sample after firing at 1000°C for 3h.

Figure 4.105(a) and (b) show the fracture surface of SFC-3 and SFC-1 at 1000°C respectively. The fracture surface is getting smoother with a decrease in the cement content from 3% to 1% in castables. Since the ceramic bonding has not been developed in SFC-1 at 1000°C (EDX results, Figure 4.63) as confirmed by the fracture toughness results. Notice that the fracture surface of SFC-5 is rougher than in either the SFC-3 or SFC-1 after firing at 1000°C as seen Figure 4.103(a-b). This is attributed to the early development of ceramic bonding with a higher cement content.

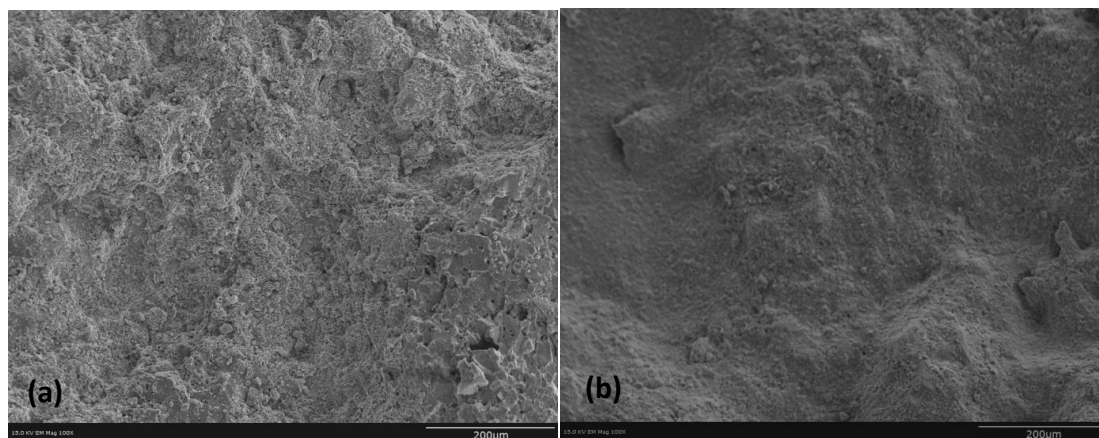


Figure 4.105 Fracture surface of (a) SFC-3 and (b) SFC-1 after firing at 1000°C for 3h at 100X

As seen figure 4.106(a) and (b), there is a crack observed at the interface between alumina aggregate and binder with firing temperature. These cracks are attributed to thermal expansion mismatch between the alumina aggregate and the new phases formed such as anorthite, cristobalite and mullite at elevated temperatures.

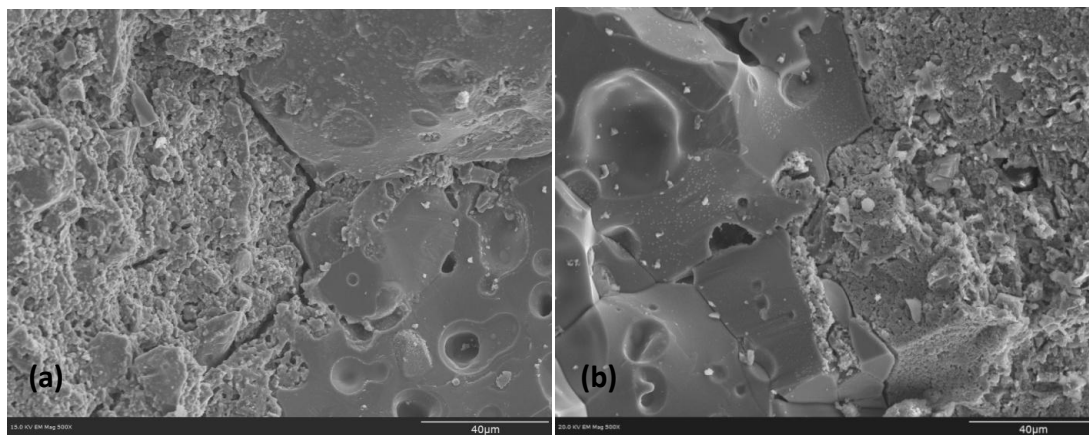


Figure 4.106 Fracture surfaces of (a) SFC-5 and (b) SFC-1 after firing at 1300°C for 3h at 500X.

Notice also that cracks increase as a result of increasing thermal expansion mismatch with increased cement content due to the formation of anorthite phase. Figure 4.107(a-d) shows the fracture surfaces of SFC-5 and SFC-1 respectively after firing at 1500°C for 3h. As seen from these figures, the formation of cracks is noticeably higher in SFC-5

compared to SFC-1. This is explained by the formation of the low melting phase (anorthite) in SFC-5 due to increasing cement content. These cracks are attributed to thermal expansion mismatch between alumina aggregate and phases formed such as anorthite, cristobalite and mullite at elevated temperatures.

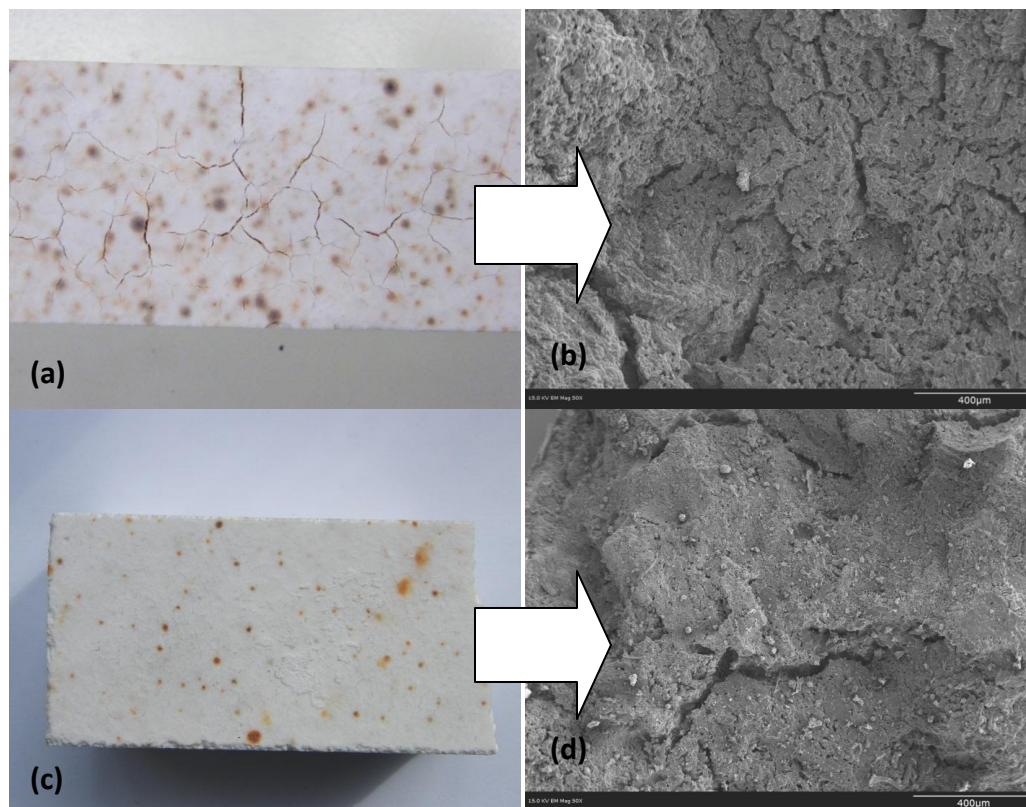


Figure 4.107 (a) Fracture surface of SFC-5 and (b) SEM picture of SFC-5 at 50X (c) fracture surface of SFC-1 and (d) SEM picture of SFC-1 at 50X after firing at 1500°C for 3h

Figures 4.108(a) and (b) show fracture surfaces of SFC-1 and SFC-5 after firing at 1300°C consisting of surface flaws, agglomerated particles and spherical porosities in the microstructure, indicating processing defects causing the brittle fracture in the castables.

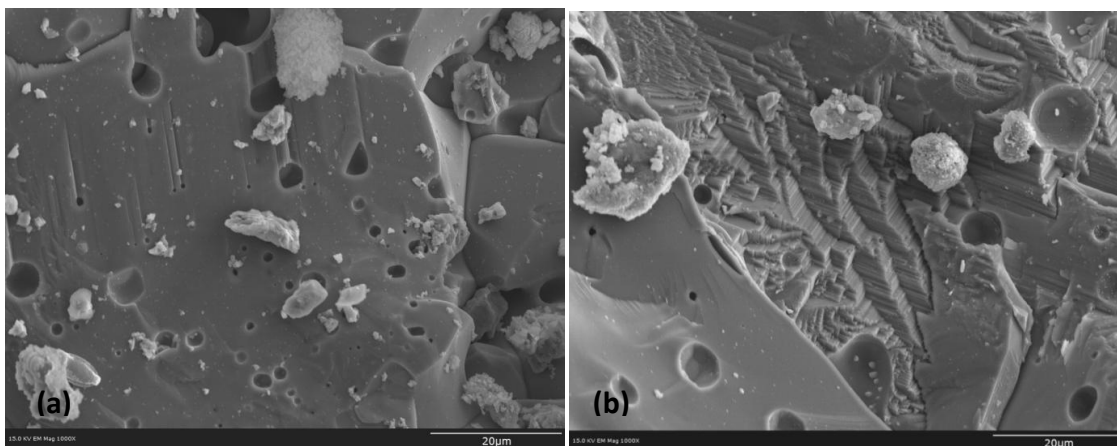


Figure 4.108 Fracture surfaces of (a) SFC-1 and (b) SFC-5 after firing at 1300°C for 3h at 1000X.

Internal pores are the common failure origins in the brittle materials. As seen Figure 4.109(a) and (b), different sizes and shapes of internal pores are the leading failure origins in castables.

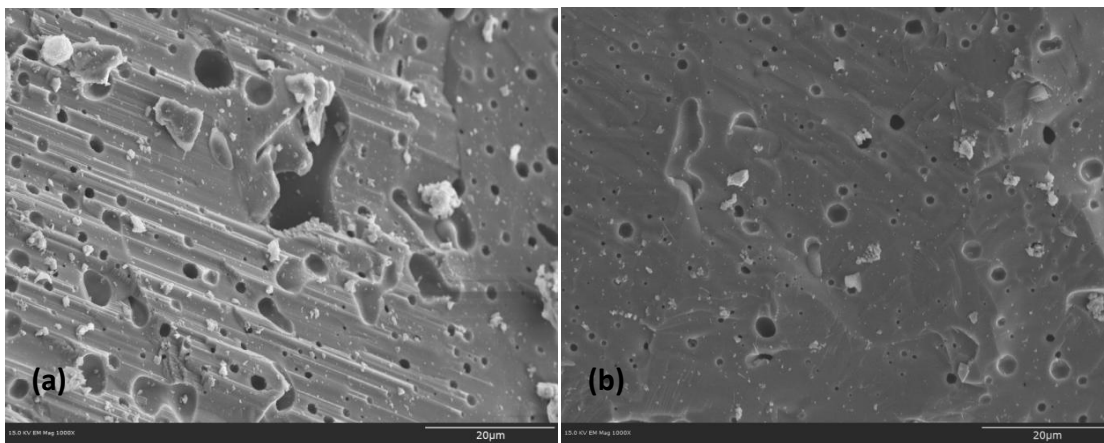


Figure 4.109 Fracture surfaces of (a) SFC-1 and (b) SFC-3 after firing at 1500°C for 3h at 1000X

Surface flaws are another common failure origin in brittle materials in addition to porosities. Figures 4.110(a) and (b) show both, surface flaws (columnar shape) and circular internal pores, leading to brittle fracture in castables.

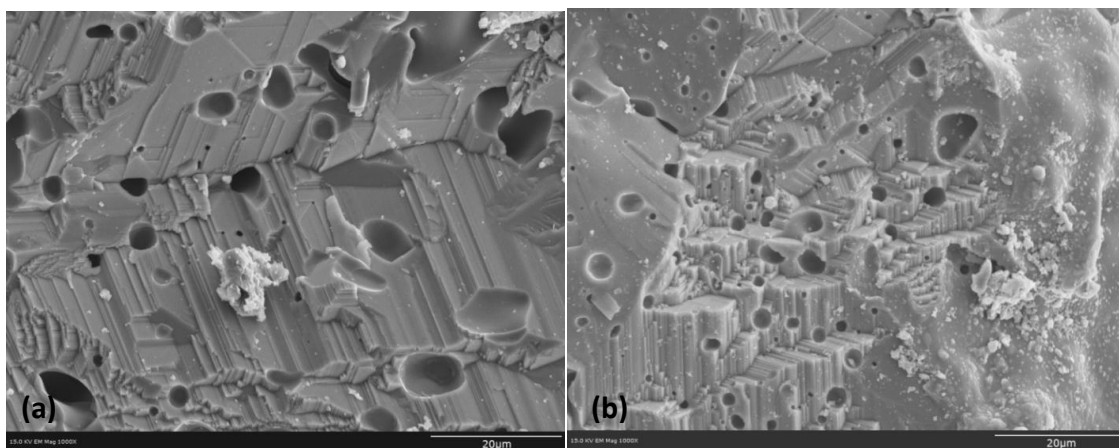


Figure 4.110 Fracture surfaces of (a) SFC-5 and (b) SFC-3 after firing at 1300°C for 3h at 1000X

Surface flaws can be seen in figures 4.11(a) and (b) more clearly. These flaws act like failure origins in refractory castables.

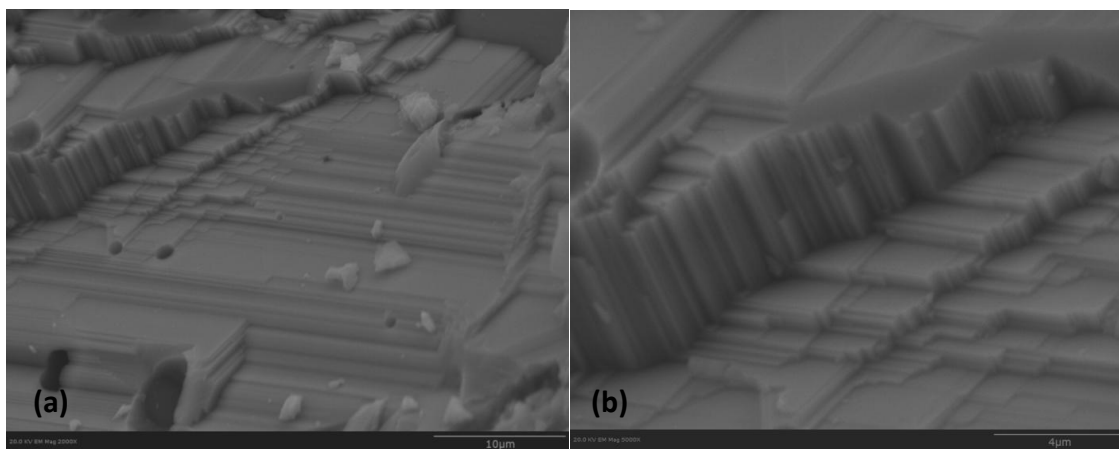


Figure 4.111 Fracture surface of SFC-3 (a) at 2000X and (b) at 5000X after firing at 1300°C for 3h.

A fractographic investigation of the experimental refractories provide valuable information on the fracture behavior of SFCs at elevated temperatures. The mechanical property studies of refractories demonstrated that fracture toughness of the SFCs as well as MOR and CCS increase at elevated temperatures due to ceramic bonding development. SEM confirms the results obtained from mechanical studies. In general,

the fracture surfaces of the SFCs are smooth and flat at 110°C due to hydraulic bonding, indication of brittle fracture behavior since ceramic bonding has not developed at this temperature. There is still no strong bonding between the aggregate and the binding system. Hence, aggregates debonded, causing to voids in the matrix as seen SEM figures. At 1000°C, ceramic bonding is developed at SFC-5 and SFC-3 samples due to high cement contents. As a result, the fracture in both, samples evolved through either the alumina aggregate or the binding system since ceramic bonding becomes stronger in the binding system than in the aggregate. On the other hand, the fracture surface of SFC-1 at 1000°C is still smooth and flat similar to 110°C (figure), showing a low toughness behavior since 1 wt.% cement content is not enough to develop a ceramic bonding at 1000°C as confirmed by XRD pattern in figure. At 1300°C and 1500°C, the fracture surface of SFC-1 gets rough with the development of the ceramic bonding. This is confirmed by XRD pattern showing crystallization of cristobalite at 1300°C and mullite phase at 1500°C in figure 4.62 and 4.63 respectively. A formation of cracks was observed in the SFCs at elevated temperatures due to thermal expansion mismatch between alumina aggregate and the formation of new phases such as; anorthite, cristobalite and mullite. These cracks increased with increased cement content due to the formation of the low melting phase (anorthite). SEM micrographs also show common flaws like internal pores and surface flaws in castables, acting failure origins and causing the brittle fracture.

CHAPTER 5- CONCLUSION

Based on both, the experimental and analytical work, the following conclusions can be summarized as:

- LCC and ULCCs compositions designed according to Andreassen model with a q (Andreassen distribution coefficient) value of 0.25 provides good self-flow properties in castables. A 5.5% water addition is satisfactory to achieve self flowing performance. The results show that the self flow value decreased from 150% to 140% when the cement content was reduced from 5% to 1% with an increment in the hydratable alumina content to 3%. This is attributed to the fact that hydratable alumina needs additional water in order to set the castables. Moreover, the self-flow values shift from 10% to 30% when nano-ZrO₂/YSZ additions increases from 1 to 5%.
- XRD studies of the castable samples fired to 110°C for 24h revealed corundum (Al₂O₃) phase. With increasing firing temperatures through 1000°C for 3h, the anorthite phase was detected in SFC-5 sample. In contrast, there was no new phases detected in the both SFC-3 and SFC-1 samples. This indicates that higher cement can lead the early development of ceramic bonding at lower temperatures when compared with hydratable alumina. At 1300°C for 3h, cristobalite and anorthite phases were detected in SFC-1 and SFC-3 samples respectively. There are no new phases detected in SFC-5, other than an increased peak intensity of the anorthite phase. In the castable samples fired at 1500°C for 3h, the formation of the mullite phase was detected, but the XRD peak intensity was decreased with

increased cement content. This is attributed to cement attack of the mullite phase inhibiting its formation.

- An increase in the firing temperature from 110°C to 1500°C leads to an increase in the BD of castables depending on the cement content. The SFC-5 sample showed the highest densification behavior compared to SFC-3 and SFC-1 since hydratable alumina does not relieve chemically bonded water easily due to its gel structure. The WA of the castables exhibits a similar trend as the AP as a function of the firing temperature. WA increases at 1000°C because of an increase in AP, then decreases at 1500°C, indicating the densification process in the SFCs. The WL of the castables confirms the BD results. At 110°C for 24 h, it shows the highest WL due to the removal of free water from the castables. With increasing firing temperatures through 1500°C for 3h, the WL of castables decreases except for the SFC-1 sample since it has a higher hydratable alumina (3%). As mentioned above, it takes time to relieve chemically bonded water for hydratable alumina due to its gel structure so the SFC-1 sample still shows an increase in WL at 1500°C.
- The TGA results on the castables confirm the WL of the castables. The castables showed WL at elevated temperatures. In particular, there is a characteristic drop in the temperature range between 200-300°C due to dehydration of hydrated cement of AH_3 and C_3AH_6 . In addition, WL of SFC-5 was higher than in both SFC-3 and SFC-1 samples up to 1000°C since they do not contain any hydratable

alumina. The DTA results of the castables indicate an endothermic reaction at a temperature between 200-300°C due to dehydration of the hydrated products.

- The PSD of nano-ZrO₂ particles was 1782 nm without any additives and ultrasonification. ZP is 24.24 corresponding to a pH of 7.52. After 20 minutes of ultrasound mixing with the additive of D811, the PSD of the nano-ZrO₂ particles was 8.9 nm. The corresponding ZP is -56.64 and the pH increases from 7.52 to 9. When nano-ZrO₂ particles were mixed with the additive of M-ADS/M-ADW after 20 minutes of ultrasound mixing, the PSD was 17.7 nm. The ZP is -62.33 and the pH decreases to 5.76. These results show that ultrasonification and additives (D-811 and M-ADS/MAD-W) enhance the PSD through its effect on negatively charging the nano-ZrO₂ particles.
- Up to 1000°C, the highest values of CCS were obtained in the SFC-5 samples due to the early development of ceramic bonding with a higher amount of cement content. After firing at 1500°C, both SFC-3 and SFC-1 samples show a promising increase in the CCS through the development of ceramic bonding. In contrast, the CCS of SFC-5 decreases due to an increase in the amount of anorthite (low melting phase).
- The K_{IC} and MOR results of the castables show similar trends. Up to 1000°C, the SFC-5 samples show the highest MOR and K_{IC} through the development of ceramic bonding. After firing at 1300°C, SFC-3 and SFC-1 show significant improvements in the K_{IC} and MOR. In contrast, the K_{IC} and MOR of SFC-5

decrease due to the increase in the amount of anorthite. With increasing firing temperatures, up to 1500°C, there is a gradual increase in the MOR and K_{IC} of SFC-3 and SFC-1 samples. In contrast, the MOR and K_{IC} of SFC-5 shows a promising increase due to a reduction in the amount of anorthite through the conversion of the mullite phase.

- The indentation toughness results are much higher than the K_{IC} results of castables due to size difference effects. The discrepancy in the toughness results can be explained by various reasons such as; (a) Using the Berkovich and vickers indenters instead of a cube corner causes uneven results since the cube corner is sharper than the Berkovich and creates more linear cracks, (b) During the indentation test, the selected area is also an important factor in getting more accurate results. Selecting an aggregate instead of the binder gives rise to much higher results since the aggregates have a high hardness and a high elastic modulus. Generally, aggregates are more visible than the binders the optical microscope . In Contrast, the binder phase is usually blurry and it is difficult to measure its inherent hardness.
- The effect of nano-ZrO₂/YSZ particles on the exhibited MOR and K_{IC} values is investigated in the experimental castables. XRD results show that nano ZrO₂ and YSZ particles are monoclinic and cubic respectively. The MOR of castables is improved by approximately 20% with the addition of 3% ZrO₂. This is attributed to the stabilization of tetragonal ZrO₂ at room temperature. In contrast, there are no noticeably changes in the MOR of castables when nano-YSZ ws added.

Apparently, the stabilization of tetragonal-ZrO₂ does not take place in this case. There are no significant effects of the additions of nano-ZrO₂/YSZ on the exhibited K_{IC} of the castables.

- The binder systems of the castables show similar results to the matrix systems of the castables. Up to 1000°C, the binder system of SFC-5 shows the highest MOR and the K_{IC} due to the development of a ceramic bonding. After firing at 1500°C, SFC-3 and SFC-1 samples show a promising increase in the MOR and K_{IC} with the formation of the ceramic bond. It is also important to mention that there are no cracks formation observed in the binding systems of samples after firing up to 1500°C. Crack formation is attributed to thermal expansion differences between aggregate and the phases developed (anorthite, cristobalite and mullite) at elevated temperatures. As a result, there is no characteristic drop observed in the MOR results of castables after firing at 1500°C.
- The effect of nano-ZrO₂/YSZ particles on the exhibited MOR in the binder systems of the castables. The results show that the MOR of binder systems is improved with the addition of the both nano-ZrO₂/YSZ at elevated temperatures. In addition, the effect of the yttria distribution is investigated in terms of the MOR and K_{IC} of binder systems of SFC-3 samples. The yttria distribution has a strong effect on the stabilization of tetragonal zirconia at the service temperatures. Also, there is a significant improvement in the observed MOR of the binder system for the SFC-3 samples with addition of different yttria content in the nano-ZrO₂

particles. In contrast, there is a gradual increase observed in the K_{IC} of the binder system of SFC-3.

- The drying step at 110°C for 24h is crucial for castables due to the removal of free water and for the increasing strength development between the aggregate/binder system. The results show that the dried samples possess a higher strength than the non-dried samples. On the other hand, the strength of non-dried samples increases with the drying time but they do not reach the strength of dried samples.
- An investigation of the fracture surfaces of castables is necessary to understand the evolution of thermal stresses. SEM pictures show that all the castables have flat and smooth fracture surfaces after firing at 110°C, indicating brittle fracture behavior. In addition, debonded aggregates are observed on the fracture surfaces of castables since there is no strong bonding between aggregates and the binding system. With increasing firing temperature through 1000°C, the fracture surfaces of SFC-5 and SFC-3 samples evolve through the binding system and aggregate due to the development of ceramic bonding. After firing at 1300°C, fracture surfaces of all castables are getting rougher with the development of ceramic bonding. The number of fractured aggregates increases at elevated temperatures, indicating the development of a strong ceramic bonding between aggregate and the binding system. In addition, fractography studies give valuable information about the common failure origins in brittle materials. The studies show that internal pores and surface flaws are common failure origins, causing brittle fracture in the castables.

CHAPTER 6- FUTURE WORK

From the present work various research activities are recommended for further study on self flowing castables

- In order to identify the variables affecting the control setting time, zero cement castables can be studied with using different additives and binders.
- Indentation toughness of castables can be further studied using cube corner indenter in addition to the Vickers and Berkovich indenters.
- Additions of nano-ZrO₂/YSZ can be increased beyond 5 % to investigate their effect on the modulus of rupture (MOR) and fracture toughness (K_{IC}) of castables.
- In this study, physico-mechanical properties of castables were studied in terms of cold crushing strength (CCS), modulus of rupture (MOR) and fracture toughness (K_{IC}). These properties can be measured at service temperatures since the applications of castables are typically at elevated temperatures (>1000°C).
- The effect of nano ZrO₂/YSZ addition on physico-mechanical properties of castables can be further investigated in the temperature range between 1200-1500°C where ZrO₂ has a tetragonal structure (1170-2370°C).

REFERENCES

1. Charles A. Schacht, "Refractories Handbook", Marcel Dekker, Inc., New York-Basel, 2004
2. W. E. Lee, W. Vieira, S. Zhang, K. Ghanbari Ahari, H. Sarpoolaky, and C. Parr, "Castable refractory concretes", International Materials Reviews, Vol. 46, No. 46, (2001), pp. 145-16
3. Paulo Cesar Evangelista, Christopher Parr, Catherine Revais, "Control of formulation and optimization of self-slow castables based on pure calcium aluminate", Refractories Applications and New, Vol. 7, (2002), pp. 14-18
4. Walter C. Wedberg, Eldar Dingsoyr and Magne Dastol "Particle size and particle size distribution of elkem microsilica and its relevance to technical application", Presented at 5th European Symposium Particle Characterization, Nurnberg, Germany, 24-26 March 1992
5. Bjorn Myhre "Particle size distribution and it relevance in refractory castables" India International Refractory Congress 1996, New Dehli 8th and 9th February 1996
6. Bjorn Myhre, Bjorn Sandberg and Aase M. Hundere, "Flow and flow decay of refractory castables", Presented at the 3rd India International Refractories Congress, Elkem Refractories, 1998
7. Bjorn Myhre and Katinka Sunde, "Alumina based castables with very low contents of hydraulic compound part 1", Presented at UNITECR 95, Elkem Refractories, 1995
8. Bjorn Sandberg and Bjorn Myhre, "Microsilica: A versatile refractory raw material", Presented at the Indian Refractories Congress, 1994
9. Bjorn Myhre and Bjorn Sandbergh, "The use of microsilica in refractory castables" Elkem ASA Materials.
10. C. Gogtas, N. Unlu, A. Odabas, L. Sezer, F. Cinar, S. Guner, G. Goller and N. Eruslu, "Preperation and characterization self flowing refractory materilas containing 971U type microsilica", Advanced in Applied Ceramics, 2009
11. C. Gogtas, N. Unlu, A. Odabasi, L. Sezer, F. Cinar, S. Guner, and N. Eruslu, "Characterization of the physical properties of a self-flowing low-cement castable

- based on white-fused alumina” Journal of Ceramics Processing Research, Vol. 9, No. 5, (2008), pp. 1-7
12. C. Gogtas, A. Odabasi L.Sezer, F. Cinar, S. Guner, N. Eruslu and N. Unlu, “Improvement of properties of self-flowing low-cement castables based on brown fused alumina”, Journal of Ceramics Processing Research, Vol. 8, No. 5, (2007), pp. 324-33
 13. C. Gogtas, N. Unlu A. Odabasi L.Sezer, S. Guner, G. Goller and N. Eruslu, “Effects of firing temperature on the physical properties of a bauxite based refractory castables” Refractories and Industrial Ceramics, Vol. 53, No. 1, 2012
 14. Xianxin Zhou, K. Sankaranarayanan, Michel Rigaud, “ Design of bauxite-based low cement pumpable castables : a rheological approach”, Ceramics International, Vol. 30 (2004), pp.47-55
 15. A.R. Studart, V.C. Pandolfelli, E. Tervoort, L.J. Gauckler, “Selection of dispersants for high-alumina zero-cement refractory castables”, Journal of the European Ceramic Society, Vol. 23 (2003), pp. 997-1004
 16. M.A. Serry, M.F. Zawrah, and N.M. Khalil “ Bauxite based low and ultralow cement castables”, British Ceramic Transactions, Vol. 101, pp. 165-168
 17. Sasan Otroj, Mohammad Ali Bahrevar, Fatollah Mostarzadeh, Mohammad Reza Nilforoshan, “The effect of deflocculants on the self-flow characteristics of ultra low-cement castables in Al_2O_3 -SiC-C system”, Ceramics international, Vol. 31, (2005), pp. 647-653
 18. Xianxin Zhou, K. Sankaranarayanan, Michel Rigaud, “Design of bauxite low-cement pumpable castables: a rheological approach”, Ceramics International 30, pp. 47-55,2004
 19. Fangbao Ye, Mi Rigaud, Xinhong Liu, Xiangchong Zhong, “High temperature mechanical properties of bauxite-based SiC-containing castables” Ceramics International 30, pp. 801-805, 2004
 20. P. Korgul, D.R. Wilson and W.E. Lee, “Microstructural analysis of corroded alumina-spinel castable refractories”, Journal of the European Society 17, pp 77-84, 1997

21. Swe-Kai Chen, Min-Yuan Cheng, Su-Jien Lin, Yung-Chao Ko “Thermal characteristics of $\text{Al}_2\text{O}_3\text{-MgO}$ and $\text{Al}_2\text{O}_3\text{-spinel}$ castables for steel ladles”, *Ceramics International* 28, pp. 811-817, 2002
22. Vicki Jones, Gerrards Cross, “Rheology control of low-cement self-flow castables” *Ceramics Industry*, pp. 49, Feb 1998
23. David J. Green, “An introduction to mechanical properties of ceramics”, 1998
24. B. Basu, “Toughening yttria-stabilised tetragonal zirconia ceramics”, *International Materials Review*, Vol. 50, No. 4, (2005), pp. 239-256
25. M. Yoshimura, “ Phase Stability of Zirconia”, *American Ceramic Society Bulletin*, Vol. 67, Issue:12 (1988), pp. 1950-1955 REF 47
26. L. Gao, T.S. Yen, J.K.Guo, “ Influence of ZrO_2 particle size on toughening in hot-pressed Y-TZP”, *Advanced in Ceramics*, Vol. 24: Science and Technology of Zirconia III, (1988), pp. 405-414, REF. 102
27. Aase Hundere, Bjorn Myhre and Bjorn Sandberg, “ Free-flowing castables-a prerequisite for wet-gunning of refractory castables”, Presented at VII-th International Metallurgical Conference in Ustron, Poland.” May, 1997
28. Charles Alt, Lana Wong and Chirostopher Parr, “ Measuring castable rheology by exothermic profile” *Refractories Applications and News*, Volume 8, No:2, 2003
29. F. Goetz Neunhoeffler, “ Hydration kinetics of calcium aluminate cement with calcium sulfate hemihydrate in presence Ti^+ and tartaric acid” Department of Mineralogy, University of Erlangen-Nuremberg-Germany
30. Zeta Meter Inc, “ Zeta potential complete course in 5 minutes”
31. Sasan Otraj, Mohammad Ali Bahrevar, Fatollah Mostarzadeh, Mohammad Reza Nilforoshan, “The effect of deflocculants on the self-flow characteristics of ultra low-cement castables in $\text{Al}_2\text{O}_3\text{-SiC-C}$ system”, *Ceramics International* 31 (2005) 647–653
32. Jing Sun, Lian Gao and Jingkun Guo, “ Influence of the Initial pH on the Adsorption Behaviour of Dispersant on Nano Zirconia Powder” *Journal of the European Ceramic Society* 19 (1999) 1725±1730

33. Weihua Lan, Xin Wang, Ping Xiao, "Agglomeration on drying of yttria-stabilised-zirconia slurry on a metal substrate", *Journal of the European Ceramic Society* 26 (2006) 3599–3606
34. R. Greenwood and K. Kendal, "Selection of Suitable Dispersants for Aqueous Suspensions of Zirconia and Titania Powders using Acoustophoresis", *Journal of the European Ceramic Society* 19 (1999) 479±488
35. Floris Esanu, "Self flowing refractory castables: Study of the hydraulic bond and ceramic matrix formation" The University of British Colombia, January 2000
36. Yu E. Pivinskii, "New refractory concretes and binding systems: basic trends of development, production, and use of refractories in the 21st century. Part IV low-cement concretes and cement-free unshaped refractories", *Refractories and Industrial Ceramics*, Vol 39, No:5, pp. 2-10, May 1998
37. Bjorn Myhre and Aase M. Hundere, " The use of particle size distribution in development of refractory castables" Presented at XXV ALAFAR Congress San Carlos de Bariloche, Argentina, Dec. 1-4, 1996
38. S. Goberis and V. Antonovich "Improving the structure and properties of a refractory castable containing porous chamotte fillers", *Refractories and Industrial Ceramics*, Vol. 45, (2004), pp. 360-363
39. M.F.M. Zawrah, N.M. Khalil, "Effect of mullite formation on properties of refractory castables", *Ceramics International*, Vol. 27, (2001), pp. 689–694
40. M.F. Zawrah, "Effect of zircon additions on low and ultra-low cement alumina and bauxite castables", *Ceramics International*, Vol. 33 (2007), pp. 751–759
41. S. Mukhopadhyay, S. Ghosh, M.K. Mahapatra, R. Mazumder, P. Barick, S. Gupta, S. Chakraborty "Easy-to-use mullite and spinel sols as bonding agents in a high-alumina based ultra low cement castable", *Ceramics International*, Vol. 28, (2002), pp. 719–729
42. Fabio A. Cardoso, Murilo D.M. Innocentini, Marcela F.S. Miranda, Fernando A.O. Valenzuela, Victor C. Pandolfelli, "Drying behavior of hydratable alumina-bonded refractory castables", *Journal of the European Ceramic Society*, (2003)

43. Dagmar Gierisch, Andreas Buhr, Jerry Dutton, Margarete Hösler, Brunhilde Franz “Aging behaviour of Alphabond and Calcium Aluminate Cement bonded castables”, Almatiss GmbH, Ludwigshafen, Germany
44. Ivone R. de Oliveira, Andre R. Studart, Fernando A.O. Valenzuela, Victor C. Pandolfelli “Setting behavior of ultra-low cement refractory castables in the presence of citrate and polymethacrylate salts”, *Journal of the European Ceramic Society*, Vol. 23 (2003), pp. 2225–2235
45. Aksel C., Warren P, Riley F. “Fracture behaviour of magnesia and magnesia-spinel composites before and after thermal shock”. *Journal of the European Ceramic Society* 24, pp. 2407-2416 (2004)
46. S. Ribeiro, J.A. Rodrigues, “The influence of microstructure on the maximum load and fracture energy of refractory castables” *Ceramics International* 36 (2010), pp. 263–274
47. Fangbao Ye, M. Rigaud, Xinhong Liu, Xiangchong Zhong “High temperature mechanical properties of bauxite-based SiC-containing castables” *Ceramics International* 30 (2004) pp. 801–805
48. GV White, C.M. Sheppard, M Bowden, M Ryan, GC Barris, M Cooper and C Yu Chen, “Precision Cast Sialon-bonded Silicon Carbide for Molten Metal Refractory Applications” *Journal of the Australian Ceramic Society* Volume 45[1], 2009, pp. 50-57
49. L.A. Diaz, R. Torrecillas, A.H. De Aza, P. Pena, S. De Az, “Alumina-rich refractory concretes with added spinel, periclase and dolomite: A comparative study of their microstructural evolution with temperature”, *Journal of the European Ceramic Society* 25 (2005) pp. 1499–1506
50. G. Prokopski J. Halbiniak and B. Langier The examination of the fracture toughness of concretes with diverse structure *Journal of Materials Science* 33 (1998) pp. 1819-1825
51. George Gogotsi, Sergey Mudrik, Vasily Galenko, “Evaluation of fracture resistance of ceramics: Edge fracture tests” *Ceramics International* 30 (2004) pp.801–805
52. S. Mukhopadhyay, P.K. Das Poddar, “Effect of preformed and in situ spinels on microstructure and properties of a low cement refractory castable” *Ceramics International*, Vol:30 Issue:3, pp. 369-380

53. Fangbao Ye, M. Rigaud, Xinhong Liu, Xiangchong Zhong, “High temperature mechanical properties of bauxite-based SiC-containing castables”, *Ceramics International* 30 (2004) pp. 801–805
54. American Society for Testing and Materials, ASTM C 1421-99, “ Standard Test Methods for Determination of Fracture Toughness of Advanced Ceramics at Ambient Temperature”
55. Palmer G.B., Baker G, “Specimen size effect on fracture toughness for a low cement refractory” *International Journal of Rock Mechanics and Mining Sciences and Geomechanics Abstracts* Vol:22,Issue:1, (1995) pp.51-61
56. L.P. Mullins, M.S. Bruzzia, P.E. McHugh, “Measurement of the microstructural fracture toughness of cortical bone using indentation fracture”, *Journal of Biomechanics* 40 (2007), pp. 3285–3288
57. G.M. Pharr, ”Measurement of mechanical properties by ultra-low load indentation”, *Materials Science and Engineering A* 253 (1998) pp. 151–159
58. B.R. Lawn, A.G. Evans and D.B. Marshall, “Elastic/Plastic indentation damage in ceramics: The median-radial crack system, *Journal of American Ceramic Society*, Vol:63, No:9-10, 1980
59. J. Kruzica, D.K. Kim, K.J. Koester, R.O. Ritchie, “Indentation techniques for evaluating the fracture toughness of biomaterials and hard tissues”, *Journal of The Mechanical Behavior of Biomedical Materials* 2, 2009, pp. 384-395
60. Taihua Zhang, Yihui Feng, Rong Yang and Peng Jiang, “A method to determine fracture toughness using cube-corner Indentation”, *Scripta Materialia* 62 (2010), pp. 199–201
61. Ji-yu Sun, Jin Tong, “Fracture Toughness Properties of Three Different Biomaterials Measured by Nanoindentation”, *Journal of Bionic Engineering* 4 (2007) pp. 11-17
62. J.J. Guo, K. Wang, T. Fujita, J.W. McCauley, J.P. Singh, M.W. Chen, “Nanoindentation characterization of deformation and failure of aluminum oxynitride”, *Acta Materialia* 59 (2011) pp. 1671–1679
63. L.Ruiz, M.J.Readey, “ Effect on heat treatment on grain size, phase assemblage and mechanical properties of 3 mol% Y-TZP”, *Journal of the American Ceramic Society*, Vol. 79, No. 9, (1996), pp. 2331-2340

64. N. Gupta, P. Mallik, B. Basu, "Y-TZP ceramics with optimized toughness: new results", *Journal of Alloys and Compounds*, 379 (2004), pp. 228-232
65. E.C. Subbarao, "Zirconia-overview", Department of Metallurgical Engineering, Indian Institute of Technology, Kanpur, India
66. M. Morinaga, H. Adachi, M. Tsukada, "Electronic Structure and Phase stability of ZrO_2 ", *Journal of Physics and Chemistry of Solids*, Vol. 44, Issue 4(1982), pp. 301-306
67. Masahiro Yoshimura, "Phase stability of Zirconia", *American Ceramic Society Bulletin*, Vol:67, Issue:12, 1998, pp. 1950-1955
68. S. Shukla, S. Seal, "Mechanism of room temperature metastable tetragonal phase stabilisation in zirconia", *International Materials Review*, Vol. 50, No. 1, pp. 1-20
69. P.F. Lange, "Transformation Toughening: Part 2", *Journal of Material Science* Vol. 17, (1982) pp. 225-234
70. Dae Joon-Kim, "Effect of Ta_2O_5 , Nb_2O_5 and Hf_2O_5 alloying on the transformability of Y_2O_3 stabilized tetragonal ZrO_2 ", *Journal of The American Ceramic Society*, 73,(1), 1990, pp. 115-120
71. P.F. Becher, "Toughening behavior in ceramics associated with the transformation of tetragonal ZrO_2 ", *Acta Metall.*, Vol. 34, No. 10, (1986) pp. 1885-1891
72. M. Hillert, "Thermodynamic model of cubic tetragonal transition in nonstoichiometric zirconia", *Journal of American Ceramic Society*, Vol. 74, Issue: 8 (1991), pp. 2005-2006
73. S.P.S. Badwal, N. Nardella, "Formation of monoclinic zirconia at the anodic face of tetragonal", *Applied Physics A Solids and Surfaces*, Vol. 49, Issue: 1 (1989), pp. 13-24
74. R.C. Garvie, "Thermodynamic analysis of the tetragonal to monoclinic transformation in constrained zirconia microcrystal", Vol. 20, Issue:10, (1985), pp. 3478-3486
75. J. Vleugels, Z.X. Yuan, O. Van Der Biest, "Mechanical properties of Y_2O_3/Al_2O_3 -coated Y-TZP ceramics", *Journal of the European Ceramic Society* 22 (2002) pp. 873-881

76. F.F.Lange, “ Transformation Toughening Part 3 Experimental Observations in $\text{ZrO}_2\text{-Y}_2\text{O}_3$ System”, Journal of Materials Science, Vol. 17, Issue 1, (1982), pp. - 240-246
77. H. Schubert, G. Petzow, “Microstructural investigations on the stability of yttria stabilized tetragonal zirconia”, Advanced in Ceramics, Vol, 24, Science and Technology of Zirconia III (1998), pp. 21-28
78. K. Tsukuma, Y. Kubota, T.Tsukidate, “ Thermal and mechanical properties of Y_2O_3 stabilized tetragonal zirconia polycrystals”, Advanced in Ceramics, Vol. 12 : Science and technology of Zirconia II, (1984), pp. 382-390
79. T. Sakuma, H. Eda. H. Suto, “ Composition optimization of $\text{ZrO}_2\text{-Y}_2\text{O}_3$ alloys to improve the fracture toughness”, Advances in Ceramics, Vol. 24, Science and Technology of Zirconia III, (1988), pp. 357-363
80. T. Masaki, K. Sinjo, “ Mechanical properties of highly toughened $\text{ZrO}_2\text{-Y}_2\text{O}_3$ ”, Vol. 13, Issue:2, (1987), pp. 109-112
81. F.F Lange, D.J.Green, “ Effect of inclusion size on the retention of tetragonal ZrO_2 : theory and experiments”, Advanced in Ceramics, Vol. 3 : Science and technology of Zirconia III, (1981), pp. 217-225
82. O.Vasylykiv, Y. Sakka, V.V.Skorokhod, “Low temperature processing and mechanical properties of zirconia and zirconi-alumina nanoceramics”, J. Am. Ceram. Soc., 86 [2],299-304, (2003)
83. F.F. Lange, “Transformation-toughened ZrO_2 : Correlations between grain size control and composition in the system $\text{ZrO}_2\text{-Y}_2\text{O}_3$ ”, J. Am. Ceram. Soc., 69,[3], (1986), pp. 240-242
84. B.F. Sorensen, A.N. Kumar, “Fracture resistance of 8 mol-% yttria stabilized zirconia”, Bull. Mater. Sci., Vol. 24, No. 2, (2001), pp. 111-116
85. M. Matsui, T. Soma, I. Oda, “*Stress-induced transformation and plastic deformation for Y_2O_3 -containing zirconia polycrystals*”.,J. Am. Ceram. Soc. 69(3) (1986), 198–203
86. R.C.Garvie, M.F.Goss, “Intrinsic size dependence of the phase transformation temperature in zirconia microcrystals”, Journal of Materials Science, Vol. 21, Issue:4, (1986), pp. 1253-1257
87. R. H. J. Hannink and M. V. Swain, “Progress in transformation toughening of ceramics ” Mater. Sci. 24 (1994), pp. 359–408

88. L. Gao, T.S. Yen, and J.K. Guo, "Influence of ZrO_2 particle size on toughening in hot-pressed Y-TZP", *Advances in Ceramics*, Vol:24, 1988, pp. 405-414
89. S. Stemmer, J. Vleugels, and O. Van Der Biest, " Grain boundary segregation in high purity yttria stabilized tetragonal zirconia polycrystals (Y-TZP)", *J. Eur. Ceram. Soc.* 18 (1998), pp. 1565-1570
90. J.P. Singh "The effects of unstabilized ZrO_2 on the fracture surface energy and thermal-shock resistance of MgCr_2O_4 ", *Journal of Materials Science*, 1987, pp.2685-2690
91. A. K. Chakravorty, D. K. Ghosh, "Kaolinite-mullite reaction series: The development and significance of a binary aluminosilicate phase", *J. Am. Ceram. Soc.* 74, 6 (1991) pp.1401-1406
92. Gerotto, M. V., Studart, A. R., Innocentini, M. D. M., Pandolfelli, V. C., Cabo, S. S., "Kaolin, metakaolin and microsilica as fillers for high-alumina refractory castables", *American Ceramic Society Bulletin*, 81, 2002, pp. 40-47
93. M. V. Gerotto, A.R. Studart, R.G. Pileggi, V.C. Pandolfelli, "Zero cement, high-alumina castables." *Am. Ceram. Soc. Bull.* 79 (2000) pp. 75–83.

CURRICULUM VITAE

Cem Gogtas

Place of Birth: Istanbul, Turkey

Education:

University of Wisconsin-Milwaukee, Department of Materials Engineering	Milwaukee, WI
Ph.D. in Materials Engineering	August- 2012
Major Advisors: Prof. Hugo Lopez, and Ass. Prof. Konstantin Sobolev	

Istanbul Technical University, Metallurgical and Material Engineering	Istanbul-Turkey
Ms.C. Materials Engineering-Ceramic Program	May-2004
Major Advisor: Prof. Niyazi Eruslu	

Yildiz Technical University, Metallurgical and Material Engineering	Istanbul-Turkey
B.Sc in Metallurgical Engineering	July-2000

Dissertation Title: Development of Nano ZrO₂ Reinforced Self-Flow Low and Ultra Low Cement Refractory Castables

Publications:

1. Gogtas C., Sobolev K., Lopez H. "Effect of cement content on the properties of self-flowing refractories castables with nano-zirconia." will be submitted to American Ceramic Society Bulletin, 2012
2. Gogtas C., Lopez H., Sobolev K. " Effect of nano-ZrO₂ addition on the mechanical behavior of ultra-low cement castables" submitted to Cement and Concrete Research, 2012
3. Gogtas C, N.Unlu, A.Odabasi, L.Sezer, S.Guner, G.Goller, N.Eruslu. "The investigation of the effects of firing temperature on the physical properties of a bauxite-based refractory castable" "Refractories and Industrial Ceramics", 2012, 1, 24-30
4. Gogtas.C, N.Unlu, A.Odabasi, L.Sezer, F.Cinar, S.Guner, G.Goller, N.Eruslu. "Preparation and characterization of self-flowing refractory material containing 97IU type microsilica." Advances in Applied Ceramics, Vol. 109 ,pp. 6-11, 2010.
5. Gogtas, C., N. Unlu, A. Odabasi, L. Sezer, F. Cinar, S. Guner ve N. Eruslu. "Characterization of the physical properties of a self-flowing low-cement castable based on white-fused alumina." Journal of Ceramic Processing Research, 10, 43-48, 2009.
6. Gogtas,C, N.Unlu, A.Odabasi, L.Sezer, F.Cinar, S.Guner, N.Eruslu. "Improvement of properties of self-flowing low-cement castables based on brown fused alumina." Journal of Ceramic Processing Research Volume: 8 Issue: 5 Pages: 324-330, 2007
7. A.Odabasi, N. Unlu, C.Gogtas, L. Sezer, N. Eruslu. "The Effect of Georgia Bentonite on The Properties of Molding Sands." 13th International Metallurgy & Materials Congress
8. A.Odabasi, C.Gogtas, L.Sezer, N.Unlu, N.Eruslu. "Heat Treatment of High Chromium Contented White Cast Irons." Metal World Technical Magazine

Conferences

1. Gogtas C., Sobolev K., Lopez H. "Effect of cement content on the properties of self-flowing refractory castables with nano-zirconia." American Ceramic Society, 48th Annual Symposium on Refractories, March 28-29 2012, St. Louis
2. Gogtas C., Lopez H., Sobolev K. " Effect of nano-ZrO₂ addition on the mechanical behavior of ultra-low cement castables" NICOM 4, 4th International Symposium on Nanotechnology in Construction, May 20-22 2012, Crete-Greece

Significant Technical Projects:

- Production and characterization of nano-ZrO₂ reinforced ultra low and low cement self flow refractory castables (Ph.D. thesis), supported by Engineering-Science of Department-UWM 2008-2012
- Role of CeO₂ nanoparticles coatings on the corrosion resistance of austenitic stainless steels at high temperatures, Advanced Analysis Facility (AAF) under summer internship program in University of Wisconsin, Milwaukee (UWM) summer-2008
- Characterization of self flowing low cement refractory castables, supported by Institute of Science and Technology, Istanbul Technical University, 2002-2004

Research Experience:

- Characterization of nano ZrO₂ reinforced ultra low and low cement self flow refractory castables, (Ph.D. thesis)
- Role of CeO₂ nanoparticles coatings on the corrosion resistance of austenitic stainless steels at high temperatures, Advanced Analysis Facility (AAF) under summer internship program in University of Wisconsin, Milwaukee (UWM) summer-2008
- Production and characterization of self-flowing low cement refractory castables (Master Thesis) with Refsan Refractory & Building Cons. Ltd. Co., 2002 –2003.
- Research on glass properties and mold materials for glass production (Undergraduate thesis) in Sisecam Glass Plant., Fall 1999-Spring 2000.

Honor/Awards:

- Teaching Assistantship, UWM (2006-2012)
- Chancellor's Graduate Student Award, UWM (2006-2012)
- AAF Summer Research Intern Program, UWM, Summer-2008

Work Experience:

- Teaching Assistant, Department of Materials Engineering, UWM Fall 2006 - 2012
- Taught 2 weekly sections of Engineering Materials Lab and Materials and Processes in Manufacturing Lab
 - Graded undergraduate level courses (Engineering Materials and Materials and Processes in Manufacturing)
- Manager Laboratory, Department of Materials Engineering, UWM Fall 2008 - 2012
- Set up the labs for Engineering Materials and Materials and Processes in Manufacturing classes, including: lab procurements, and followed up sample preparation with the machine shop.
 - Trained and assisted students to use Scanning Electron Microscope (SEM) and Energy Dispersive Spectroscopy (EDS).
 - Advised and assisted the students to use different lab equipments in their class project
- Engineering Internship, Advanced Analytical Facility (AAF), UWM Summer-2008
- Produced nano-ceria by using sol-gel method.
 - Coated stainless steel with nano ceria and examined the crystallization and phase formation behavior upon annealing at high temperature
- Research Engineer, Team Leader, Refsan Refractory & Building Cons Ltd.,-Turkey 2004-2006
- Led the team of four engineers and oversaw their work
 - Produced of self-flowing low cement refractory castables